DOCTOR OF PHILOSOPHY

The Detection of Gastrointestinal Inflammation with Microultrasound and The Feasibility of Ultrasound Capsule Endoscopy

Cox, Benjamin F.

Award date:
2020

University of Dundee

The Detection of Gastrointestinal Inflammation with Microultrasound and The Feasibility of Ultrasound Capsule Endoscopy

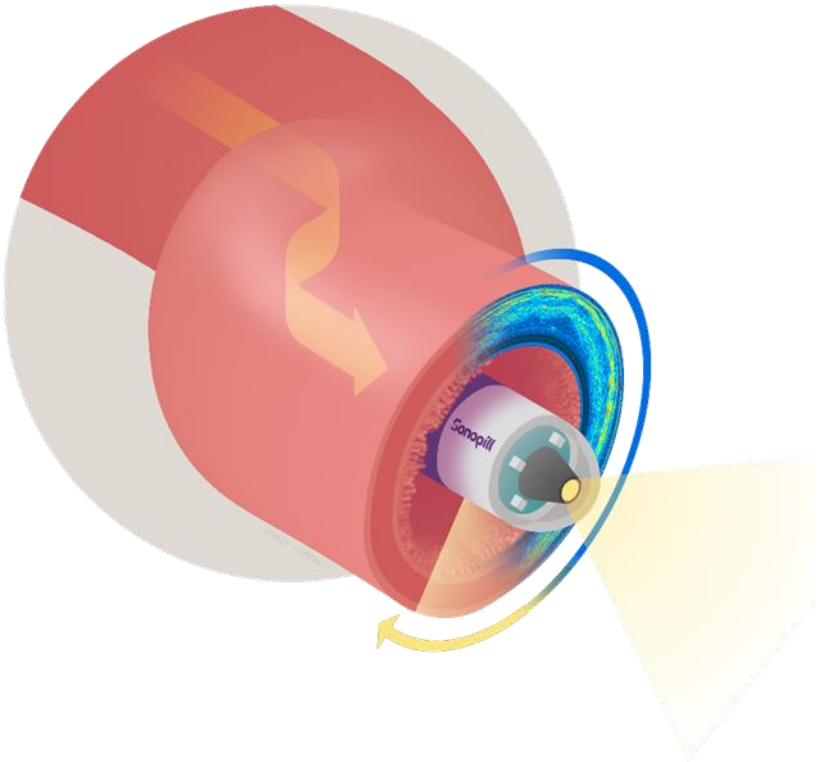

BENJAMIN F COX

A THESIS SUBMITTED IN FULFILMENT OF THE REQUIREMENTS FOR THE DEGREE OF DOCTOR OF PHILOSOPHY (PH.D.) TO THE SCHOOL OF MEDICINE, UNIVERSITY OF DUNDEE, DUNDEE, SCOTLAND, UK.

20 NOVEMBER 2020

Table of Contents

Declaration

I hereby declare that this thesis titled "Feasibility Ultrasound Capsule Endoscopy and Detection of Gastrointestinal Inflammation with Microultrasound" has been prepared by me under the direct guidance of Professor Inke Näthke, Professor Bob Steele and Professor Sandy Cochran as a part of my study for the award of PhD degree at the University of Dundee, Dundee, Scotland. I have not submitted this thesis previously for the award of any degree or diploma at any other institution.

Signature: [redacted] **Date:**…14April2020...

Certificate

This is to certify that Dr Benjamin F. Cox has done his research under my supervision and complied with all the requirement for the submission of this Doctor of Philosophy thesis to the University of Dundee, Dundee, Scotland.

Signature: [redacted] **Date:** April 14th 2020

Abstract

Crohn's Disease (CD) is a lifelong inflammatory disorder of the gastrointestinal tract. It may manifest anywhere along the gut including anatomically remote sections of the small bowel. The principal motivation behind the work described here is to meet the clinical need for improved means of diagnosis and management of inflammatory disorders of the bowel, such as CD. Potentially, improvements can be met by augmenting capsule endoscopes with microultrasound. Microultrasound (μUS) frequencies are > 20 MHz and have the potential to provide highly detailed transmural images of the bowel wall. This would provide capsule endoscopes with a means of detecting and displaying subsurface disease and, provide clinicians with the means of treating the disease to achieve complete or histological remission.

Investigating the feasibility of ultrasound capsule endoscopy (USCE) utilised explanted human tissue, *in vivo* pig trials and mouse experiments. Human tissue experiments were aimed at identifying a suitable μUS frequency for USCE and examining the relationship between acoustic and histologic bowel layers. Pig experiments aimed to demonstrate the technological feasibility of USCE. The primary endpoint was to determine if sufficient coupling occurred between capsule ultrasound transducer(s) and the mucosa to generate a transmural μUS bowel image. Mouse experiments were aimed at determining whether μUS could directly detect inflammation via the infiltration and accumulation of white blood cells. This also included what was the lowest grade of inflammation detectable.

Chapter 4 describes the results of scanning explanted human colon with different microultrasound frequencies. The purpose of this pilot study was twofold. One aim was to tentatively identify a suitable frequency for inclusion into USCE. The other aim was to examine the relationship between acoustic tissue layers and histological layers. Surgically acquired tissue was scanned at various μUS frequencies in three different orientations with respect to the μUS transducer. This was done to determine the effect layer interface and layer components on acoustic layer generation. A total of five cases were included in this study and tissue was collected exclusively from the colon. Neoplastic disease was the reason for all five procedures. Tissue was collected approximately 20 cm from the tumour and presumed healthy. Three cases (1-3) were transmurally scanned with the transducer facing the mucosa (i.e. mucosa to serosa image). Microultrasound was able to depict multiple acoustic layers. Case 1, in particular, was able to depict up to 7 acoustic layers with full tissue penetration at 34 MHz. Case 4 was scanned in a novel orientation where the histologic layers were scanned individually.

This permitted each layer to generate a signal based on its composition without contribution from layer interfaces. Five acoustic layers were generated at 25 MHz and seven acoustic layers were detected at 37 MHz. Case 5 was scanned transmurally from serosa to mucosa at 37 MHz. Five distinct layers were detected. Results indicated that a frequency ≈35 MHz was suitable for inclusion. This was due to the high degree of superficial tissue detail and both frequencies demonstrated sufficient transmural penetration. The second aim, to further explore the relationship between acoustic and histological layers, demonstrated that scanning in various orientations represents a practical means of examining the ultrasound-histology relationship.

Chapter 5 describes the results obtained with a prototype tethered USCE device in vivo addressing the feasibility of USCE in the gastrointestinal tract. The primary clinical endpoint of this series of experiments was to determine whether sufficient coupling occurred between the capsule transducer(s) and the gut mucosa of pigs to generate an ultrasound image. A total of 18 in vivo experiments were carried out with SonoCap, a tethered USCE prototype. Experiments were conducted in the oesophagus (N=6) and small bowel (N=12) in nonrecovery anaesthetised pigs. Scans were done in both static and dynamic capsule modes. Images were generated of the oesophagus in static and dynamic modes indicating sufficient transducer to tissue coupling occurred. Images were also generated of the small bowel in static and dynamic modes indicating capsule transducer to mucosa contact. Similar results were also achieved using an alternatively designed USCE prototype from colleagues at Shenzhen University. Results showed coupling between the capsule's acoustic window and transmural images of the oesophagus and small bowel. Evidence of USCE feasibility was observed in both prototype capsules indicating that further research and capsule development is warranted.

Chapter 6 describes the results of mouse gastrointestinal (GI) inflammation experiments. The purpose of these experiments was twofold. The first objective was to determine whether high resolution microultrasound could directly detect leukocyte infiltration during GI inflammation. The second objective was to determine the lowest grade of inflammation detectable. Stage 1 was able to demonstrate the ability of μUS to detect overt or severe (i.e. visually perceptible) inflammation at 37 MHz. Subsequent attempts at 37 MHz (Stages 2 and 3) to detect low grades (i.e. mild and moderate inflammation) were unsuccessful. This was despite histopathologic signs of inflammation upon microscopic examination. Further experimentation at 62 MHz was also unable to detect lowest grade of inflammation. Although sever inflammation was detected, low grade

inflammation may have been beyond the capabilities of the two frequencies used in this series of experiments. Improved methods of co-registration of the two modalities, μUS scanning and histology, would assist with additional experiments of this nature.

The research described here examined a number of facets in the development of USCE in order to fulfil a clinical need for an improved means of diagnosis and management of CD and has succeeded in demonstrating areas of potential utility for further study.

Acknowledgements

I would like to thank my supervisors, Profs Inke Näthke, Bob Steele and Sandy Cochran, for providing me the opportunity. The experience has proven to be very enriching and immersed me in subjects that I never dreamed I would be involved with. I am also extremely grateful to Ian Newton for all his assistance, persistence and Taco Tuesdays.

I would like to thank all members of the Sonopill for their support. I very much enjoyed our time together on this worthwhile project. I would also like to thank Dr Elaine Henry for her advice and guidance in navigating both the GI tract and NHS. I am grateful for the assistance provided by the staff of both the WBRU and WTCLLA. I am also grateful for the help provided by Tayside Tissue Bank. Thanks to everyone on MSI-4, best of luck with your Western Blots.

Finally, I would like to thank my family for their support and encouragement to see this endeavour through to the end. I am particularly grateful for Jarka's infinite patience and understanding, Alex's constant coaching and Andrew for being Andrew. This would have not been possible without the support from all of you.

List of Figures

List of Tables

List of Abbreviations

Adenomatous Polyposis Coli	$Apc^{Min/+}$
Alternative Macrophage Response	M2
American College of Gastroenterology	ACG
American Society for Gastrointestinal Endoscopy	ASGE
Antigen Presenting cells	APC
Blood Per Rectum	BPR
Bone Marrow	BM
Caecum	Cae
Capsule Endoscopy	CE
Classical Macrophage Response	M1
Colon	Co
Complete Blood Count	CBC
Computed Tomography	CT
Critical Neutrophil Concentration	CNC
Crohn's Disease	CD
Crohn's Disease Activity Index	CDAI
Crohn's Disease Endoscopic Index of Severity	CDEIS
Damage-Associated Molecular Pattern	DAMP
Deep Bowel Enteroscopy	DSBE
Degassed Phosphate Buffered Saline	dPBS
Deoxyribonucleic Acid	DNA
Dextran Sodium Sulphate	DSS
Distal	D
Endothelial Cell	EC

Endotracheal Tube	ET
European Crohn's and Colitis Organisation	ECCO
European Society of Pathology	ESP
Extracellular Matrix	ECM
Fas ligand	FasL
Fas Receptor	FasR
Gastroesophageal Junction	GOJ
Gastrointestinal	GI
Goblet Cell	GC
Gut Associated Lymphoid Tissue	GALT
Haematoxylin and Eosin	H&E
High Power Field	HPF
Human Leukocyte Antigen	HLA
Hydrogen Peroxide	H_2O_2
Hydroxyl Radicals	HO·
Immunoglobulin	Ig
Inflammatory Bowel Disease	IBD
Interleukin	IL
Intravascular Utrasound	IVUS
Intravenous	IV
Lamina Propria	LP
Lead Zirconate Titanate	PZT
Lipopolysaccharide	LPS
Lithium Niobate	LNO
Magnetic Resonance Imaging	MRI

Major Histocompatibility Complex	MHC
Matrix Metalloproteases	MMP
Mesenteric Lymph Node	MLN
Microfold cells	M-cells
Microultrasound	μUS
Mucosa	M
Muscularis Mucosae	Mm
Muscularis Propria	MP
Myeloperoxidase	MPO
Named Veterinary Surgeon	NVS
Neutrophil Extracellular Trap	NET
Nicotinamide Adenine Dinucleotide Phosphate	NADPH
Pathogen-Associated Molecular Pattern	PAMP
Pattern Recognition Receptors	PRR
Peyer's Patches	PP
Phosphate Buffered Saline	PBS
Polymorphonuclear	PMN
Polyvinylidene Fluoride	PVDF
Procedure Project Licence	PPL
Project Establishment License	PEL
Proximal	P
Radiofrequency	RF
Randomised Control Trial	RCT
Reactive Oxygen Species	ROS
Serosa	S

Signal to Noise Ratio	SNR
Small Bowel	SB
Submucosa	SM
Superoxide Anion	$O2^{-}$
Toll-Like Receptor	TLR
Transcutaneous Abdominal Sonography	TABS
Transforming Growth Factor	TGF
Tumour Necrosis Factor	TNF
Ulcerative Colitis	UC
Ultrasound	US
Ultrasound Capsule Endoscopy	USCE
Vascular Endothelial Growth Factor	VEGF
Villi	V
Wellcome Building Resource Unit	WBRU
White Light Imaging	WLI
Wild Type	WT

Chapter 1: Introduction

1. Chapter Introduction

This chapter provides the motivation, namely clinical need that drove forward the work described in this thesis. It also includes an introduction to capsule endoscopy (CE) and an overview of ultrasound (US). An outline of the thesis is provided as well as my own contribution to knowledge and a list of publications arising from the work.

1.1. Motivation

The principal motivation behind this work is to meet the clinical need for improved means of diagnosis and management of inflammatory disorders of the bowel, particularly Crohn's Disease (CD), by improving the diagnostic (i.e. imaging) capabilities of CE.

1.1.1. Inflammatory Disorders of the Gastrointestinal Tract

Enteritis is a nonspecific descriptive term denoting an inflamed state of the small bowel. The causes of enteritis are numerous. Aetiology ranges from infectious causes (e.g. bacterial or viral) to autoimmune causes (e.g. Coeliac Disease) and to incompletely understood causes (e.g. Inflammatory Bowel Disease). Although varying from case to case, common signs and symptoms can include abdominal cramping and pain, diarrhoea, nausea, vomiting and malnutrition.

CD, or regional enteritis, is a member of the Inflammatory Bowel Disease (IBD) group which includes Ulcerative Colitis (UC). It is a chronic and progressive lifelong disorder marked by intermittent periods of quiescence (i.e. remission) and relapse (i.e. flare). The disease may affect any part of the gastrointestinal (GI) tract from mouth to anus, but most commonly manifests in the terminal ileum of the small bowel [1]. Figure 1.1 depicts the more common anatomic areas affected in the human GI tract.

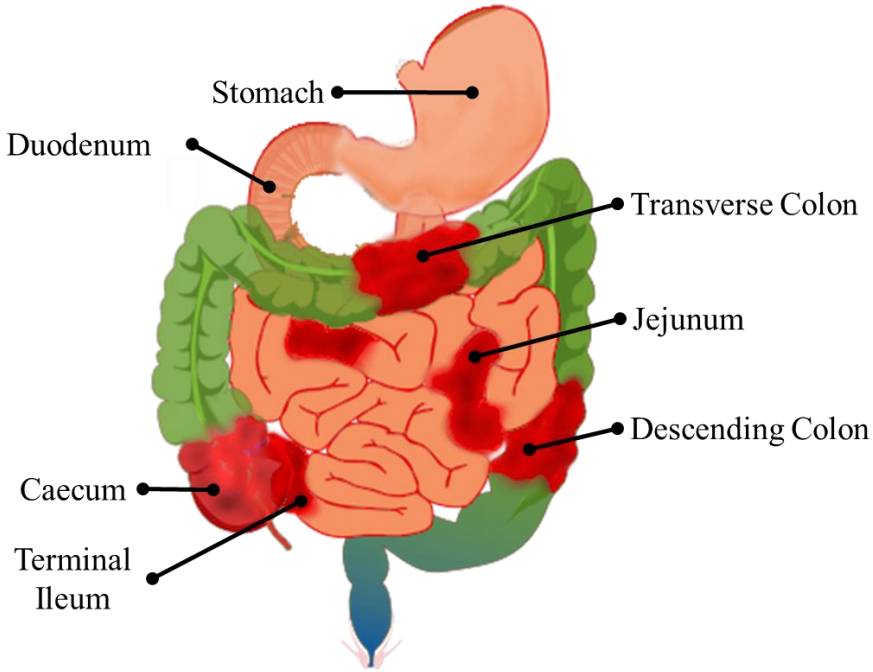

Figure 1.1. Illustration of the small bowel and colon showing prevalent locations of Crohn's Disease CD) manifestation. While CD may affect any part of the GI tract, it predominately manifests at the terminal ileum. Image adapted from Mariana Ruiz, public domain.

CD pathogenesis is incompletely understood but is considered to be multifactorial and involve environment (e.g. diet and lifestyle), resident bowel microbes (i.e. Gut Flora) and genetics [2]. With regards to the genetic aspect of CD, there is an increased risk of development with a positive family history [3]. Several genes and their associated products have been identified that contribute to disease development. Genetic factors such as *NOD2* and *ATG16L1* are involved in innate cell priming and phagocytosis. Their involvement indicates the importance of immunity in the development of CD [2].

There is no known cure for CD. Treatment involves pharmaceutical management of inflammation and surgical intervention for related complications. Pharmaceutical management involves multiple medications which include anti-inflammatory drugs (e.g. steroids and 5-aminosalicylic acid derivatives), immunosuppressants (e.g. methotrexate) and biologics (e.g. monoclonal antibodies and Tumour Necrosis Factor inhibitors). The primary therapeutic endpoint is to induce and maintain a lasting remission, to return the patient to baseline function and promote adequate nutrition and paediatric growth. However, medications used are not without side effects, some of which can be serious, particularly in terms of immune suppression and risk of opportunistic infection. This requires balancing therapeutic effect against unwanted side effects to achieve treatment goals.

Historically indications of treatment success have relied on physician/patient assessment regarding the resolution of symptoms. The CD Activity Index (CDAI) was developed and validated in the 1970s to assess treatment efficacy with placebo controlled drug trials [4]. The index scores a number of factors (e.g. stools per day, maximum abdominal pain and patient wellbeing). The scores are tallied out of 600 points. Scores greater than 150 are considered indicative of active disease with the severity of the grade (i.e. mild, moderate and severe) elevating as one approaches 600. The prominent criticism of CDAI is the subjective nature of the assessment. For instance, abdominal pain caused by CD may be over or under reported by patients and affecting overall score. Furthermore, symptoms often do not correlate well with disease activity, with the potential to result in over or under treatment. It is for this reason that the American College of Gastroenterology (ACG) no longer recommends symptom resolution as the sole guide for treatment [5]. This has led to the development of more objective means of assessment.

A more objective means involves endoscopic mucosal assessment for signs of 'mucosal healing'. Mucosal healing is simply defined as the absence of mucosal ulcerations and/or erosions [6]. The CD Endoscopic Index of Severity (CDEIS) assesses disease activity based on the presence of ulcers (deep and superficial) and area of disease involvement which involves ulcerated and non-ulcerated tissue and luminal narrowing [7]. Scores are collated for each region examined (e.g. ileum and ascending colon) for final score. As with CDAI, higher scores equate to greater severity. Although considered more objective than self-assessment, image interpretation is subject to observer bias and is reliant on assessment of superficial manifestations of disease [8]. Subsurface disease activity cannot be assessed without the benefit of tissue biopsy. Nevertheless achieving combined clinical (CDAI <150) and endoscopic remission (CDEIS <3) or 'deep remission' is associated with improved patient prognosis [9].

1.1.2. An Emerging Therapeutic Endpoint

A relatively new treatment endpoint has recently emerged in the medical management of CD. The new endpoint proposes a target of 'complete remission' or histological remission based on complete resolution of inflammation at the microscopic level [10]. Currently, the definition of histologic resolution is evolving and has yet to be clinically validated. Nevertheless, one generally accepted criteria is the absence of acute inflammatory cells in the superficial layers of the bowel [10]–[12]. A systematic review

by Bryant *et al* concluded that complete remission represented an advanced treatment endpoint independent of deep remission [11]. Furthermore, data indicates that achieving a complete remission confers improved patient prospects in terms of decreased relapse rates, hospitalisations, surgical intervention and neoplastic transformation.

It has been demonstrated that tissue deemed endoscopically healed can harbour active microscopic (i.e. residual) disease [13]. The presence of residual disease can be considered a harbinger for early relapse. According to the European Crohn's and Colitis Organisation (ECCO) and the European Society of Pathology (ESP), the presence of persistent inflammatory activity in UC is a strong predictor of clinical relapse [14]. Unfortunately similar data is scarce when examining the same issue in CD. This is partially due to the patchy pan-enteric distribution and the limited reach of ileocolonoscopy. Adding to the data shortage is the invasive nature of endoscopy; it is not regularly performed on asymptomatic patients. As a consequence histologic assessment of response is not routine [10], [11]. Nonetheless, two studies did determine that between 25% - 37% of cases harboured residual disease activity by histology, despite clinical and endoscopic deep remission [15], [16]. Whether this has the same implications as UC remains to be fully elucidated.

Whilst adopting a new treatment target of complete remission has the potential to improve patient outcomes, it has yet to be fully embraced. Hurdles to implementing this strategy are numerous, including procedural risk, time and overall cost involved in obtaining and processing multiple biopsy samples [17]. In addition to these impediments are the technical challenges associated with imaging subsurface pathology, accessing the entire GI tract and minimising risk of the imaging modality [11].

1.2. Capsule Endoscopy

Capsule endoscopy provides a pill based means of examining the entire length of the GI tract in an autonomous and non-invasive manner. While many capsule suppliers exist, the market is dominated by Medtronic (formerly Given Imaging). The following CE description is based on the features of the Pillcam™ system. This consists of capsule, abdominal sensor patches and data logger. The capsule is 11 mm diameter x 26 mm length for PillCam SB (small bowel). Its key feature is the illuminated white light camera capable of imaging the luminal surface (i.e. mucosa) of the GI tract (Figure 1.2).

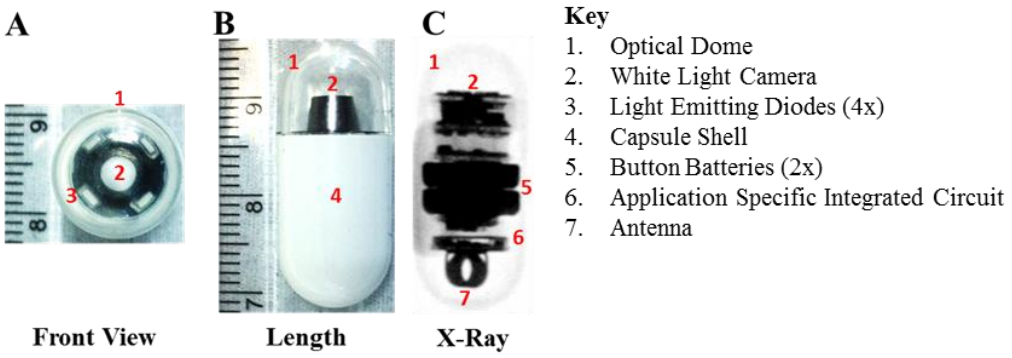

Figure 1.2A-C. (A) Front view of a capsule showing the camera and light emitting diodes (LEDs) for illumination. The diameter of the capsule is 11 mm. (B) Long axis view (length: 26 mm) of a Pillcam™ SB (Medtronic, IE) single camera capsule endoscope (CE). (C) X-ray image of a CE depicting the internal components of the capsule.

1.2.1. History

The introduction of CE into clinical practice followed the work of Gavriel Iddan and Paul Swain reported in 2000 [18]. Capsule endoscopy was particularly attractive for several reasons. First, it provided a means of imaging the entire GI tract including the anatomically remote areas of the small bowel. Other benefits included non-invasive oral mode of delivery, no required sedation, relatively benign safety profile and improved patient acceptance over conventional endoscopy [19].

1.2.2. Indications

Since its introduction, the primary use for CE has become the detection of obscure GI bleeding, particularly in the small bowel. However the role of CE in GI diagnosis and disorder management has expanded to include neoplastic disease, monitoring polyposis syndromes and inflammatory disorders such as Coeliac Disease and CD [20]. Other uses include determining the causes of abdominal pain and malabsorption [21].

1.2.3. Limitations

Despite its benefits, currently available CE suffers from a number of limitations including the inability to biopsy, poor capsule/lesion localization and dependency on gut peristalsis for locomotion [22]. In addition is the restriction to analysis of only the superficial mucosa

due to CE's reliance on visible light for imaging [23]. Visible light rays are in the range 400 - 700 nm and are unable to penetrate beyond the surface of the mucosal layer [24]. Subsurface pathology cannot be detected, and clinicians are dependent on superficial manifestations for assessment. This opens image interpretation to a number of issues. Firstly superficial lesions are often visually obscure and can be variable in appearance [2], [25]. Furthermore, there can be visual overlaps between diseases. Sensitivity also declines when assessing low grade disease, as visibility is less overt [26], [27]. All this can negatively impact the ability of CE to detect signs of disease.

1.3. Ultrasound Capsule Endoscopy

Given the superficial only imaging and lack of biopsy capabilities, improvements in CE are clinically warranted. This statement is the position of the American Society for Gastrointestinal Endoscopy (ASGE). The ASGE's 2013 Technology Status Evaluation Report on CE simply states that 'improvements in technology and techniques are needed' [28]. This is certainly the case for improved assessment of CD especially when considering the benefits of complete remission as indicated by Bryant *et al* [11].

The development of advanced capsule endoscopes is an area of active research, as indicated by the review by Cummins *et al* on alternative modes of CE based diagnosis [29]. One area of CE research and development is the inclusion of microultrasound (μUS) forming the basis of Ultrasound Capsule Endoscopy (USCE).

USCE has the potential to resolve the issue of surface only imaging and mitigate the need for tissue biopsy. Combining the positive aspects of CE (e.g. non-invasive delivery and full bowel transit) with μUS imaging has the potential to assess for subsurface (i.e. optically occult) pathology. This capability can conceivably be applied to monitoring treatment of CD and thereby advancing the concept of achieving complete remission.

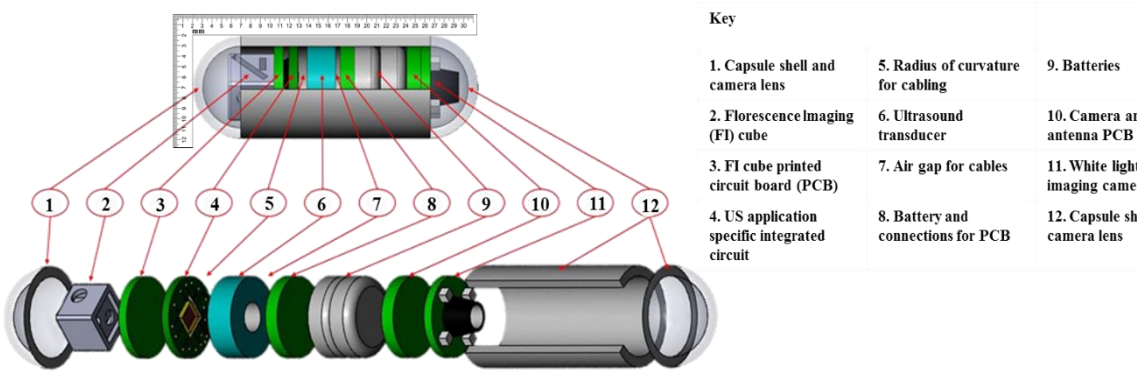

Figure 1.3. Schematic of the ultrasound capsule endoscope (USCE) under development in the Sonopill programme. The 10 mm diameter by 30 mm long capsule, with spherical ends, is intended to contain both ultrasound (component 6) and optical modalities (components 2 and 11). The ultrasound transducer (> 25 MHz) permits high resolution subsurface imaging of the bowel wall. Optical modalities include both white light imaging (component 11) and fluorescent imaging (component 2). Additional constituents include electronic circuitry (components 3, 4 and 10) and batteries (component 9). Image courtesy of Dr. Vipin Seetohul.

The development and proof of concept of USCE was the remit of the Sonopill Programme (EPSRC GR/K034537/2, UK), a multi-institutional, multidisciplinary effort with the aim to incorporate µUS and video modalities into a 10 mm diameter by 30 mm long capsule (Figure 1.3).

1.4. Diagnostic Ultrasound

The history of diagnostic US in medicine as a means of non-invasive internal examination can be traced back to 1942. Karl Dussik of Vienna, Austria, first employed US to detect cerebral tumours and ventricles of the brain [30]. Dussik's ground breaking work was followed by a number of early pioneers in US diagnostics such as George Ludwig in imaging *in vivo* foreign bodies and gallstones [31]. However it was Ian Donald's research in obstetrics in Glasgow, Scotland, that made US familiar to many expectant mothers. His 1958 publication in the Lancet is considered a seminal paper in diagnostic US and prenatal care [32].

Today, US is a ubiquitous presence throughout many disciplines of healthcare such as cardiology, urology and gastroenterology. It is continually praised for its relative low cost, safety profile (e.g. use of nonionizing energy), flexibility (i.e. adaptability), and resolution (e.g. spatial and temporal). It is for these reasons that US was considered for

inclusion into endoscopic devices for the purposes of endoluminal sonography such as endoscopic US (EUS). The drive behind this development was to improve resolution and diagnostic accuracy by removing obstructions (e.g. bone or gas) between the probe and target tissue [33]. It is for the same reasons that US was considered for inclusion into CE. The rationale was to provide high resolution subsurface imaging whilst being able to transit the entire GI tract in a minimally invasive manner [34].

1.4.1. Concepts in Ultrasound

Ultrasound waves are produced by the application of an electrical voltage to a piezoelectric material such as some specialised ceramics [35]. The electrical signal causes a material deformation which generates a high frequency pressure wave. Sound waves are transmitted by an ultrasound transducer (i.e. sound source), which incorporates the material, through tissue and echoic reflections return to the transducer. The echoes are detected by the transducer and are converted to electrical signals to present tissue images based on a time - distance relationship.

Medical US frequency, measured in MHz, is the number of soundwave cycles per second. A cycle is defined as the distance between two soundwave peaks (i.e. wavelength). By shortening the distance between two peaks the frequency of the sound wave is increased. There is a direct relationship between wavelength, image resolution and depth of tissue penetration. This concept will be further explored in section 1.4.2 detailing microultrasound. Generating images with US is the result of the interaction of energy and the medium in which it travels. Energy is provided by sound which is almost always a longitudinal mechanical (i.e. pressure) wave in medical ultrasonics, in which the medium is biological tissue.

Tissue is a heterogeneous combination of material such as cells, muscle and connective components. These components are organised in such a way as to carry out a specific function and are grouped together to form organs such as the GI tract. Grouping of specialised tissue into organs often creates distinctive layers as encountered with skin, blood vessels and the bowel wall. In terms of US, these layers form boundary interfaces between different acoustic properties which have the potential to generate an echo (i.e. reflection) [36]. As sound travels through tissue, it will encounter a tissue boundary and an interface of sufficient difference has the potential to generate a detectable echo.

Differences in tissue properties including density and stiffness (i.e. resistance to compression) affect the speed of sound propagation through tissue.

The speed of sound through tissue is, on average, 1.54 mm/μs but can deviate depending on the properties of the tissue examined. For instance, the speed of sound through muscle is 1.60 mm/μs and 1.45 mm/μs for fat [37]. The difference in speed can be explained by differences in tissue density. The density of muscle is calculated to be 1.06 g/ml and 0.9 g/ml for fat [38][39]. This indicates that the sound speed travelling through tissue is affected by the physical properties of the tissue, with acoustic impedance a key property, comprising the product of density and speed of sound in tissue [35]. Echo generation is a result of impedance differences, or acoustic mismatch, from one layer to another. Sound transiting from one layer to another with a high impedance difference will generate a bright (i.e. hyperechoic) signal. Conversely a weak difference will produce a hypoechoic (muted) signal and no difference results in a black (anechoic) signal [40].

The generation of an echo at the interface is the result of two types of reflection. The first is specular, or mirror like, relative to the wavelength of the ultrasound, and the echo returns directly to the sound source. This is encountered when the material is smooth such as a bone shaft and the source is directly (i.e. 90°) above the reflector. The second is type is diffuse reflection and is the result of sound striking uneven boundaries. The returning echo is distributed across a wide range of angles, as opposed to the single angle in specular reflection. This results in multiple echoes of decreased amplitude (i.e. strength) returning to the sound source. Architecturally, the luminal surface of the GI tract is characterised as a diffuse reflector due to numerous invaginations and projections.

Generated echoes will also experience further scattering as a result of tissue composition. Soft tissue (e.g. bowel wall) is composed of multiple scattering elements such as collagen and muscle fibres [41]. Echoes generated by these elements will occur at multiple angles and randomly interact with one another in a constructive or destructive manner. Echo scattering (i.e. backscatter) is influenced by a number of causes intrinsic to the tissue and US frequency [41], [42]. Tissue dependent factors include the concentration and dimensions of the scatterers (i.e. elements). Echo scattering also relates to the size of the element(s) as scattering occurs where element dimensions are smaller than the frequency's wavelength. Elements must also demonstrate a degree of acoustic impedance difference compared to the surrounding medium to generate an echo. Scattered echoes reaching the transducer contribute to the formation of an US image and result in the characteristic texturing of the images referred to as 'speckle' [43]. Speckle can provide

information regarding the internal make-up of tissue as it is dependent on tissue composition [44], [45].

Only a portion of the original signal is reflected back to the sound source. As sound penetrates successive layers it will undergo attenuation or loss of intensity. In addition to reflection and scattering, two other sources of attenuation will be experienced as sound transits through tissue. The first is refraction and it occurs when sound travels between tissue types with different speeds of propagation. The result is deviation of the signal path from a straight line. If detected, the returning echo may be blurred or cause refraction artefacts by positioning a structure incorrectly. The second cause for signal loss is absorption, which plays a large role in attenuation [43].

Absorption refers to the conversion of sound energy in the medium itself, predominantly into heat. Absorption is affected by three primary variables. The first two, viscosity and relaxation, are inherent tissue characteristics and the third relates to sound frequency [44]. Tissue viscosity, as it relates to friction between tissue components, has a direct relation to sound absorption. Increasing tissue viscosity increases the frictional interaction between components resulting in in greater absorption and conversion into heat. Relaxation refers to the time it takes for a vibrating element to return to a neutral (i.e. relaxed) position [46]. A vibrating element has the potential to attenuate sequential sound waves if the direction of sound and vibration oppose one another. Tissue elements with long relaxation times will have greater potential to attenuate sound energy.

Absorption is related to increasing US frequency, with higher frequencies experiencing greater absorption. Frequency refers to the number of cycles (e.g. sound waves) that occur per unit time. Thus, increasing frequency increases the number of waves per second. A higher frequency also leads to increased absorption due to an increased rate of frictional contact between tissue components. Additionally, there is a decreased likelihood of an element reaching a neutral position before the next soundwave arrives. The result is that higher frequencies experience higher attenuation than lower frequencies with a consequent decrease in depth of tissue penetration.

1.4.2. Microultrasound

Microultrasound (μUS) refers to imaging with higher than normal frequencies. Conventional diagnostic frequencies generally are in the range of 2 - 20 MHz, with frequency choice dependent on the demands of the examination [47].

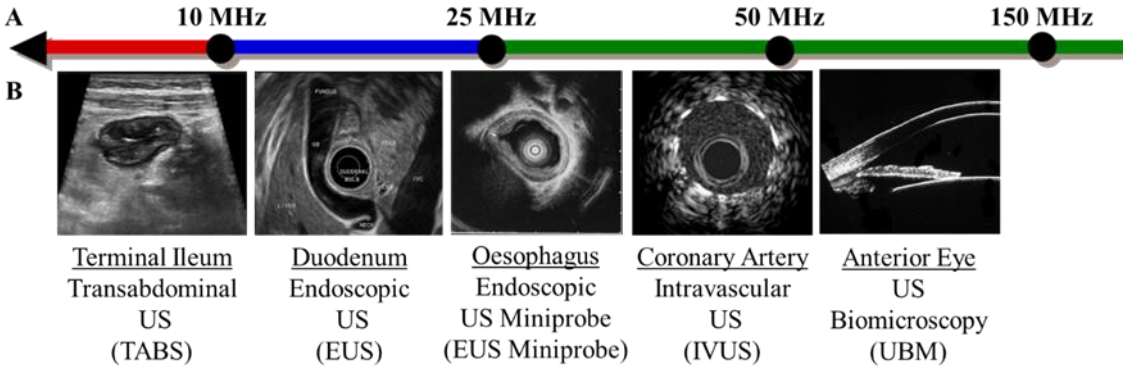

Figure 1.4A-B. (A) Frequency spectrum of ultrasound used in medial US diagnostic. (B) Common applications of medical US and their relation to the frequency spectrum. Image adapted from H. Rafferty, licensed under the Creative Commons Attribution-Share Alike 2.5 and Maffe *et al* [48],May *et al* [49], Krill *et al* [50], Foster *et al* [51], Silverman [52].

Microultrasound utilises frequencies > 20 MHz. Examples of microultrasound used in clinical practice include intravascular US (IVUS) and Ophthalmology (Figure 1.4). As indicated in Figure 1.4, higher frequency US provides improved resolution in both the axial and lateral directions. As frequency is increased, the US wavelength shortens, allowing waves to resolve microstructures too small to generate distinct signals at conventional frequencies. At μUS frequencies, it is postulated that the primary scatterers are nuclei of cells [53], [54]. As discussed previously, echo scattering is influenced by the quantity (i.e. concentration), dimensions and impedance of the scatterers present and the US frequency. By shortening the wavelength, smaller tissue elements (e.g. cell nuclei) present more acoustically and echo generation/scattering will increase with frequency [42], [44]. Furthermore, it stands to reason that an increase in white blood cell concentration during inflammation can potentially affect the acoustic properties of tissue and be detected by μUS.

1.4.3. Ultrasound and the Gastrointestinal Tract

US interaction with the layers of the bowel wall produces an image similar to that shown in Figure 1.5 [55]. At frequencies of 5 - 12 MHz, the bowel wall demonstrates five distinct hyperechoic and hypoechoic layers. These layers are thought to closely correspond to the cardinal histologic layers [55]. The first hyperechoic layer represents the mucosa (M) where the epithelium interfaces with the US coupling medium or transducer. The second anechoic signal corresponds with the deeper portion of the M and

includes the lamina propria (LP) and muscularis mucosae (Mm). At the interface of the Mm and dense collagen rich submucosa (SM), a third hyperechoic layer is present. The

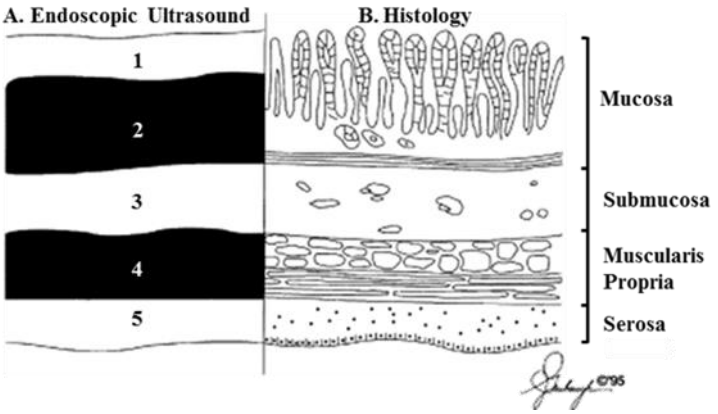

Figure 1.5A-B. Illustration of the bowel wall layers by conventional endoscopic ultrasound frequency (A) and histology (B). Scanning human bowel at frequencies in the range 7 - 12 MHz will produce five distinct signals corresponding to the cardinal histologic layers (i.e. Mucosa, Submucosa, Muscularis Propria and Serosa). Hyperechoic (white) and hypoechoic (black) ultrasound signals are thought to arise from the interfaces between adjacent tissue layers as well as the internal composition of each layer [2]. Illustration adapted from P. R. McNally [55].

signal transitions into a fourth hypoechoic layer at the muscularis propria (MP). The fifth hyperechoic layer represents the serosa (S) which often contains hyperechoic fat.

The prevailing hypothesis on ultrasonic layer generation was proposed by Kimmey *et al* and published in 1989 [56]. The authors hypothesised that an US bowel wall image is the result of two echogenic sources. The first echogenic source is an acoustic (i.e. impedance) mismatch interface between tissue layers. The second echogenic source is the internal composition of each layer with stiffer materials (e.g. collagen) producing hyperechoic reflections. Despite the frequent referencing of this seminal article, the exact relationship between US layers and histology is not universally accepted [57]. The origin of the controversy centres on whether the US layers conveniently correspond directly to histology or are artefacts created by tissue interfaces which generates an image based on the physical properties of the tissue [58], [59]. By the authors' own admission, US technology of 1989 was too underdeveloped to definitely answer the question. Furthermore, the limits of image resolution prevented exact correlation of ultrasonic layers to histologic layers.

It has been 30 years since Kimmey's article was published, yet the controversy still remains, despite the advancements in US transducer development [57]. An example of a relevant advancement is the application of µUS to the bowel wall. With µUS, histologic sublayers in the form of additional echoic layers become ultrasonically manifest.

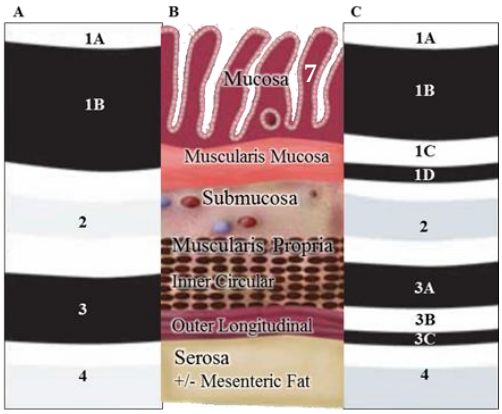

Figure 1.6A-C. Illustration of the bowel wall layers by conventional 7 – 12 MHz frequency (A), histology (B) and high frequency (> 20MHz) ultrasound (C). Higher US frequencies can enhance image resolution and provide a greater level of tissue detail. Conventional ultrasound typically displays 5 ultrasonic layers. High frequency microultrasound can display bowel wall sublayers in the form of additional echoic layers for up to 4 additional layers. This results in a total of 9 layers that can be potentially displayed. Illustration adapted from Ødegaard *et al* [36].

According to Ødegaard *et al*, higher frequencies can manifest up to four additional US layers for a total of nine acoustic layers (Figure 1.6) [36]. At the level of M, the number of distinct layers increases from two to four. At conventional frequencies, M generates an initial hyperechoic layer at the transducer/tissue interface and a deeper hypoechoic layer at the level of the LP. At higher frequencies (e.g. > 20 MHz) the Mm can generate two additional layers to bring the total to four mucosal layers. The Mm produces a second hyperechoic mucosal layer and at the Mm and SM interface, the Mm becomes hypoechoic forming the 4th mucosal signal [36], [60]. The SM is hyperechoic until it interfaces with the inner circular muscle of the MP, where it becomes hypoechoic. At conventional frequencies the MP tends to be a single uniformly hypoechoic layer. However, higher frequencies can resolve the thin fibrous/neural layer separating the inner circular and outer longitudinal muscle as a hyperechoic stripe [36], [60]. The final layer is hyperechoic serosa (S). The echogenic properties of this layer can be further augmented with the presence of mesenteric fat.

Evidence supporting Ødegaard's conclusion regarding the increase of ultrasonic layers have been reported. For instance, Wiersema described 7 layers when scanning the stomach, colon and rectum at 25 MHz [61]. Yoshino and colleagues reported that they could visualise 7 US layers from the M to SM using a 30 MHz endoscopic US probe on the stomach [60]. However, they concluded that visualisation beyond the SM was not possible due to US attenuation by the tissue. Despite the inconsistencies of the published results, it is evident that higher US frequencies can resolve and present additional

ultrasonic layers. The enhanced resolution of µUS transducers can potentially assist in correlating ultrasonic layers with histologic layers.

1.4.4. Ultrasound and Pathology

Tissue undergoing pathologic changes has the potential to have its acoustic properties affected. Merriam-Webster defines pathology as the "the structural and functional deviations from the normal that constitute disease or characterize a particular disease" [62]. Structural abnormalities associated with disease can alter the tissue architecture and compositional elements of tissue. These in turn may affect US interaction with the tissue as image generation is dependent on tissue properties [35]. Pathologic changes have the potential to affect a number of echogenic parameters depending on the disease aetiology (e.g. cancer or inflammation).

Potential changes can include acoustic impedance modification through shifts in tissue density and stiffness. Signal attenuation will change as the number of scatterers deviates from normal. It has been demonstrated by Fatehullah *et al* that µUS is capable of detecting premalignant changes in mutant adenomatous polyposis coli ($Apc^{Min/+}$) mouse small bowel [63]. Pathologic changes that accompany $Apc^{Min/+}$ include the development of multiple adenomas (e.g. polyps) which includes cellular proliferation and abnormal tissue architecture. While the authors stated they could reliably image visible polyps with µUS, they also concluded that architectural changes could be detected prior to histological manifestation. This was a result of modified acoustic impedance and backscatter properties of the tissue. Furthermore, results could be presented in an objective and quantitative manner as measurements are based on the physical properties of tissue. This implies data interpretation does not rely solely on subjective interpretation of images. These results indicate that µUS can be applied to acute inflammation where the hallmark change is massive influx and aggregation of immune cells.

1.5. High Resolution USCE and GI Diagnosis

Combining high resolution µUS with capsule based endoscopy to form USCE can potentially improve the diagnosis and management of GI disorders. The transmural nature of µUS imaging would overcome the surface only imaging capabilities of standard CE. This benefit is particularly well suited for the assessment of treated CD where normal (i.e. healed) mucosa, with a normal appearance, can harbor residual disease. Furthermore, full GI tract assessment would provide information on a pan-enteric disorder that is not

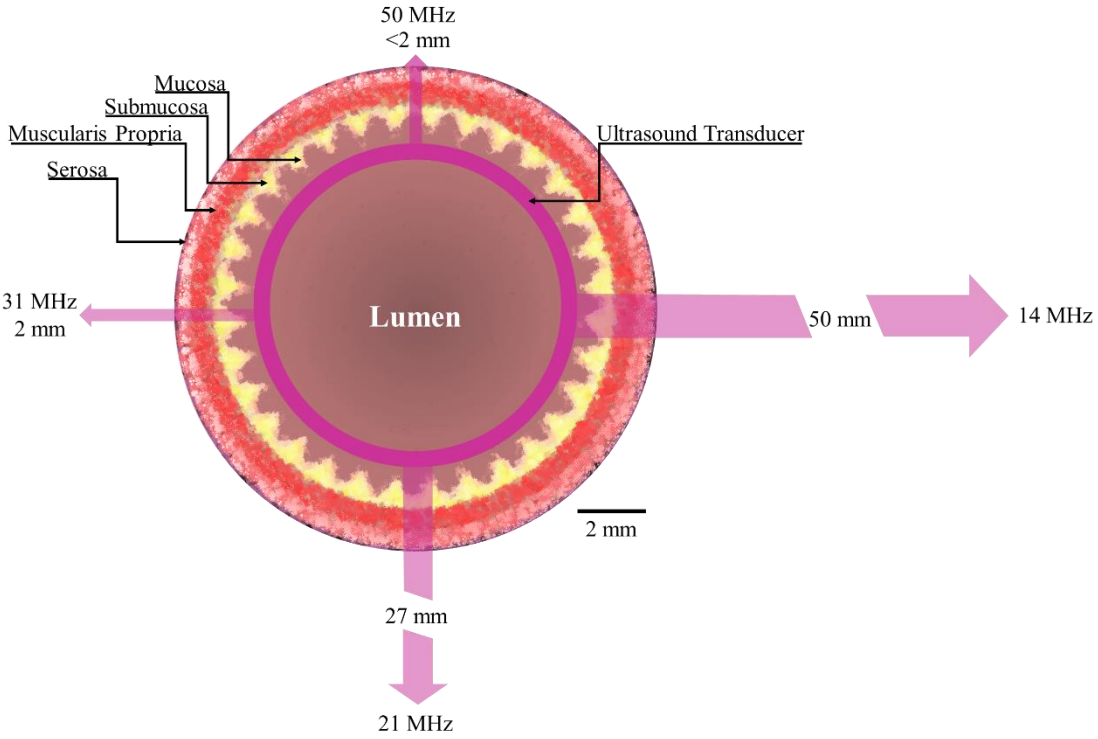

Figure 1.7. Schematic of ultrasound resolution and relative tissue penetration depicted from the lumen of the bowel outwards. There is a twofold effect as the ultrasound frequency is increased which includes enhanced axial and lateral resolution and decrease in tissue penetration as indicated by scaled purple arrows. The major advantages of using microultrasound in ultrasound capsule endoscopy (USCE) is high resolution transmural imaging which is focused on the bowel wall. Image adapted from Cox *et al* [64].

normally available with conventional endoscopy. The ability to fully assess disease activity would provide clinicians with a means of making better informed management decisions. High resolution transmural imaging would also provide a means of determining treatment response at a microscopic level. This would facilitate the goal of achieving a complete response and provide patients with the benefits that accompany histological remission.

Another benefit of µUS is the fast attenuation of high US frequencies as they travel through tissue. The limited penetration makes µUS well suited for imaging the gut wall from a USCE perspective. The decreased depth will maintain a narrow region of interest (i.e. the gut wall) as compared to conventional frequencies (Figure 1.7) [65]. The advantage of limited tissue penetration is that it may prevent adjacent structures (e.g. neighbouring bowel loops) from falsely presenting as oedematous (i.e. thickened) bowel. A narrow window permits each bowel section to be evaluated independently for signs of disease. The subject of conventional US assessment of CD will be discussed at greater length in Chapter 2.

1.6. Thesis Outline

Chapter 2 discusses aspects of the human GI tract gross anatomy and microstructure (i.e. histology). This is followed by a review of GI immune biology including acute inflammation and the histology of CD. Finally, various imaging modalities pertaining to CD are reviewed.

Chapter 3 describes the materials and methods used throughout the thesis. The materials section includes an account of the three models used. It also provides a description of the μUS transducers and associated equipment. Methods for inducing inflammation, μUS scanning and data analysis are included.

Chapters 4, 5 and 6 present results. Chapter 4 presents results from μUS scans of explanted human tissue experiments. Chapter 5 summarises the results from the *ex vivo* and *in vivo* pig experiments in terms of USCE development. Chapter 6 presents mouse results and includes μUS data, histology and comparison of the two methods.

Chapter 7 discusses the overarching research theme of this thesis and draws conclusions from the results of all three models, also outlining possible future research directions.

1.7. Contributions to Knowledge

The work described in this thesis has contributed to knowledge and development of USCE.

Three tissue types were used to test different aspect of USCE design and function.

Ex vivo human tissue results indicated that a centre frequency of ≈35 MHz could provide high resolution transmural images. Up to nine acoustic layers were noted on scans, which agreed with published results. These results suggested that ≈35 MHz would be suitable for inclusion into USCE. Human tissue scans also provided a means of further examining the acoustic-histologic layer relationship. By scanning the tissue in a nonstandard orientation, a novel and independent means of scanning tissue layers was established. Scan results were also compared with histology, the gold standard of tissue analysis, for the purposes of exploring concepts in virtual biopsy.

In vivo pig experiments were successfully used to demonstrate that USCE was capable of generating bowel images. It was demonstrated that contact between the tissue mucosa

and capsule µUS transducer was achieved. Contact permitted generation of capsule-based *in vivo* µUS images of the GI tract. Pig experiments concluded with a successful demonstration of an early USCE prototype.

Ex vivo mouse bowel experiments involving induction of GI inflammation showed that ultrasound at a frequency of ≈35 MHz was capable of detecting high grade inflammation. Further experiments demonstrated that low grade inflammation exceeded the capabilities of ultrasound in the range 35 - 62 MHz, thus excluding these frequencies from further consideration in future.

1.8. Publications and Related Material Arising From This Thesis

Peer Reviewed Journal Articles:

First Author:

B.F. Cox, F. Stewart, H. Lay, G. Cummins, I.P. Newton, M.P. Y. Desmulliez, R.J. C. Steele, I. Näthke, S. Cochran., "Ultrasound capsule endoscopy: sounding out the future," Ann. Transl. Med., vol. 5, no. 9, pp. 201–201, May 2017. DOI: 10.21037/atm.2017.04.21

Contributing Author:

S. Yang, B.F. Cox , C. Lemke, I. Näthke, S. Cochran, I.P. Newton., "A Deep Learning for a Computer-aided Microultrasound System," IEEE TMI. *Manuscript submitted* (TMI-2020-0371)

Y. Qiu, Y. Huang, Z. Zhang, B.F. Cox, R. Liu, J. Hong, P. Mu, H.S. Lay, G. Cummins, M.P.Y. Desmulliez, E. Clutton, H. Zheng, W. Qiu, S. Cochran., "Ultrasound capsule endoscopy with a mechanically scanning micro-ultrasound: a porcine study," Ultrasound Med. Biol., vol. 46, no. 3, pp. 796–804, Mar. 2020. DOI: 10.1016/j.ultrasmedbio.2019.12.003

J.C. Norton, P.R. Slawinski, H.S. Lay, J.W. Martin, B.F. Cox, G. Cummins, M.P.Y. Desmulliez, R.E. Clutton, K.L. Obstein, S.Cochran and P.Valdastri., "Intelligent magnetic manipulation for gastrointestinal ultrasound," Sci. Robot., vol. 4, no. 31, p. eaav7725, Jun. 2019. DOI: 10.1126/scirobotics.aav7725

G. Cummins, B.F. Cox, G. Ciuti, T. Anbarasan, M.Y.P. Desmulliez, S. Cochran, R.J. Steele, J.N. Plevris, A. Koulaouzidis, "Gastrointestinal diagnosis using non-white light imaging capsule endoscopy.," Nat. Rev. Gastroenterol. Hepatol., Apr. 2019. DOI: 10.1038/s41575-019-0140-z

G. Cummins, B. F. Cox, J. D. Walker, S. Cochran, and M. P. Y. Desmulliez, "Challenges in developing collaborative interdisciplinary research between gastroenterologists and engineers," J. Med. Eng. Technol., 2018. DOI: 10.1080/03091902.2018.1543466

H. Lay, G. Cummins, B.F. Cox, Y. Qiu, M.V. Turcanu, R. McPhillips, C. Connor, R. Gregson, E. Clutton, M.P.Y. Desmulliez, S. Cochran, "*In-Vivo* Evaluation of Microultrasound and Thermometric Capsule Endoscopes.," IEEE Trans. Biomed. Eng., Jul. 2018. DOI: 10.1109/TBME.2018.2852715

F. Stewart, Y. Qiu, H. Lay, I.P. Newton, B.F. Cox, M. Al-Rawhani, J. Beeley, Y. Liu, Z. Huang, D. Cumming, I. Näthke, S. Cochran,. "Acoustic Sensing and Ultrasonic Drug Delivery in Multimodal Theranostic Capsule Endoscopy," Sensors, vol. 17, no. 7, p. 1553, Jul. 2017. DOI: 10.3390/s17071553

J. Faerber, G. Cummins, S.K. Pavuluri, P. Record, A.R.A. Rodriguez, H. Lay, R. McPhillips, B.F. Cox, C. Connor, R. Gregson, R.E. Clutton, S.R. Khan, S. Cochran, M.P.Y. Desmulliez., "*In Vivo* Characterization of a Wireless Telemetry Module for a Capsule Endoscopy System Utilizing a Conformal Antenna," IEEE Trans. Biomed. Circuits Syst., pp. 1–11, 2017. DOI: 10.1109/TBCAS.2017.2759254

G. Cummins, D. E. Yung, B. F. Cox, A. Koulaouzidis, M. P. Y. Desmulliez, and S. Cochran, "Luminally expressed gastrointestinal biomarkers," Expert Rev. Gastroenterol. Hepatol., vol. 4124, no. 2008, pp. 1–16, Sep. 2017. DOI: 10.1080/17474124.2017.1373017

Book Chapter:

T. Anbarasan, C.E.M. Démoré, H. Lay, M.R.S. Sunqrot, R. Poltarjonoks, S. Cochran, B.F. Cox.,. "High Resolution Microultrasound (μUS) Investigation of the Gastrointestinal (GI) Tract," Methods Mol Biol. 2017;1572:541-561. DOI:10.1007/978-1-4939-6911-1_34

Conference Proceedings:

H. S. Lay, B. F. Cox, V. Seetohul, C. E. M. Demore, and S. Cochran, “Design and Simulation of a Ring-Shaped Linear Array for Microultrasound Capsule Endoscopy,” IEEE Trans. Ultrason. Ferroelectr. Freq. Control, pp. 1–1, 2018. DOI: 10.1109/TUFFC.2018.2794220

F. Stewart, A. Verbeni, Y. Qiu, B.F. Cox, J. Vorstius, I.P. Newton, Z. Huang, A. Menciassi, I. Näthke, S. Cochran., “A Prototype Therapeutic Capsule Endoscope for Ultrasound-Mediated Targeted Drug Delivery,” J. Med. Robot. Res., vol. 03, no. 02, p. 1840001, Jun. 2018. DOI: 10.1109/ULTSYM.2015.0189

F. Stewart, A. Verbeni, Y. Qiu, B.F. Cox, J. Vorstius, I.P. Newton, Z. Huang, A. Menciassi, I. Näthke, S. Cochran., “A Prototype Therapeutic Capsule Endoscope for Ultrasound-Mediated Targeted Drug Delivery,” J. Med. Robot. Res., vol. 03, no. 02, p. 1840001, Jun. 2018. DOI: 10.1109/ULTSYM.2015.0189

B. F. Cox, V. Seetohul, H. Lay, and S. Cochran, “Microultraound and small bowel inflammation: Tissue phantom studies,” in Proc. 2015 IEEE International Ultrasonics Symposium (IUS), 2015, pp. 1–4. DOI: 10.1109/ULTSYM.2015.0304

G. Cummins, H. Lay, B.F. Cox, V. Seetohul, Y. Qiu, F. Stewart, J. Faerber, V. Mitrakos, M. Al Rawhani, J. Beeley, D.E. Watson, R. Poltarjonoks, C. Démoré, I. Nathke, R.J.C. Steele, D.Cumming, M.P.Y. Desmulliez, S. Cochran., “Sonopill: A Platform for Gastrointestinal Disease Diagnosis and Therapeutics,” Proc. 6th Jt. Work. New Technol. Comput. Assist. Surg., no. September, pp. 3–5, 2016.

H. Lay, B.F. Cox, M. Sunoqrot, C.E.M. Démoré, I. Näthke, T. Gomez, S. Cochran., “Microultrasound characterisation of *ex vivo* porcine tissue for ultrasound capsule endoscopy,” J. Phys. Conf. Ser., vol. 797, p. 012003, Jan. 2017. DOI: 10.1088/1742-6596/797/1/012003

Conferences:

T Anbarasan, C. Démoré, H Lay, M Sunoqrot, R Poltarjonoks, S Cochran, B Cox. Development of Small Bowel Tissue Phantom for Microultrasound (μUS) Investigation. Proceedings 11th Congress of ECCO, 2016.

Thineskrishna Anbarasan, Christine E.M Démoré, Holly Lay, Mohammed R. S. Sunoqrot, Romans Poltarjonoks, Benjamin F. Cox, Sandy Cochran. Development of Small Bowel Tissue Phantom for Microultrasound (μUS) Investigation. Proceedings 2015 Royal Society of Medicine-The United Kingdom Medical Students' Association Conference.

Invited Talks:

B.F. Cox., "Multi (-modal) capsules" Invited Speaker "Fluorescence Capsule Endoscopy Workshop (Project No. HTC-16-056)". Colorectal Therapies Healthcare Technology Co-operative, Leeds, UK. 01 December 2017.

B.F. Cox., "Multimodal Capsule Diagnosis: Modalities and Combinations" Invited Speaker: Minimally Invasive Endoscopy Workshop. The Royal Scots Club Edinburgh, 21 March, 2017.

B.F. Cox., "Sonopill Overview" Invited Speaker: Liver/GI Lunchtime Teaching Meeting for Specialist Registrars. Hosted by Dr A. Koulaouzidis – Endoscopy Unit, Royal Infirmary of Edinburgh. February 2016

B.F. Cox., "Capsule sonography – a brief insight of the Sonopill" Invited speaker, An Update on the use of Capsule Endoscopy in IBD. Hosted by Dr A.Koulaouzidis – Endoscopy Unit, Royal Infirmary of Edinburgh, September 2015.

S. Cochran, B.F. Cox, H. Lay., "Ultrasound capsule endoscopy for diagnosis and therapy: A new frontier in autonomous, robotic systems." Invited Speaker, CDT Gateway Events, Heriot-Watt University, November 2014.

Awards:

National Instruments Week 2019 Humanitarian Award ‘Sonopill: The Future of Capsule Ultrasound’ Winner: University of Glasgow, Heriot-Watt University, University of Dundee, University of Leeds

Scottish Health Innovations Ltd. (SHIL) Proof of Principle (PoP) scheme: Henry, E., Cox, B.F., Lay, H., Cochran, S. “Microultrasound (μUS) Surveillance of Barrett’s Oesophagus” (Selected IPR Project: 140904). Awarded £22,500 for 12 months.

2nd Prize, 1st year tissue/dry lab presentations, 26th Annual Postgraduate Research Student Symposium, School of Medicine, University of Dundee, Jun 2016.

Chapter 2: The Gastrointestinal Tract

2. Chapter Introduction

This chapter discusses aspects of the human gastrointestinal (GI) tract beginning with gross anatomy. This is followed by a description of the bowel wall microanatomy (i.e. histology). A review of the immune biology of acute inflammation and how it relates to Crohn's Disease (CD) is introduced. Finally, the various GI tract imaging modalities are reviewed.

2.1. Human Gastrointestinal System

The human digestive system is an organisation of internal organs and is primarily associated with two fundamental tasks: absorption of nutrients and elimination of waste.

2.1.1. Gross Anatomy

The primary component of the digestive system is the GI tract, a hollow tube that begins with the oral cavity (i.e. the mouth) and terminates at the anus. The alimentary canal is grossly divided into sections based on anatomical location. The upper GI tract consists of the mouth, oesophagus, stomach and proximal (i.e. superior and descending) duodenum. The lower GI tract is comprised of the distal (i.e. horizontal and ascending) duodenum and remaining small bowel (i.e. jejunum and ileum). Forming the terminus of the lower GI tract is the colon (i.e. ascending, transverse, descending and sigmoid) which includes the caecum, appendix, rectum and anus.

The total length of the GI tract is estimated to be ≈ 5 m for an average healthy adult *in vivo* [66]. Of that total, roughly $^{2}/_{3}$ is small bowel. Length measurements vary between individuals and are affected by factors such as diet and lifestyle. It should be noted that the *in vivo* measurement differs significantly from often quoted lengths such as 8.0^{+} m which are measured *post mortem* [2]. Differences in measurements have been attributed to the loss of bowel tonality following death. Combining length with the topology of the inner surface, the estimated surface area measures ≈ 32 m^2 [66], [68]. Roughly corresponding with a studio apartment, this is significantly smaller than the tennis court area (i.e. 300 m^2) traditionally quoted [69]. Nevertheless, 32 m^2 represents a substantial area when considering microscale modes of examination. The large surface area aids

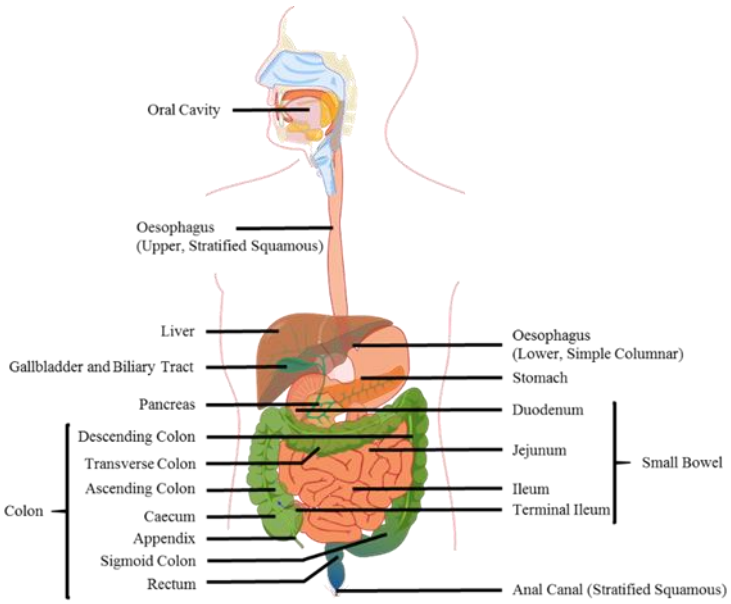

Figure 2.1. Gross anatomy of the human gastrointestinal (GI) system which includes the alimentary canal and accessory organs. Image adapted from Mariana Ruiz, public domain.

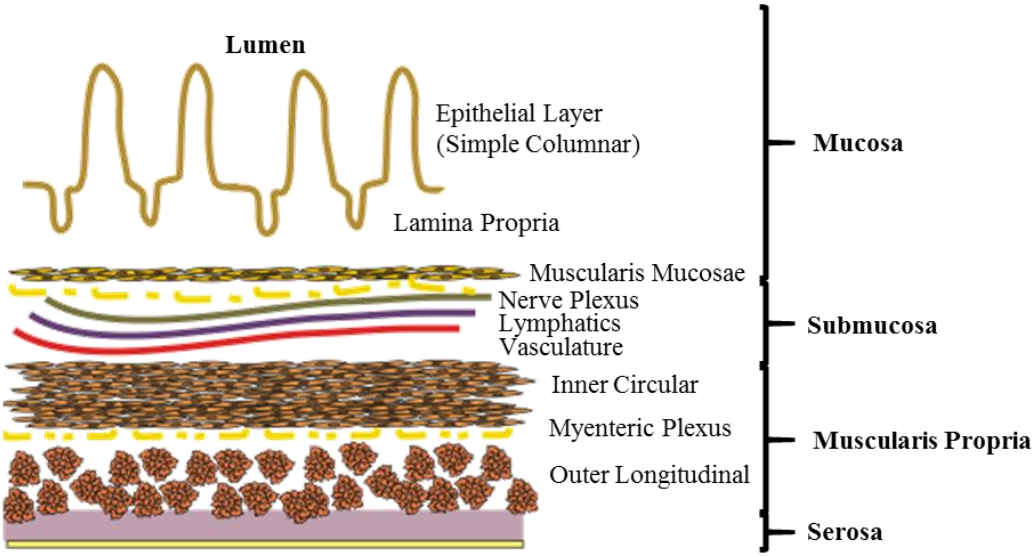

Figure 2.2. Illustration of the general microanatomy of the gastrointestinal (GI) tract which extends from the lower oesophagus to the rectum. The luminal mucosal epithelial layer is lined by a simple (single) layer of columnar cells. Included in the mucosa is the underlying lamina propria and muscularis mucosae. Immediately below the muscularis mucosae lies the submucosa. This is a supporting layer of dense connective tissue housing the precapillary vasculature as well as lymphatics and nerves. The muscularis propria is formed of two distinct layers of involuntary smooth muscle that runs the entire length of the GI tract. The inner circular layer wraps around the wall circumference and the outer, or longitudinal, layer parallels the long axis of the GI tract. The outermost layer is the serosa, a thin membrane of connective tissue and cells. Adapted from Frank Boumphrey, Wiki Commons.

with digestion and absorption of nutrients by enhancing gut wall-to-chyme (i.e. nutrient semifluid) contact. The complete GI system also includes accessory organs aiding in function. These include the tongue, salivary glands, liver plus bile network and pancreas, illustrated in Figure 2.1.

2.1.2. Microanatomy

The microanatomy or histology of the GI tract is remarkably well conserved throughout its length [70]. Cardinal layers, beginning luminally to outermost membrane, are the mucosa, submucosa, muscularis propria and serosa. Figure 2.2 illustrates the general arrangement of the bowel wall which includes the cardinal layers and associated sublayers.

The mucosa (M) is comprised of tall columnar cells arranged as a simple (i.e. single) continuous epithelial layer. This arrangement begins at the squamocolumnar junction, or z-line, at the gastroesophageal junction (GOJ). Prior to the GOJ, the epithelial lining is arranged in a stratified squamous cell (i.e. multi-layered and flat) manner. The simple columnar epithelium then continues until reaching the anal canal and transitions back into stratified squamous epithelia at the pectinate line. The epithelial cells are often referred to specifically as enterocytes and colonocytes, denoting their location in the small bowel and colon respectively. Despite different anatomic locations and nomenclature, columnar cells demonstrate a similar apical-basal polarity arrangement. Sublayers of the mucosa include the lamina propria (LP), a thin layer of connective tissue and the muscularis mucosa, a thin smooth muscle layer delineating the inner border of the mucosa.

Beneath the mucosa lies the submucosa (SM). This is a dense connective tissue rich layer. The SM contains circulatory vessels such as arterioles and venules. These form the capillary networks of the bowel wall. Additionally, located in the SM are the nerve and lymphatic networks. The lymphatics begin in the M and muscularis propria (MP) and drains into the greater lymphatic system via the mesenteric lymph nodes [71]. The MP is formed of two orthogonally orientated layers of involuntary smooth muscle. The inner circular layer runs the entire circumference and length of the bowel wall. The outer or longitudinal layer runs the length of the GI tract.

Deep to the MP is the serosa (S), a thin membrane of connective tissue and a simple squamous layer of mesothelium. In addition to providing support and lubrication, the

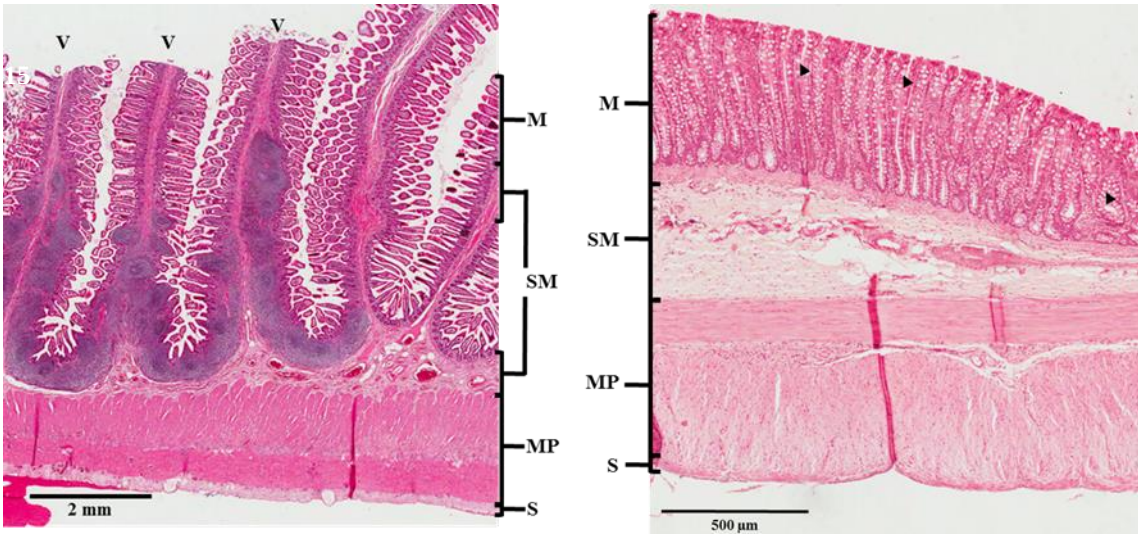

Figure 2.3. Haematoxylin and Eosin (H&E) sections of the human ileum (L) and colon (R). Both slides illustrate the common features of the gastrointestinal tract including the simple columnar lined mucosa (M), submucosa (SM), muscularis propria (MP) and serosa (S). Additionally, the slides indicate tissue specialisation, most notably at the mucosa. The long finger-like projections, i.e. villi (V), of the ileum have the effect of increasing the surface area for the absorption of nutrients. The colon lacks villi but is dominated by mucosal invaginations or crypts. Although present in both sections, the colon is well endowed with mucus secreting goblet cells (arrow heads). Slides courtesy of Dr Paul Felts, CAHID, University of Dundee.

serosa blends with the mesentery. The mesentery serves to tether the bowel to the abdominal wall and provides a conduit for vessels, lymphatics and nerves.

Although the GI tract shares common histologic features, there are morphologic aspects unique to each anatomic section as illustrated in Figure 2.3. General characteristic morphology of the small bowel includes villi. Villi, or finger-like projections, extend into the lumen and enhance the absorptive surface area. Crypts, or short mucosal invaginations, are situated between the villi and play a supportive role in epithelial renewal. The GI tract is noted for its rapid turnover of epithelial cells, estimated at 3.48 ± 1.55 days [72]. Crypts house stem cells responsible for maintaining the epithelial lining and mucosal integrity. The bowel surface also possesses numerous folds, called plicae, along its length resulting in an irregular and uneven surface.

The colon also has a similar uneven mucosal surface. It lacks villi but is dominated by crypt invaginations. The crypts are imbued with numerous mucous secreting goblet cells and house basally located stem cells. Due to the presence of haustra, shallow sack-like folds, the colon appears segmented on gross examination.

2.2. Gastrointestinal Barrier System

In order to carry out its absorptive and elimination functions, epithelial cells must interface with the external environment. Thus, the entire length of the mucosa is considered in contact with an unsterile environment. For instance, a major constituent of the luminal contents are microbes that colonise the GI tract. In fact, the human colon alone is considered one of the most densely inhabited environments due to the estimated 10^{12} organisms per millilitre of luminal contents [73]. As a result, the GI tract represents a potential route for microbial insult and invasion. To combat this ever present risk, the entire bowel length is endowed with a highly sophisticated and regulated means of immune defence, response and tolerance.

Component	Characteristics	Function
Mucosal Epithelium (Simple Columnar Lining)	• Uninterrupted the entire length of GI tract • Neighbouring cells bound by tight junctions • Cells firmly anchored to mucosal basement membrane • Continual replacement of epithelium • Discriminatory between beneficial and noxious material (Positive and Negative Selection)	Selective Barrier
Mucus (Secreted by epithelial Goblet Cells)	• Microbial trap (Negative Selection) • Facilitates elimination of microbes • Positive selection for beneficial nutrients • Reduction of shear stress (Reduced Friction)	Selective Impediment and Mucosal Integrity Maintenance
1. Microfold Cells (Specialised Epithelial Cells) 2. Paneth Cells (Differentiated Epithelial Cells)	• Interaction/Communication with immune cells • Role in immune response and tolerance • Luminal secretion of polymeric IgA • Antimicrobial peptides (e.g. defensins)	Immune Surveillance and Neutralisation of Noxious Material
Gut Associated Lymphoid Tissue	• Organisation of GI associated immune component • Inductor Sites (e.g. Tonsils, Peyer's Patches) house naïve and memory lymphocytes. Area of adaptive immune initiation • Effector site (e.g. Lamina Propria) represents primary area of immune cell migration and accumulation	Immune Surveillance, Response and Tolerance
Innate Immune Cells 1. Monocytes/Macrophages 2. Neutrophils	1. Immune surveillance; initiation, maintenance and resolution of Inflammation 2. Rapid response, accumulation and maintenance; immune clearance	First Responders in Acute Inflammation Rapid Clearance of Noxious Stimuli Antigenic Nonspecific Response
Adaptive Immune Cells Lymphocytes	• Immune modulation (e.g. response or tolerance), memory and antibody synthesis	Delayed Responders in Acute Inflammation Antigenic Specific Response Immune Memory

Table 2.1. Gastrointestinal (GI) tract organisation and function of barrier components.

The GI tract must transfer material to and from this hostile environment. To facilitate this function, the luminal surface acts as a selective barrier. The selectivity allows for the absorption of essential elements whilst simultaneously preventing ingress of noxious elements. Barrier function of the mucosa involves multiple components both inherent to the bowel wall itself as well as elements of the immune system (Table 2.1).

As previously discussed, the epithelium of the mucosa forms a continuous layer. This layer physically prevents ingress of unwanted molecules and microbes. The major barrier component are the apicolateral tight junctions, which securely bind cells to one another and facilitate selective transport [74]. Selective transport through the enterocyte barrier is achieved through transcellular (e.g. receptor mediated endocytosis) and paracellular

routes. Highly discriminatory, the transcellular route is responsible for the intake of nutrients such saccharides and amino acids. The paracellular route is generally restricted to molecules that are <500 kDa and are charged (e.g. cation or anion), which includes common electrolytes (e.g. Na^+ or Cl^-). Enterocytes are firmly anchored to the underlying tissue via the basement membrane [70].

Augmenting the epithelial barrier is the luminal mucous layer. Secreted by goblet cells, the mucous layer comprises glycoproteins termed mucin. Forming a viscous apical coating, mucus reduces shear stress on the mucosal layer incurred by passage of luminal contents. Mucus glycoproteins also function as a filter to trap noxious material and facilitate its eventual elimination [75]. Simultaneously mucus permits diffusion of required nutrients to the epithelial cells [76].

The barrier role of enterocytes is not limited to a physical barrier role. They also play an important role in communicating with resident immune cells of the GI tract. Communication with the immune cells is largely the role of specialised enterocytes called microfold cells (M-cells) [77]. These specialised epithelial cells are devoted to sampling luminal contents and presenting potential antigens to closely associated immune cells [78], [79]. Antigen presentation by M-cells is thought to play a role in inciting an immune response or immune tolerance [80], [81]. Enterocytes are also responsible for translocating secretory immunoglobulin A (sIgA) into the gut lumen. [82], [83]. The function of IgA is to neutralise toxins, inhibit viral attachment, block bacterial mucosal adherence and play a role in immune cell activation [84]. Immunoglobulins are synthesised by plasmocytes (i.e. mature B-cell) which form a large resident population in the LP of the GI tract [85], [86].

2.2.1. Immune Component of the Barrier System

The overall function of the mucosal immune system of the GI tract is to respond to potential pathogenic threats and forms a critical component of the barrier system. The immune system is a highly complex system involving numerous components (e.g. antimicrobial molecules, cells and mediators) to protect the host from infection and disease. Complicating the role of the immune component is the need to discriminate between beneficial elements (e.g. nutrients and gut commensals) and noxious elements (e.g. bacterial or viral pathogens). The former should not stimulate an immune response

(i.e. tolerance) while performing its absorptive function. However, the latter should elicit an appropriate inflammatory response to antigen challenge.

The primary aim of this thesis is to determine if microultrasound (μUS) is capable of detecting an acute inflammatory response. The following sections will focus on aspects of the immune system as it relates to an acute inflammatory response.

Gut Associated Lymphoid Tissue

Due to its close proximity to the external environment, the immune component of the GI tract represents one of the largest pools of lymphoid tissue in the human body. During steady state (i.e. healthy) conditions it is estimated that the gut hosts upwards of 70-80% of the total lymphocyte population [87], [88]. This equates to a mass of 10^6 lymphocytes/g of tissue [88].

Gut Associated Lymphoid Tissue (GALT) is specific to the GI tract and pertains to the cellular and structural organisation of the immune component. It is possible to define GALT using different criteria including anatomical compartments and site specific mechanisms. Compartmentally, GALT ranges from highly organised tissue to more diffuse elements [89]. Organised elements include lymphoid aggregates that include the tonsils, appendix, Peyer's Patches (PP), mesenteric lymph nodes (MLN) and isolated lymphoid follicles [90][91]. Diffuse elements include the scattered resident immune cells of the LP. Mechanistically, GALT may be divided into inductor and effector sites. Inductor sites are where naïve lymphocytes are primed for response and include GALT sites such as MLNs. Effector sites represent the major sites of immune cell migration, aggregation and antimicrobial activity during the process of acute inflammation. The major effector site of the gut is the LP [92].

Immune Cells

Immune cells are derived from bone marrow (BM) precursors that migrate to the GI tract. Even under healthy conditions, migration is a continuous process in order to maintain steady state levels of immune cells. Maintaining sufficient cell numbers is necessary to mount a fast and effective inflammatory response [93]–[95]. The immune component of the gut wall consists of cells from the myeloid line (e.g. neutrophils, monocytes, eosinophils and basophils) and lymphoid line (e.g. Natural Killer, B and T cells). Immune cells can be further grouped into innate and adaptive components. The former includes

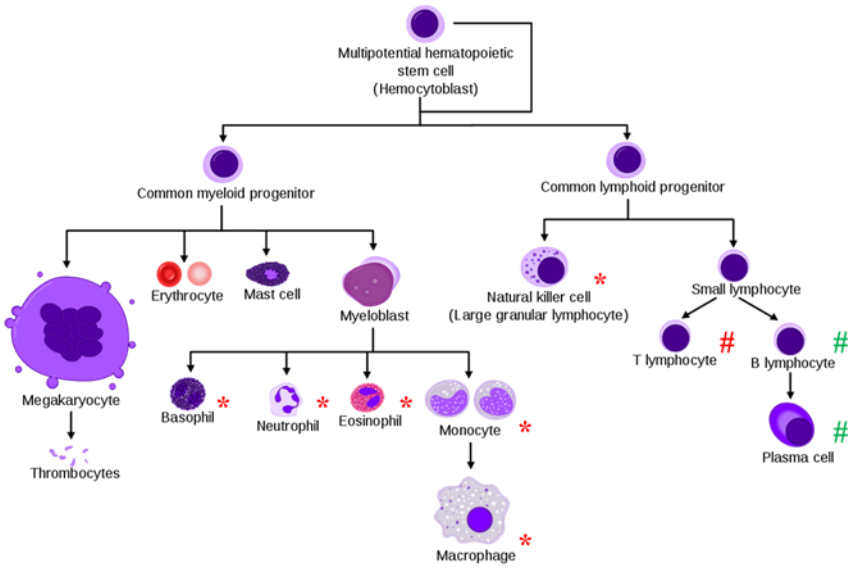

Figure 2.4. The immune component of the gut wall consists of cells of both innate and adaptive lines. These cell lines are derived from bone marrow progenitor cells and include lineages from the myeloid line (neutrophils, monocytes, eosinophils and basophils) and lymphoid line (Natural Killer, B and T cells). Immune cells can be further divided by grouping cells into innate (*) and adaptive components (#). The adaptive component can be subdivided into cell mediated (#) and humoral (#) responders. Image by Mikael Häggström, Public Domain.

cells of the myeloid and lymphoid lines whilst the latter includes the lymphoid line and can be subdivided into humoral and cell mediated immune response (Figure 2.4.).

The differentiation between innate and adaptive relates to time of response, specificity of response and antigenic memory. Innate cells can mount a rapid but non-specific response to a noxious stimulus. This is due to their ability to inherently recognise pathogens or damaged tissue. The adaptive, or acquired, immune arm is able to mount a specific antigenic response. However, antigen specificity requires time to develop, and results in delayed response as opposed to the rapid response of the innate component. While the innate response can be measured in hours, a naïve adaptive response requires days. Notably, the adaptive immune component possesses antigen memory so that subsequent exposure to a specific antigen elicit a faster response [29].

Innate Immune Cells

Cells of the innate arm are intrinsically able to recognise external threats and internal damage. This is facilitated by Pattern Recognition Receptors (PRR). These germ-line encoded receptors allow innate cells to rapidly recognise and respond to an insult. These receptors are not only expressed by innate immune cells but also epithelial cells such as M-cells [96]. Several classes of PRRs exist and are grouped according to cellular location

(e.g. membrane or cytosolic), ligand and function [97]. These receptors can recognise and bind to conserved structures on microbes. Conserved structures include bacterial lipopolysaccharide (LPS), flagellin and nucleic acids of viral and bacterial origin. Collectively, microbial associated PRR ligands are termed Pathogen-Associated Molecular Patterns (PAMPS). Well characterised examples of PRRs are Toll-Like Receptors (TLR). Upon binding to a recognised ligand, transmembrane TLRs will dimerise and activate transcription pathways necessary for initiating the inflammatory process [98].

In addition to exogenous ligands, there are endogenous danger signals associated with tissue damage. Such molecules are Damage-Associated Molecular Patterns (DAMPs). Released during periods of cellular stress (e.g. infection) or damage (e.g. necrosis), DAMPs represent either intracellular molecules (e.g. histones) or extracellular matrix fragments [99]. As with PAMPs, DAMPs are highly conserved molecular structures and can be recognised by PRRs. Under non-inflammatory (i.e. steady state) conditions, DAMPs are normally sequestered from interaction with PRRs to prevent inappropriate initiation of the inflammatory process [99]. During periods of cell stress (e.g. infection), DAMPs are released permitting PRR-DAMP interaction and eliciting an immune response by activating immune cells [100].

Mononuclear Monocytes

Mononuclear monocytes include circulating undifferentiated monocytes, tissue resident macrophages and dendritic cells. The latter two represent mature and tissue fixed monocyte subsets found in a number of epithelial linings (e.g. skin, respiratory and GI). Tissue-specific residential macrophages/dendritic cells are often referred to with specialised names such as Kupffer (Liver) and Langerhans (Epidermis) cells. This indicates that resident monocytes can differentiate into tissue specific subsets according to location and function [101].

Monocytes are located along the length of the GI tract with the highest concentration in the colon [102]. Histologically, the highest density of monocytes is found in the LP [103]. This arrangement relates to their surveillance function against barrier breaches and early responding effector cells. Despite their varied phenotypes, monocytes are considered specialised (i.e. professional) antigen presenting cells (APC) functionalised to display antigens to other cells (e.g. effector or regulatory cells). This is mediated with Major Histocompatibility Complex (MHC) II, also known as Human Leukocyte Antigen (HLA)

II [104]. Presentation of antigen is predominately achieved through phagocytosis of endogenous (e.g. cellular debris) or exogenous (e.g. bacterial components). Following engulfment, the antigen is processed and presented at the cell surface bound to MHC II and associated with co-stimulatory molecules such as CD40 and B7 [10]. Antigen presentation allows APCs to interact with other immune cells including that of adaptive arm. In this regard, APCs function as a link between the two immune system components.

Neutrophils

Polymorphonuclear (PMN) leukocytes include neutrophils, eosinophils and basophils. Neutrophils represent the most abundant white blood cells in circulation and typically make up to 70% of cells in a complete blood count (CBC) [105].

Upon maturation, neutrophils are released from the bone marrow into the circulatory system. They have a short half-life of approximately 6 - 8 hours and a daily turnover rate of 5×10^{10} –10 $\times10^{10}$ cells/day at steady state [106]. During their short lifespan, neutrophils will remain in circulation until encountering one of two fates. Upon reaching unstimulated senescence, neutrophils will undergo apoptosis and are cleared by macrophages in the liver, spleen or bone marrow [106]. The short life-span is thought to control cells numbers and, in turn, control the potentially destructive nature of neutrophils [106], [107]. Notably, neutrophils are considered rare in non-inflamed tissue [87], [108], [109]. For instance, it is estimated that < 5 neutrophils per high power field (hpf) reside in the appendix under baseline (i.e. healthy) conditions [110]. The alternate fate of neutrophil activation, migration (i.e. tissue accumulation) and antimicrobial mechanisms will be discussed in the next section.

2.3. Inflammatory Response

An inflammatory response is a biological response to noxious stimuli mediated by the immune system (Figure 2.5). It is a complex and highly coordinated process involving the previously discussed immune cells. The purpose of an immune response is to rapidly neutralise and remove the insult. The final endpoint is to return to the system to baseline form and function upon resolution.

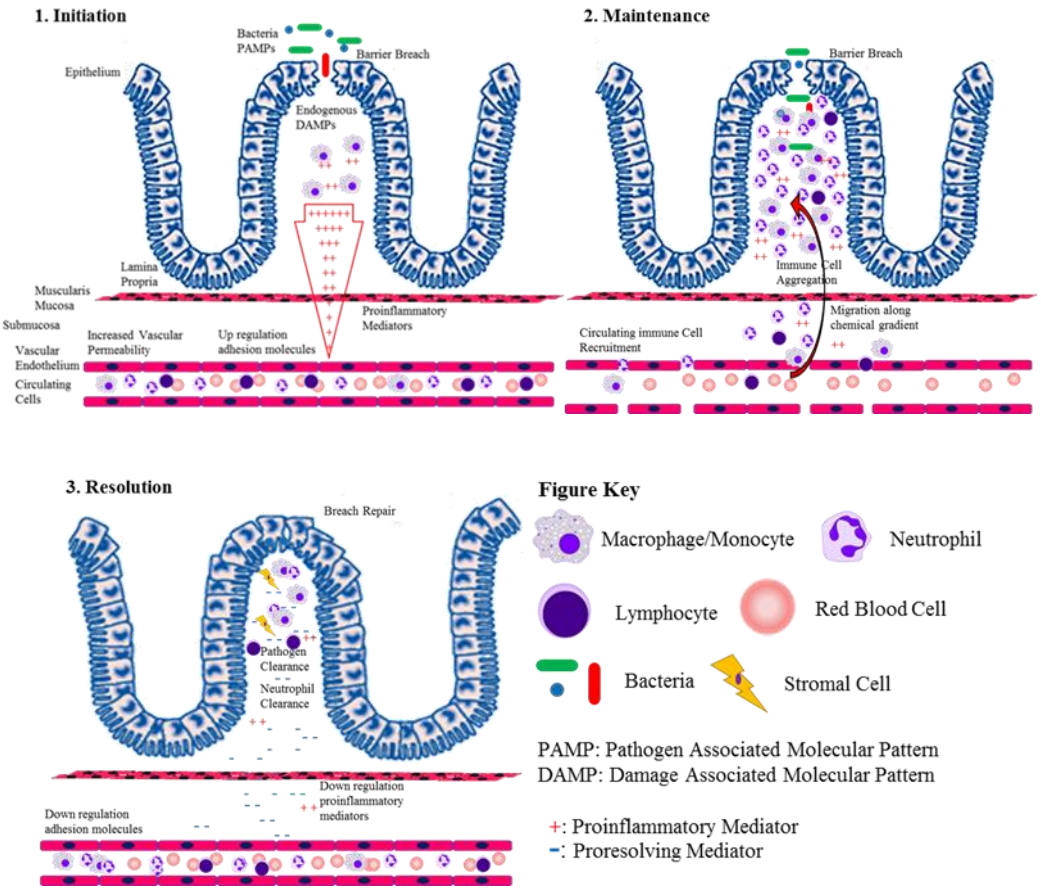

Figure 2.5. Stages of the acute inflammatory process involving cells of the innate and adaptive immune system. The stages involved are 1. Initiation, 2. Maintenance and 3. Resolution. Initiation begins with a barrier breach in the epithelial lining. Sentinel resident macrophages detect conserved molecular patterns originating from luminal microbes (PAMPs) or endogenous molecules released due to tissue damage (DAMPs). Activated macrophages will release proinflammatory mediators such as Tumour Necrosis Factor Alpha (TNF-α) and Interleukin-1Beta (IL-1β). The mediators will result in vascular endothelial cell upregulation of adhesion molecules and increased permeability. This step is necessary for the recruitment of circulating immune cells such as neutrophils, monocytes and lymphocytes. Cells will extravasate from circulation and migrate along the mediator gradient to the site of injury. The accumulation of immune cells will continue during the maintenance stage until the immunogenic stimulants are cleared. Resolution occurs with clearance of proinflammatory stimuli including endogenous and exogenous debris. Monocytes/macrophages will then clear spent neutrophils and release proresolving mediators such as Transforming Growth Factor-β (TGF-β) and IL-10. These mediators serve to diminish further recruitment by down-regulating adhesion molecules and up-regulating stromal cell activity. Activation of stromal cells (e.g. fibroblasts) initiates the repair process with the intention of returning affected tissue to a functioning baseline condition.

The process of inflammation can be described as either acute or chronic. An acute response induces a rapid proinflammatory cascade of events. This results in an initial swift influx and accumulation of innate immune cells at the site of injury. The duration of an acute response is usually measured in days. A chronic inflammatory response is a

prolonged process that may range in duration from months to years [111]. Persistent immune activation is often attributed to failure to remove immunogenic stimuli as resolution of inflammation is dependent on clearance of immunogenic stimuli [112]. The continual or repeated activation of the immune system is, in itself, a pathologic condition as illustrated by CD [113].

2.3.1. Acute Inflammation

An acute inflammatory response is classically defined as the remit of the innate arm. It is characterised by rapid onset and short duration (Figure 2.6). The stages involved can be described in terms of initiation, maintenance and resolution with characteristic timing of immune cell type infiltration at the LP effector sites [90].

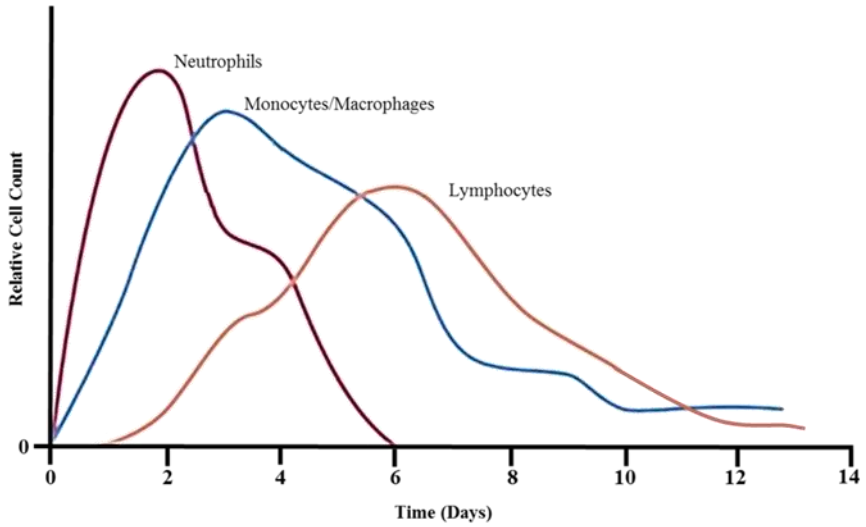

Figure 2.6. Relative influx and aggregation of immune cells measured in days post barrier injury. Neutrophil influx can be measured in minutes after injury and accumulation will peak by 24 – 48 hours afterwards. Monocytes will then follow in a second wave as a result of neutrophil release of chemoattractants. Second wave migration begins almost immediately post initiation and continues for an extended period of time. By the conclusion of the inflammatory response monocytes represent the predominate cells. Monocytes will interact with the adaptive arm, resulting in B- and T-cell priming, activation and differentiation. Activated lymphocytes will then infiltrate and accumulate at lamina propria effector sites. Adapted from Witte and Barbul [114].

Initiation

Initiation begins when an exogenous or endogenous stimulus is encountered and phagocytosed by sentinel tissue macrophages. This triggers the recruitment of circulating monocytes and neutrophils as well as activation and expansion of the adaptive immune system.

Activation of sentinel tissue fixed macrophages results in expression and release of proinflammatory mediators that are responsible for further leukocyte recruitment. Among the first effects of the proinflammatory mediators (e.g. TNF-α, IL-β) is activation of post capillary endothelial cells (ECs). Activated ECs release chemoattractants responsible for immune cell recruitment. These molecules promote and direct immune cell migration to the site of injury. The gradient establishes a 'homing signal' to attract and recruit circulating leukocytes. Stimulation of ECs will also result in upregulation of adhesion molecules necessary for the arrest and migration of immune cells into the affected area [115]–[117]. Another notable effect of EC activation is increased vascular permeability to facilitate leukocyte extravasation. This also results in net fluid movement into the injured area causing the familiar swelling (i.e. oedema) that accompanies inflammation [118].

During periods of inflammation, the circulating neutrophil numbers can be increased upwards of 10-fold [119]. This is achieved by releasing bone marrow reserves into circulation and enhancing bone marrow production [120]. During the initial phase of inflammation, neutrophils migrate and accumulate in the area of invasion/injury. This effect occurs within minutes and peaks by 24 – 48 hours [121]. Peripherally circulating PMNs detect and follow a chemical gradient through chemotactic navigation. Upon localising and arresting at the site of injury, PMNs extravasate from circulation and migrate to the LP where neutrophils aggregate and cluster in a process called 'neutrophil swarming' [122]. These swarms may be temporary (10 - 40 minutes) or persistent (> 40 minutes) in nature. Cell numbers are in the range approximately 10 - 150 neutrophils for temporary swarms and > 300 neutrophils for persistent swarms.

Because of experimental limitations, delineating the *in vivo* spatiotemporal dynamics of swarming remains poorly understood [123]. This includes calculating cell density per swarm. However it is known that neutrophils are required to reach a critical neutrophil concentration (CNC) to control bacterial growth [124]. Li *et al* estimated that a CNC of 4×10^6 - 8×10^6 neutrophils/ml at the dermis is necessary for bactericidal activity.

Cybulsky *et al* demonstrated a 150 fold increase in neutrophil population within 4 hours of intradermal injection into antigen rabbits [125]. Although the two aforementioned experiments are limited to the dermis, they illustrate the rapid accumulation of neutrophils at the site of insult during the process of inflammation.

During this phase, monocytes interact with the adaptive arm resulting in B- and T-cell priming, activation and differentiation [126]. Post activation, antigen specific B- and T-lymphocytes undergo selection, clonal expansion and proliferation [127]. Clonal expansion is estimated to occur by a factor of 2 - 4 times within a 24 hour period. Completion of expansion is estimated to take 4 - 5 days explaining the delay in the adaptive response. It is estimated that a single antigen specific cell will gives rise to a thousand or more daughter clones [84], [127], [128]. Activated lymphocytes then migrate and accumulate at injured LP effector sites [92].

Maintenance

Upon establishing an initial response, the immune system will enter the maintenance phase. During this phase the response is amplified through positive feedback mechanisms. Arriving neutrophils undergo a transcriptional burst, resulting in *de novo* synthesis and release of proinflammatory cytokines such as IL-8 [129], [130]. This results in further neutrophil recruitment as well as recruitment of circulating monocytes. The second wave of monocyte infiltration has important repercussions in determining the outcome of the inflammatory response. Upon arrival, monocytes will differentiate to become either proinflammatory (Classical M1) or immune suppressive (Alternative M2) [131]. Principally, proinflammatory monocytes function to amplify and sustain the immune response through further neutrophil/monocyte recruitment [132]. The latter suppressive role will be discussed in the section on resolution.

Initially, neutrophil migration to the site of injury exceeds monocyte numbers. However, second wave migration begins almost immediately post initiation and continues for a longer period of time [133]. By the conclusion of the inflammatory process monocytes represent the dominant cell type in a lesion. This phenomenon is most likely explained by the role of monocytes in all stages of inflammation including the cessation of inflammation [102]. The dynamics of the maintenance phase are linked to antigen load and will continue until antigen clearance has been achieved. Upon elimination of the stimulus, the immune response enters the resolution phase.

During the inflammatory response, nonspecific microbial clearance is achieved via a number of different mechanisms (Table 2.2). Neutrophil antimicrobial mechanisms include antigen phagocytosis, oxygen radical release, antimicrobial molecules (e.g. proteolytic enzymes) and the formation of neutrophil extracellular traps (NETs) [129], [134]. The synthesis and release of reactive oxygen species (ROS) occurs during 'oxidative burst'. Catalysed by NADPH oxidase and myeloperoxidase (MPO), oxidative burst results in production of destructive oxygen radicals such as superoxide anion (O_2^-), hydrogen peroxide (H_2O_2), and hydroxyl radicals ($HO\cdot$).

As summarised in Table 2.2, neutrophils possess ample means of bacterial elimination and are well suited to their primary role. However, these antimicrobial 'weapons' are nonspecific and pose a threat to host tissue. Collateral host tissue damage has been linked to the oxygen radicals and proteolytic enzymes [121].

Family	Enzymes	Product/Function/Target
Proteolytic Enzymes	Matrix Metalloproteinase (MMP) MMP-2 MMP-8 MMP-9	 Gelatinase (Collagen IV) Collagenase (Collagen I, III) Gelatinase (Collagen IV)
	Serine Proteases Cathepsin G Elastase Protease-3	 Elastin Fibronectin Laminin Vitronectin Collagen IV
Oxidant Generation	NADPH Oxidase Myeloperoxidase (MPO)	Superoxide ($O_2\cdot$) Hydrogen Peroxide (H_2O_2) Hypochlorous Acid (ClOH) Hypothiocyanous acid (CHNOS) Chloramines (R-NHCl) Organic radicals

Table 2.2. Selected neutrophil antimicrobial products implicated in collateral tissue damage. During the inflammatory response, neutrophil killing of microbes is achieved via a number of different mechanisms. Primary mechanisms include phagocytosis and release of proteolytic enzymes. During oxidative burst neutrophils will synthesise and release a number of reactive oxygen species (ROS). Both proteolytic enzymes and ROS are involved in damage to host (i.e. self) tissue due to the non-specific nature of the anti-microbial products. Adapted from Wilgus [135] and Winterbourne [136].

ROS are inherently unstable and biochemically indiscriminate. These molecules will damage exogenous and endogenous molecules such as lipids, proteins and nucleic acids. This can result in self-cell death via apoptotic or necrotic pathways due to oxidative stress [136]–[138]. Protective enzymes such as catalase and glutathione peroxidase can counteract the deleterious effects of ROS. Further protection comes in the form of free radical scavengers (i.e. antioxidants), which include glutathione and diet derived

antioxidants (e.g. vitamins A, C and E). However, during an inflammatory state, such protective measures may be overwhelmed, tipping the balance to favour oxidative stress induced damage. This imbalance can result from an excessive or prolonged inflammatory response [64], [69].

Many of the enzymes released by neutrophils are nonspecific and can attack endogenous as well as exogenous targets. Included amongst the proteolytic enzymes are serine proteases and matrix metalloproteases (MMP). These proteases will degrade the supporting structural extracellular matrix (ECM) and basement membrane [135]. Although this phenomenon has been implicated in aiding neutrophil migration to wound sites, protease activity can also result in structural damage. This damage can prolong inflammation and delay re-epithelialisation and wound healing [135], [139], [140]. Protease inhibitors such as α1-antitrypsin and secretory leukocyte protease inhibitor can limit such damage but, during inflammation, the balance favours proteolytic activity.

Also involved in the generation of collateral tissue damage are NETs. Neutrophils release a network of chromatin composed of DNA, histones and antimicrobial molecules including neutrophil elastase, myeloperoxidase and cathepsin G [141]. The primary purpose of NETs are to trap microbes, prevent bacterial dissemination and localise the neutrophil response [142]. Evidence suggests that NETs may provide means of prolonged exposure to self-antigens leading to prolongation of an immune response [143]. Current opinion holds that NETs are involved in a number of chronic inflammatory pathologies such as vasculitis, Systemic Lupus Erythematosus and IBD [140], [144].

Resolution

The purpose of resolution is to return inflamed tissue to baseline form and function. Immune resolution depends on the interplay between different mechanisms. This involves suppression of proinflammatory stimuli, arrest of cell recruitment, and reduction of effector site immune cells. The principle effectors of resolution are monocytes. During the second wave of monocyte migration, arriving monocytes can differentiate into alternative (M2) macrophages and function as immune suppressors. This represents a key step towards resolution as M2 cells function in multiple pro-resolution roles [131].

Phagocytic clearance of proinflammatory stimuli represents a critical step as elimination of proinflammatory stimuli favours a conclusion of inflammation [145]. Debris, in the

form of exogenous (e.g. microbial) and endogenous (i.e. self) material, represents a proinflammatory stimuli and removal is considered the primary driver towards resolution [146]. Furthermore, elimination of accumulated neutrophils represents another important step towards resolution. Spent neutrophils that have performed their antimicrobial function will undergo intrinsic programmed cell death (i.e. apoptosis). The process of apoptosis, as opposed to necrosis, sequesters proinflammatory debris from immune cell recognition. Efficient removal of antigen laden cells and fragments reduces the potential for inappropriate continuation of inflammation. This requires monocyte mediated clearance via specific phagocytic process. This non-inflammatory process is termed efferocytosis. What distinguishes efferocytosis from phagocytosis is its role in inducing monocyte switching to a proresolution phenotype [145]. Proresolution M2 monocytes secrete a host of anti-inflammatory mediators and as the M2 population increases, the anti-inflammatory gradient favours resolution over maintenance.

Suppressive M2 monocytes also secrete proresolving mediators (e.g. IL-10) which function to arrest further cell recruitment and stimulate reduction of accumulated immune cells [131]. Neutrophil apoptosis may also be initiated extrinsically by M2 monocytes with the release of Fas ligand (FasL) [131]. This acts in concert with neutrophil up-regulation of death receptors such as the membrane bound Fas Receptor (FasR). Binding of FasR with FasL results in inducing neutrophil apoptosis [147]. Further immune cell suppression occurs with down regulation of co-stimulatory molecules on M2 monocytes. Without costimulatory molecules, such as B7, interaction between monocyte MHCII and corresponding B or T-cell receptors is incomplete. This results in an anergic (i.e. nonresponsive) state and induction of apoptosis [146]. Finally, M2 monocytes also facilitate the induction of tissue repair by stimulating resident stromal cells with mediators, such as Transforming Growth Factor-β and Vascular Endothelial Growth Factor (TGF-β and VEGF respectively) [145], [148]. Activation of these cells (e.g. fibroblasts) initiates the repair process with the intention of returning affected tissue to normal conditions.

Failure to resolve acute inflammation in a timely manner has serious implications for continued neutrophil mediated tissue destruction and failure to resolve. The inability to resolve inflammation in a timely manner has been implicated in a number of chronic inflammatory diseases including Crohn’s Disease [140].

2.4. Histopathology of Crohn's Disease

CD is a lifelong inflammatory bowel condition involving the entire GI tract. It is marked by periods of disease quiescence and flare. During periods of relapse, an acute inflammatory response is superimposed on a chronic inflammatory state. Distinguishing the two inflammatory types has important implications for disease management [10], [149].

Macroscopically, CD manifests in a heterogeneous manner but has a number of stereotypical features (Figure 2.7). Early mucosal disease may present as normal tissue or manifest with multiple small (1 - 2 mm Ø) superficial ulcers. These ulcers may coalesce to form linear, or serpiginous, ulcers separated by oedematous tissue. This combination results in the classic 'cobblestone' appearance of an affected area. Commonly CD manifests in patchy, or discontinuous, lesions with defined borders. Affected areas may be separated by areas of mucosa of normal appearance, resulting in 'skip' lesions [150]. Other macroscopic features include luminal narrowing due to fibrosis (i.e. strictures), abscesses and fistulae. Fistulae are abnormal passages that may connect two body parts (e.g. small bowel to colon) or end blindly [151]. Also typical of CD is the phenomenon of 'fat wrapping', with mesenteric fat encircling an affected area [152].

Histologically, CD has a number of key features that are a result of the chronic and acute aspects of the disease (Figure 2.8). A distinguishing feature is the transmural nature of inflammation [153]. Inflammation associated with CD extends from mucosa to serosa, with immune cells present in all layers of the bowel wall [14]. Chronic features are the result of long standing disease involving immune cell organisation, tissue remodelling and architectural distortion [154].

A hallmark histologic sign of long-standing CD is the presence of non-caseating granulomas. Granulomas are defined as node-like aggregations of activated monocytes/macrophages surrounded by lymphocytes [111]. The non-caseating description indicates that they do not have a necrotic core, as is the case with tuberculosis granulomas. The patchy distribution of CD presents with focal lesions. These are characterised by increased LP cellularity consisting of aggregated lymphocytes. However, given the transmural nature of the disease, immune cells are not restricted superficially and can be found in deeper layers [14].

Active or ‘acute-on-chronic’ disease is characterised by recruitment and accumulation of innate immune cells (e.g. neutrophils and monocytes) superimposed on the chronic components (e.g. fibrosis) [155], [156]. Active CD is defined by a characteristic pattern of neutrophil accumulation which includes cryptitis and crypt abscesses [14], [152], [108]. Cryptitis is defined as neutrophil infiltration into the epithelium crypts. A crypt abscess is the presence of neutrophils in the lumen of affected crypts. Further diagnostic criteria includes neutrophil associated epithelial damage in the form of erosions or ulcerations. Neutrophils may also accumulate in the LP. The International Organisation of Inflammatory Bowel Disease defines the absence of neutrophils in the LP as indication of histologic remission [11], [108]. However, assessment of disease activity by LP infiltration lacks the reliability or reproducibility of cryptitis and crypt abscesses [14], [102].

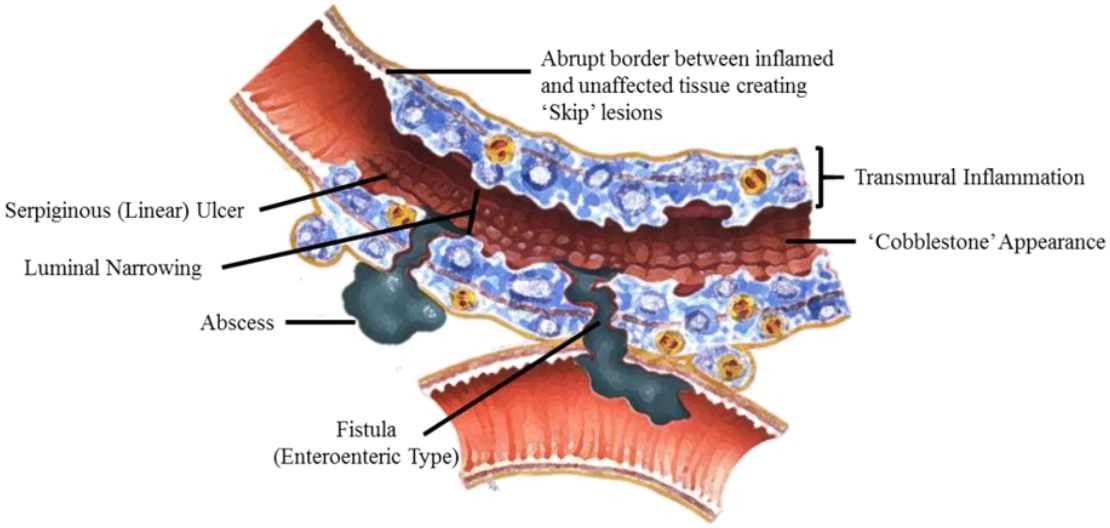

Figure 2.7. Typical macroscopic features associated with Crohn’s Disease. Mucosal changes include multiple serpiginous, or linear, ulcers, resulting in a cobblestone appearance. A common gross characteristic of CD is the patchy, or discontinuous, appearance of the disease. Affected areas may be separated abruptly by areas of mucosa of normal appearance, resulting in ‘skip’ lesions. Due to fibrotic deposition, the lumen will experience progressive narrowing. Deeper pathology includes transmural infiltration of immune cells. Transmural defects in the form of abscesses and fistulae are also seen. Not shown is fat ‘wrapping’ where the mesenteric fat will encircle an affected area. Adapted from Rubin Essential Pathology [157].

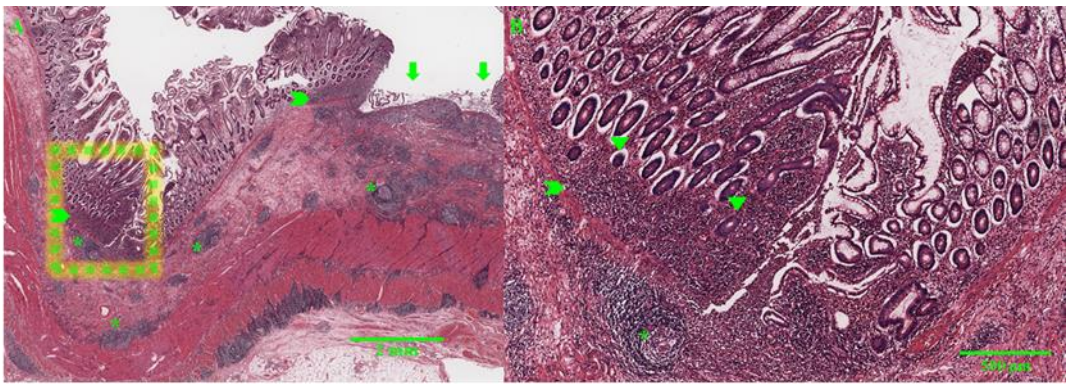

Figure 2.8A-B. Haematoxylin and Eosin (H&E) slide of the ileum from a 58 year old female diagnosed with CD. The left slide represents a low magnification view. The right slide is a higher magnification of the left slide (dashed green box). Histology demonstrates examples of 'acute on chronic' disease that result in a small bowel obstruction requiring surgical intervention. Notable features include transmural inflammation by mixed innate and adaptive immune cell types. The LP demonstrates focal areas of enhanced cellularity (chevrons). There is also considerable crypt irregularity including non-parallel crypts with variable diameters. There are multiple non-caseating granulomas (asterisks) i.e. collections of monocytes / macrophages surrounded by lymphocytes. They do not contain a necrotic core and are considered a hallmark feature of CD. Indications of active disease are the neutrophil associated mucosal erosion (arrows), cryptitis and crypt abscesses (arrow heads). Slide from Virtual Pathology at the University of Leeds [158].

Focal architectural changes that accompany chronic CD are important criteria for diagnosis [14], [159]. Ileal mucosal changes include villus distortion and crypt irregularity. Crypt irregularity is defined as non-parallel crypts, compromised or variable diameters (e.g. dilated crypts), with branches of decreased length [160].

2.5. Clinical Imaging

The diagnosis and monitoring of CD involves a number of modalities including clinical assessment, laboratory studies, pathology and imaging. Imaging involves the use of both external (i.e. radiology) and internal (i.e. endoscopy) means. Both approaches play an important role in establishing a diagnosis, measuring disease extent, detection of complications and determining disease activity. Furthermore, imaging disease activity assists in guiding management decisions and assessing response to medical therapy [5].

2.5.1. External Modalities

Current accepted means of non-invasive, external imaging of bowel inflammation include the use of standard X-ray, computed tomography (CT), magnetic resonance imaging

(MRI) and conventional ultrasound (US) [161]. Each modality has advantages and disadvantages (Table 2.3). There is a continued debate about which offers the most efficacious means of assessing disease. To date, no single modality has emerged as significantly superior to the other [162]. Regardless, it is clear that cross-sectional imaging of the bowel wall is the most effective means of disease assessment [163]. The primary advantage of cross-sectional imaging is evaluation of the transmural extent of inflammation [164]. Other advantages include improved imaging of associated complications (e.g. abscess and fistula) and detection of extraluminal signs (e.g. fat wrapping and lymph node involvement) [165]. Modalities capable of cross-sectional imaging of the bowel wall include CT, MRI and US and have largely replaced standard X-ray imaging [166].

In terms of overall CD assessment, which includes mural and extra luminal manifestations, contrast enhanced CT offers good sensitivity and specificity. This is particularly true for bowel obstruction (e.g. fibrotic stenosis) where sensitivity is in the range 81 - 94% and specificity is 96% [166]. However, sensitivity and specificity decline to 81% and 88%, respectively, when assessing low grade (e.g. early) disease activity [167]. This is due to the lack of sufficient spatial resolution of CT to detect early pathology at the mucosal level [163], [164], [166]. For example, early disease features (e.g. superficial ulcers) are not readily detected, limiting the use of CT in detecting low grade disease activity. Furthermore, the primary diagnostic criteria of inflammation is bowel wall thickening of greater than 3 mm [168]. Thickening is a nonspecific phenomenon and is associated with other bowel pathologies such as infection and neoplasms [169]. Furthermore, bowel thickening is not a feature of early active disease [163]. Other mural signs of inflammation fat halo sign which is generated by fat deposition in the submucosa, however, this sign may not be specific to IBD and maybe, in some instances, related obesity [170], [171].

Other limiting factors are related to bowel preparation, contrast enhancement and the nature of CT image generation. Pre-examination bowel preparation involves fasting and/or laxatives to achieve a clean bowel [164]. Furthermore, satisfactory bowel lumen patency is necessary to avoid collapsed bowel loops which can mimic pathologic signs (e.g. wall thickening) [164]. To improve luminal imaging capabilities, CT uses both oral and intravenous (IV) contrast. Oral contrast requires ingestion of large volumes (1 - 1.8 L) and can be poorly tolerated and uncomfortable due to bowel distension [172]. A further limitation of CT regards the use of ionising radiation giving a cumulative

Modality	Advantages	Disadvantages
Computed Tomography (CT)	• Cross sectional imaging (transmural disease evaluation, luminal narrowing) • Visualisation extraluminal disease (Mesenteric involvement including lymph nodes and fat wrapping)	• Ionising radiation • Bowel thickening primary sign (non-specific and not readily apparent in early disease) • Spatial resolution limits evaluation early active disease • Use of intravenous and high volume oral contrast (allergy and oral tolerance) • Collapsed bowel can mimic bowel wall thickening
Magnetic Resonance Imaging (MRI)	• Cross sectional imaging (transmural disease evaluation, luminal narrowing) • Visualisation extraluminal disease (Mesenteric involvement including lymph nodes and fat wrapping) • Good soft tissue contrast • Non-ionising radiation • Preferred examination by European Crohn´s and Colitis Organisation (ECCO) for repeated examinations	• Bowel thickening primary sign (non-specific and not readily apparent in early disease) • Use of intravenous and oral contrast (medical contraindications and oral tolerance) • Spatial resolution limits evaluation early active disease • Collapsed bowel can mimic bowel wall thickening
Ultrasound (Transabdominal Bowel Sonography (TABS))	• Cross sectional imaging (transmural disease evaluation, luminal narrowing) • Visualisation extraluminal disease (Mesenteric involvement including lymph nodes and fat wrapping) • High diagnostic accuracy for terminal ileal involvement • Non-ionising radiation • Recommended the use of TABS in the initial and emergent assessment	• Bowel thickening primary sign (non-specific and not readily apparent in early disease) • Reliance on nonspecific secondary signs of inflammation (loss of bowel wall stratification, ulcers and reduced motility) • Assessment of deep bowel structures limited (e.g. duodenum and rectum) • Low ultrasound frequency for tissue penetration reduces spatial resolution • Interoperator variability resulting in varied sensitivity and specificity

Table 2.3. Summary of the advantages and disadvantages of imaging CD by external means.

radiation dose and increased risk of cancer. This issue is particularly salient for paediatric patients where the long term nature of the disease and repeated examinations enhances a pre-existing risk of neoplastic disease [173]. It is for these reasons that the European Crohn´s and Colitis Organisation (ECCO) recommends CT for the diagnosis of acute complications only (e.g. fibrotic obstruction) [165], [174].

MRI is similarly capable of cross-sectional imaging in addition to assessing extramural disease. Furthermore, the reported sensitivity and specificity, 85% and 91%, respectively, are comparable to CT [167]. The excellent soft tissue contrast of MRI permits enhanced discrimination between pathology and healthy tissue [164], [166]. Assessment of CD activity is initially based on non-specific bowel thickening (>3 mm). Further evaluation is based on T2 imaging of bowel wall for signs of acute inflammation [175]. Detection can be improved with oral and IV contrast. Increased disease activity is thought to correlate with the presence of extravasated gadolinium (Gd) contrast into the bowel wall [163]. However, there is some indication that this relationship only offers a weak to moderate indication of disease activity [176]. Nevertheless, the limits of spatial resolution prevent reliable visualisation of early stage disease [164]. Also, MRI uses oral contrast in large volumes (≈ 1.5 L) to improve detection by distending the bowel lumen. As with CT, this is an important step in preventing misleading signs due to collapsed bowel [163]. The primary advantage of MRI over CT is the lack of ionising radiation.

The combination of satisfactory diagnostic capabilities and lack of ionising radiation has resulted in ECCO recommending MRI as the preferred imaging modality for repeated scanning [165], [174].

Transcutaneous abdominal sonography (TABS) is another means of assessing disease. Specificity and sensitivity for the detection of mural inflammation are 75% - 94% and 67% - 100% respectively [177]. The large range variation is attributed to both anatomic location of disease and inter-operator variability [166], [167]. It has been noted that diagnostic accuracy diminishes when imaging deep bowel anatomy (e.g. rectum and upper small bowel) [178]. Greatest accuracy is possible when the disease manifests in the terminal ileum [166]. Bowel thickening is again the primary criterion used for assessing bowel inflammation. Supporting evidence includes loss of bowel wall hyper/hypoechoic stratification, presence of ulcers and reduced bowel motility [163]. Increased mural vascularisation that accompanies acute inflammation. This maybe imaged with doppler US, semi-quantified and scored with the Limberg score. Tissue is graded (i.e. 0-4) based on thickening, wall stratification and flow [179], [180]. In order to permit sufficient tissue penetration for imaging the bowel, US is used in the frequency range 3.5 - 7.5 MHz [163], [181]. However these relatively low frequencies reduce spatial resolution and inhibit TABS assessment of low grade disease activity [163], [182]. Nevertheless, the wide availability of US, low cost and lack of ionising radiation has led ECCO to recommend the use of TABS in the initial and emergent assessment of CD [174].

2.5.2. Internal Modalities

Endoscopy represents a more invasive but direct means of evaluating disease activity (Table 2.4). The combination of direct mucosal visualisation, biopsy capabilities and delivery of therapeutics has made ileocolonoscopy the gold standard examination [183]. Other endoscopic methods include capsule endoscopy (CE), deep small bowel enteroscopy and upper endoscopy [165], [183], [184]. The most common mode of visualisation is white light imaging (WLI). The major disadvantage of this mode is the limitation to superficial mucosa assessment only [185]. Subsurface pathology cannot be evaluated without biopsy. Furthermore, reliance on superficial manifestations can be difficult where lesions are visually obscure (e.g. occult), variable in appearance, patchy in distribution and/ or occurring in microfoci [2]. Additionally, pathologic mucosal changes are often nonspecific due to visual overlaps with other GI diseases [27], [108],

[186]. Currently, the only means of diagnostic confirmation and deeper tissue analysis is endoscopic based biopsy [108], [174].

CE demonstrates high sensitivity in the detection of superficial mucosal lesions [187], [188]. Despite its lack of biopsy capabilities, CE does have advantages over conventional endoscopy in terms of small bowel imaging. Both ileocolonoscopy and upper endoscopy are physically limited to examining only a fraction of the small bowel. DSBE permits small bowel examination, with the added benefit of biopsy and/or treatment. However, full DSBE assessment requires both oral and rectal access. Unlike the minimally invasive nature of CE, DSBE is considered highly invasive, requiring lengthy procedure times, and is difficult to perform [189]. The ACG and ECCO recommends that DSBE be reserved for specific situations where biopsy or endoscopic intervention is required [5], [174].

Recommendations by ECCO and the ACG currently relegate CE to a second line or adjunct test after ileocolonoscopy and radiological exams [5], [166]. The principle reasons for second line status regards the lack of biopsy capability and inability to differentiate between bowel pathologies due to visual overlap. The limited specificity and lack of defined diagnostic criteria hinder full adoption of CE into current Crohn's management algorithms [5], [177].

Modality	Advantages	Disadvantages
Ileocolonoscopy	• Direct visualisation of the luminal surface • Biopsy and interventional capable • Frontline procedure for diagnosis and management	• Mucosal visualisation only (Visual overlap with other pathology) • Reliance on biopsy for deeper assessment • Limited to assessment of colon and terminal ileum • Invasive, requires skilled operator
Enteroscopy	• Direct visualisation of the luminal surface • Biopsy and interventional capable • Whole gastrointestinal tract assessment	• Mucosal visualisation only (Visual overlap with other pathology) • Whole tract assessment requires oral and rectal access • Highly invasive, requires skilled operator • Not recommended for routine assessment
Capsule Endoscopy	• Direct visualisation of the luminal surface • Whole gastrointestinal tract assessment • Minimally invasive	• Mucosal visualisation only (Visual overlap with other pathology) • Cannot biopsy • Adjunct test • Potential for capsule retention

Table 2.4. Advantages and disadvantages of Crohn's Disease assessment by endoscopy.

Despite the relatively high safety profile of CE, there is the potential for capsule retention [126]. Although a rare event, <2% of all patients, it is an important risk to consider when prescribing for CD patients. The fibrotic strictures associated with CD increase the risk of retention to exceed 8% [127]. A retained capsule represents a form of small bowel obstruction and can lead to perforation. Additionally, an ingested capsule is

contraindicated in MRI [128]. Therefore, it is recommended that CE be preceded by Patency capsule® administration [111]. The patency capsule is of similar dimensions to PillCam™ (11 x 26 mm) and consists of lactose and barium. The lactose dissolves in the GI tract while the barium is radiopaque on X-ray / CT. The capsule is also fitted with a 10 x 2 mm Radio-Frequency Identification (RFID) Tag for detection by non-ionising means [129]. The capsule is typically taken a few days prior to CE and an intact passage of the capsule is indicative of a patent bowel [130].

2.6. Summary and Conclusions

The human GI tract is responsible for the absorption of nutrients and elimination of waste. In order for it to carry out these functions, it is necessary for it to interact with the external environment. To facilitate its fundamental responsibility and maintain sterile internal conditions, the GI tract has a highly selective barrier at the environment interface. Selectivity is necessary for the ingress/egress of nutrients and waste. Barrier function is necessary to prevent contamination of the sterile internal environment of the human body. This is the dual responsibility of the single layer of mucosal epithelial cells lining the entire surface area of the GI tract. Augmenting the single cell layer selective barrier is luminal mucus which traps microbes but permits nutrient contact with the epithelium. The GI tract also houses a highly sophisticated and organised system that rapidly responds to noxious insults to prevent further damage. It carries a full complement of innate and adaptive immune elements responsible for responding to microbial encroachment.

A barrier breach of the GI immune system results in an acute inflammatory response. Acute inflammation initially involves cells of the innate arm, namely neutrophils and monocytes. The initial phase of acute inflammation is characterised by a rapid influx and accumulation of innate cells. This is designed to overwhelm and rapidly clear immunogenic stimuli. This initial response is referred to as nonspecific and does not retain lasting specific immunological memory. Adaptive immune cells follow the innate cells arm. It is capable of a highly specific antigen response and maintains immunologic memory. The endpoint of acute inflammation is removal of the noxious stimuli to return the affected region to baseline conditions. Failure to clear immunogenic stimuli results in repeated immune activation causing chronic inflammation, a pathologic condition in itself.

CD is an example of a lifelong chronic inflammatory condition. The disease is marked by features of both acute and chronic inflammation. Macroscopically, CD is patchy in nature with grossly affected areas separated by healthy appearing mucosa resulting in skip lesions affecting the entire length of the GI tract. Histological features include transmural inflammation, non-caseating granulomas and focal lesions of organised immune cells. Acute, or active, disease is defined by the presence of neutrophils in the LP and crypt spaces as either cryptitis or crypt abscesses.

Imaging of CD for diagnosis and management is by either external or internal means. External imaging includes CT, MRI and TABS. The advantages of these modalities include visualisation of the transmural (i.e. cross-sectional) aspect of the bowel and provision of information on extraluminal disease manifestations. Despite these advantages, no single modality is superior to another and none has sufficient resolution to sensitively detect low grade disease activity. Furthermore, assessment of active disease is hampered by their reliance on nonspecific aspects of inflammation (e.g. oedema). Nevertheless, non-ionising means of imaging (e.g. MRI and US) possess an advantage in regard to long term repeated scans.

Internal means for CD assessment relies on endoscopic techniques which include ileocolonoscopy, DSBE and CE. Endoscopy provides a means of directly evaluating the mucosa and has proven useful in assessing mucosal healing as a treatment endpoint. Nevertheless, reliance on superficial manifestations is limited due to visual overlap with other diseases and inability to assess subsurface pathology. These shortcomings can be overcome by tissue biopsy and histopathological analysis. Both ileocolonoscopy and DSBE allow for biopsy but are considered invasive procedures. CE offers a number of advantages over conventional endoscopy. It is non-invasive, suitable for repeated examinations and able to transit the entire GI tract. These points make CE, on paper, ideal for imaging CD. However, CE is severely disadvantaged by its reliance on mucosal manifestations of disease for assessment. This limits its role and full adoption in the diagnosis and management of CD by either ECCO or the ACG.

The inability to satisfactorily image and fully assess disease activity has created a clinical need for a more efficacious means of imaging CD. An ideal means should be non-invasive for repeated examinations. It should be capable of imaging the entire GI tract and cross-sectional imaging is paramount to provide deep tissue information. Image resolution must be sufficient to detect disease activity without relying on nonspecific signs of inflammation. Such an imaging modality represents a means of mitigating the

need for tissue biopsy and allows for *in situ* evaluation of subsurface pathology. Adapting high resolution μUS to CE represents a rational concept as it meets the aforementioned criteria.

USCE would provide clinicians a means of evaluating subsurface disease activity along the entire length of the GI tract. Suitable for repeated examinations, USCE would provide a way of monitoring disease activity during periods of treatment. Furthermore, USCE has the potential to advance the notion of histological remission by providing high resolution subsurface information on disease activity. Image guidance would better inform clinicians as to disease status and response to treatment and permit evidence based management decisions.

Chapter 3: Materials and Methods

3. Chapter Introduction

This chapter describes the materials and methods consistently employed throughout the duration of this project. Procedures related to experiments that deviated from normal practice will be addressed in specific sections.

The Sonopill programme was multidisciplinary project for which I acted as the Clinical Research Fellow, Technical Lead (re: diagnosis and therapy) as well a part-time PhD student. As the sole physician on a predominately engineering project I was involved in most aspects the programme. Salient duties included development, planning and execution of the *in vivo* pig experiments, advising on device design and assisting other Sonopill related matters. This meant there was often overlap between my thesis and that of other subprojects as there were common goals.

3.1. Materials

Bowel tissues from mice, pigs and humans were used for the purposes of *ex vivo* and *in vivo* experiments. All mouse and human tissue types were used in *ex vivo* situations and pigs were used in both conditions.

3.1.1. Human Tissue

Human GI tissue was obtained for *ex vivo* scanning from surgically removed bowel samples acquired from areas remote (> 20 cm) from the visually identified tumours by the Consultant Pathologist and was presumed healthy. Five subjects were enrolled (Table 3.1). This study was reviewed and approved by the NHS Tayside Tissue Bank Committee (Study Number TR000442). All patients were informed and consented by the Tissue Bank Nurse prior to surgery.

3.1.2. Pigs

Ex vivo pig experiments utilised abattoir obtained porcine tissue that included samples from the oesophagus, small bowel and colon. Fresh-frozen post-mortem samples were purchased from Medical Meat Supplies Ltd (Rochdale, UK). Tissue samples were

Case	Scan Date	Age	Sex	Diagnosis	Location	Procedure	Past Medical History	Medication
1	20170605	42	F	High Grade Dysplasia	Right Ascending Colon	Right Hemicolectomy	No Significant Issues	None
2	20170615	90	F	Adenocarcinoma	Right Ascending Colon	Right Hemicolectomy	Diabetes, Hypertension, Hypothyroidism, Osteoporosis, Osteoarthritis, Diverticulosis, Coronary Arterial Disease (Stented)	Ferrous Fumarate, Bisprolol, Irbesartan, Furosemide, Levothyroxine, Nicorandil, Isosorbide, Asparin, Zinc Supplement
3	20170917	78	M	Adenocarcinoma High Grade	Right Ascending Colon	Right Hemicolectomy	Ischaemic Heart Disease, Angina, Myocardial Infarct, Aortic Valve Disease (Replaced), Chronic Obstructive Pulmonary Disease, Atrial Fibrillation, Osteoarthritis, Gastroesophageal Reflux Disease, Diverticulosis, Non-Hodgkin's Lymphoma (Rituximab), 20 Cigarettes/Day	Clopidogrel, Rantidine, Ramipril, Alfuzosin, Simvastatin, Finasteride, Glyceryl trinitrate spray, Salarnol, Ultibro
4	20180410	80	F	Adenocarcinoma Moderately Differentiated	Right Ascending Colon	Right Hemicolectomy	Total Knee Replacement, Hypertension, Alcohol Dependency	Furosemide, Mirtazipine, Omeprazole, Thiamine, Zopicolone, Ferrous Fumarate, Folic Acid, Paracetamol, Ibuprofen, Vitamin B
5	20181003	62	F	Adenocarcinoma Moderately Differentiated	Caecum	Right Hemicolectomy	Hypertension, Diabetes Type 2, Asthma, Gastroesophageal Reflux Disease, Peripheral Neuropathy, Depression, Morbidity Obesity, Unknown Cigarettes/Day	Novomix, Dapagliflozin, Furosemide, Fexofenadine, Sertaline, Pregabalin, Tildiem, Ranitidine, Amitriptyline, Zopiclone, Metoclopramide, Laxido, Peptac, Cocodamol, Relvar Ellipta, Clenil, Salmeterol, Salamol

Table 3.1. Demographics and medical information of patients enrolled on the microultrasound characterisation of gastrointestinal tissue study.

individually vacuum packed, frozen and stored at -4°C. These samples were assumed to be healthy tissue as they were originally intended for human consumption.

In vivo porcine experiments used 20 female Landrace pigs, weight range 40 - 64 kg, and age range of 3 – 4 months. These were obtained from a local breeder/supplier as no special requirements were needed. Pigs were kept in licensed housing (UK Project Establishment License 60/4604) in groups of no less than two animals. The study was conducted under Home Office (UK) Procedure Project Licence (PPL): PF5151DAF held by Prof Eddie Clutton of the University of Edinburgh (The Royal (Dick) School of Veterinary Studies), in accordance with the Animal (Scientific Procedures) Act 1986. The project license was modified to include endoscopy experiments.

3.1.3. Mice

Wild-type C57BL/6 mice were used for all stages of the acute inflammation experiment with the exception of stage 2B. The use C57BL/6 mice was based on documented strain susceptibility to dextran sodium sulphate [190]. Two female heterozygous adenomatous polyposis coli ($Apc^{Min/+}$) mice were included in stage 2B. Ages were 67 - 88 days with a median of 74.3 days. Animals were grouped by sex in each experimental stage (Table 3.2). Mice were housed in the University of Dundee Wellcome Building Resource Unit (WBRU) and maintained in accordance with UK Home Office guidelines for the care and use of laboratory animals under the supervision of Dr Ngaire Dennison, the Named

Stage	Treatment Regimen	Number	Sex	Genotype	Age (Day 0)	Weight Range (Day 0)
1A	5% DSS Max. 7 Days	N=5 N=4 Treated N=1 Control	N=5 Male	N=5 WT C57BL/6	72-80 Days Old	24.2-25.2 g
1B	5% DSS Max. 7 Days	N=7 N=4 Treated N=3 Control	N=7 Female	N=7 WT C57BL/6	78-88 Days Old	19.6-21.6 g
2	5% DSS Max. 5 Days 2x mice culled daily	N=12 N=10 Treated N=2 Control	N=6 Female N=6 Male	N=12 WT C57BL/6	69 Days Old	18.4-24.3 g
3	5% DSS Max. 5 Days Randomised Control Trial	N=16 N=11 Treated N=5 Control	N=11 Female N=5 Male	N=16 WT C57BL/6	67-81 Days Old	18.1-24.8 g
2B	5% DSS Max. 5 Days 2x mice culled daily	N=7 N=6 Treated N=1 Control	N=3 Female N=4 Male	N=5 WT C57BL/6 N=2 $Apc^{Min/+}$	67-68 Days Old	18.4-26.3 g

Table 3.2. Mouse demographics for acute inflammatory studies; stages 1A, 1B, 2, 3 and 2B. DSS: Dextran Sodium Sulphate, WT: Wild Type, $Apc^{Min/+}$: adenomatous polyposis coli (heterozygous)

Veterinary Surgeon. The study was conducted under Home Office (UK) Procedure Project Licence: P3800598E held by Prof Inke Näthke of the University of Dundee in accordance with the Animal (Scientific Procedures) Act 1986.

3.1.4. Ultrasound Systems

Microultrasound (μUS) scanning was performed *ex vivo* and *in vivo* with single element high frequency transducers and associated equipment.

Single Element Transducers

Ex vivo scanning was accomplished with two types of single element μUS transducers (Table 3.3). One type of transducer used a piezocomposite element based on lead zirconate titanate (PZT), with samples manufactured by Applied Functional Materials Ltd (AFM, Birmingham, UK) focused to different depths. Frequencies ranged from 25 to 50 MHz. The second type of transducer was generously provided by Prof Kwok-Ho Lam (Hong Kong Polytechnic University, Hong Kong). This transducer was manufactured using lithium niobate (LNO) piezocrystal and operated at a frequency of 62 MHz. This transducer was used in mouse experiment 2B due to its higher frequency.

Scanning Systems

The single element transducers were used in conjunction with two bespoke scanning systems in two configurations design and built by Drs. C. Démoré, H. Lay and Mr R. Poltarjonoks. The Step Scanner obtained μUS data in a discontinuous transducer step-stop-scan manner (Figure 3.1A). The Continuous or ‘Fast’ Scanner maintained a

Transducer ID	Material	Centre Frequency (MHz)	Focal Distance (mm)
Th19	PZT	47.7	6.5
Th23	PZT	25.8	8
Th24	PZT	34	6.5
Th25	PZT	37.5	6.5
Th26	PZT	50	6.5
HK62	LNO	62	6.5

Table 3.3. Profiles for the various single element transducers used throughout this project. Transducers were manufactured by Applied Functional Materials Limited (AFM, UK) and Prof Kwok-Ho Lam (Hong Kong Polytechnic University). PZT: Lead Zirconate Titanate piezocomposite, LNO: Lithium Niobate

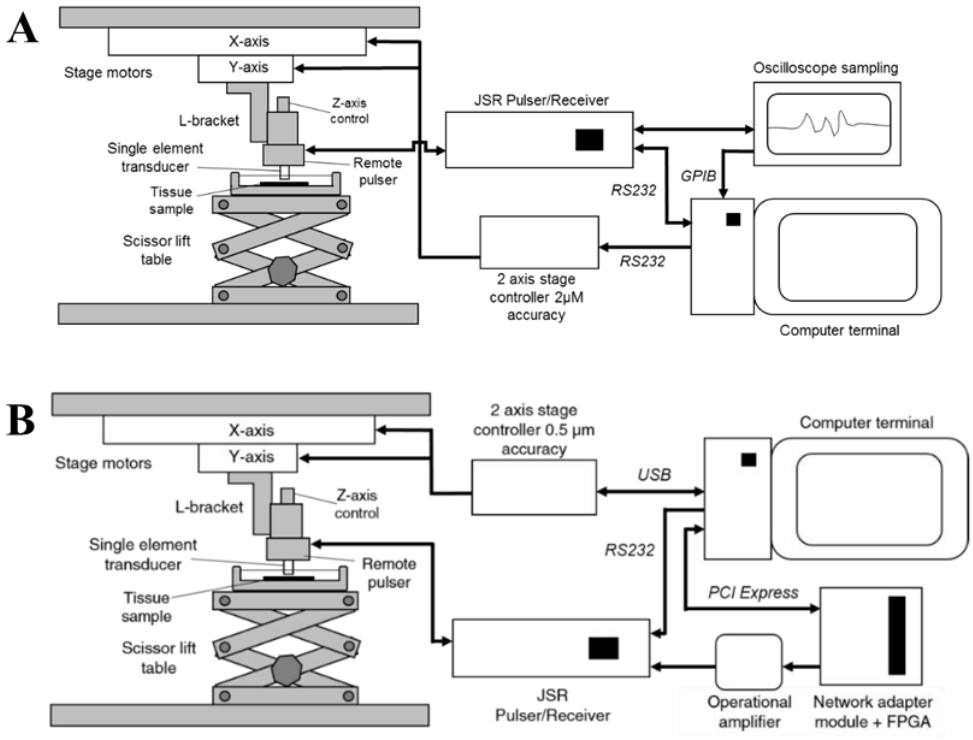

Figure 3.1A-B. Diagrams of the scanning systems used to collect microultrasound scan data from *ex vivo* tissue samples. Figure 3.1A depicts the Step Scanner. Figure 3.1B illustrates the Continuous Scanner. The former obtains data in a discontinuous manner: the stage motor moves the transducer a prescribed distance, stops to scan, and then steps to the next scan point. This method permits better motor accuracy and a high signal to noise ratio (SNR) but requires extended periods of time to acquire data due to the slow progression of the transducer. The Continuous Scanner, by comparison, acquires data at a much faster rate. It permits simultaneous travel and data acquisition without interruption. However, there is a concomitant decrease in SNR as result of decreased signal averaging. Technical differences between the two systems are addressed in Appendix A. Images adapted from Anbarasan *et al* [191].

consistent, programmable, speed, with data being collected during transducer movement (Figure 3.1B). Detailed technical differences between the μUS step and continuous scanning systems are outlined in Appendix A. The arrangement of the μUS step scanner system comprises a stepper motor (Sigma Koki Co., Ltd, JP), remote pulser-receiver (DPR 500, JSR Ultrasonics, Imaginant Inc., US) and external oscilloscope and computer to coordinate and support the μUS scanner. The frame of the scanning system consists of four aluminium pillars mounted between two optical breadboards (Thorlabs Ltd, UK) to provide stability during scanning. Within the frame, attached to the optical breadboard, are the mobile parts of the scanning system. Two-dimensional (X and Y) motion is achieved through the stage (stepper) motors. The remote pulser was mounted to these via an L-bracket, with a goniometer for accurate positioning. The stage motors were connected to an axis stage controller (Sigma Koki Co., JP). The mixed domain oscilloscope (Tektronix UK Ltd., UK) recorded the raw electrical echo signal from the μUS transducer which was transmitted to a LabVIEW program (National Instruments, Austin, US), custom coded to automate the scanning process.

Capsule Based Transducers and Cart

In vivo pilot studies of USCE required the development and manufacturing of simple prototype capsule devices. Termed ‘Sonocaps’, these tethered devices were designed to address a number of basic questions central to the future development of USCE.

Sonocaps measure 10 mm diameter x 30 mm length (Figure 3.2). They contain up to four single-element spherically focused μUS transducers made with polyvinylidene fluoride (PVDF, Precision Acoustics, Dorchester, UK) operating at 30 MHz, with a focal distance of 6 mm. The diameter of each PVDF transducers is 4 mm. Three transducers were placed on one side along the long axis of the Sonocap. The fourth transducer was situated opposite the front end of the capsule, with the tethered end representing the back end. The locations of the transducers were chosen to allow a comparison of image quality as a function of capsule position along the axis of the capsule.

All US capsules were manufactured, and safety tested ‘in-house’ by members of the Sonopill team which included Drs H. Lay, Y. Qiu and R. McPhillips of the University of Glasgow, School of Engineering, and Dr G. Cummins of Heriot-Watt University, School of Engineering and Physical Sciences. Safety tests included thermal heating, tether

strength, electrical hazards, hermeticity and material toxicity. Testing was done to ensure that capsules did not pose a hazard to animal or operator.

To facilitate experimental set-up and repeatability, the capsule control and data acquisition equipment was located on a mobile cart for use during *in vivo* testing (Figure 3.3). The capsule was attached to the JSR pulser (JSR Ultrasonics, Imaginant Inc., NY, US). Ultrasound signals were transmitted to each of the four capsule transducers via respective micro-coaxial cables (Alpha Wire, NJ, US). Received echoes returned via the same micro-coaxial cable for each transducer. The electrical power supply to the capsule also ran the length of the 3 m tether via two 0.1 mm diameter wires.

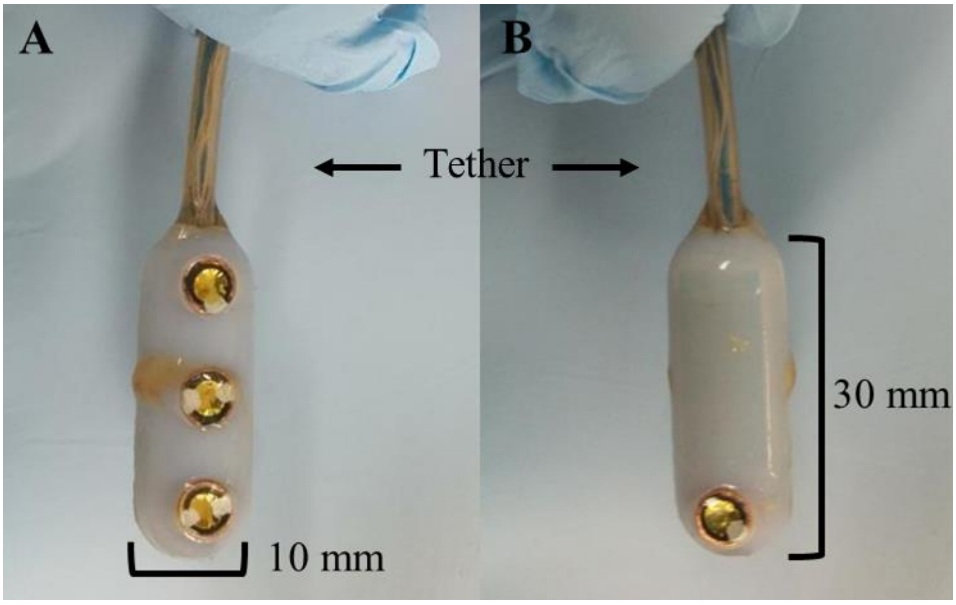

Figure 3.2A-B. (A) Sonocap microultrasound capsule with 3 of the 4 single element transducers. The fourth transducer is situated on the opposite side, distal from the tether (B). Each transducer is 4 mm in diameter and manufactured with PVDF (Precision Acoustics, Dorchester, UK). Transducers operate at 30 MHz, with a focal distance of 6 mm. Dimensions of the capsule are 30 mm in length x 10 mm in diameter. Afferent and efferent micro-coaxial cables contained in the 3 m tether were connected to supporting equipment.

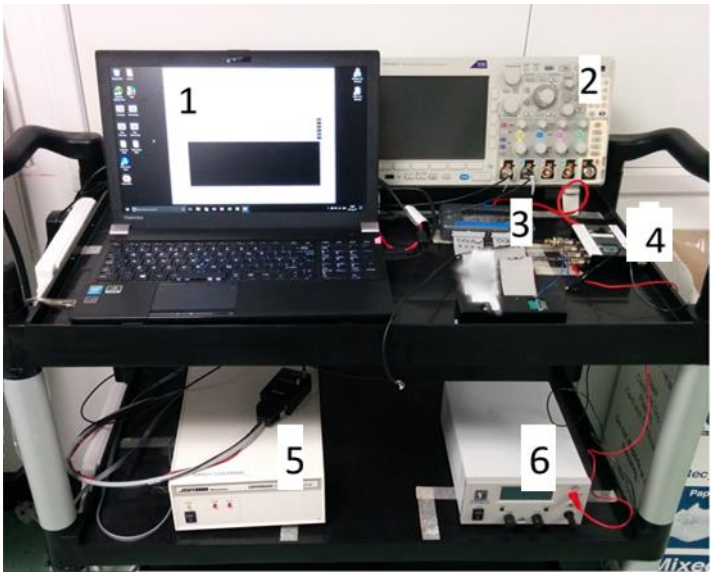

Figure 3.3. Support cart housing control and data acquisition hardware for Sonocap. Hardware includes a LabVIEW-based acquisition graphical user interface (GUI) (1), ultrasound data acquisition and monitoring oscilloscope (2), MyRIO (LabVIEW) real-time embedded evaluation board (3), Sonocap breakout box for capsule transducer connection to the control and data acquisition hardware (4), Ultrasonic pulser/receiver (5) and power supply (6). Image adapted from Lay *et al* [192].

System control was achieved with custom software coded in LabVIEW (National Instruments, Austin, US) paired with a myRIO-1900 acquisition device (National Instruments, Austin, US) and a commercial ultrasonic pulser/receiver (DPR500, JSR Ultrasonics, US), a power supply (EA-PS 2084-03 B, Elektro-Automatik, DE) and oscilloscope (MDO3024, Tektronix, US). The proximal end of the tether was attached to the myRIO device for real-time data acquisition and control.

Cart design and assembly was done by Dr H. Lay of the University of Glasgow, School of Engineering.

3.2. Methods

This section provides a description of the experimental procedures.

3.2.1. Inducing Inflammation

Inflammation was induced in individual mice with Dextran Sodium Sulphate (DSS). It is frequently employed in IBD studies due its simplicity of administration, cost and

reliability [190], [193]. It generally used to induce colitis in mouse models of IBD. However, researchers have noted that DSS can cause pan-gastroenteritis, causing inflammation from the stomach to colon [194]. Depending on concentration and frequency of exposure, DSS can be used to induce acute, chronic or relapsing models of intestinal inflammation [193]. A major deviation from human disease is the lack of T and B cell involvement in the development of DSS induced inflammation. Nonetheless, it considered applicable to the study of the genesis of intestinal inflammation [190]. First described in 1985 by Ohkusa, DSS has been used in multiple studies aimed at determining the pathobiology of IBD [195], [196]. The exact mechanism of how DSS induces inflammation is not completely understood but it is thought to interrupt GI barrier function, exposing immune cells to luminal antigens. This causes a rapid acute inflammatory response [197], [198]. Soluble in water, DSS is a negatively charged sulphated polysaccharide with a highly variable molecular weight in the range of 5 - 1400 KDa. Animals demonstrate variable responsiveness to DSS molecular weight. Factors involved in response include mouse strain, sex and gut commensals [190], [197], [199]. Nevertheless, 40 - 50 KDa has been described as the optimum molecular weight for inducing bowel inflammation [190], [197].

Signs of inflammation typically start by Day 3 of ingestion and are maximally manifested by Day 7. Clinical signs include weight loss, diarrhoea and GI bleeding which may be occult or overt in nature. However histological signs may be detected as early as one day after introduction of DSS [200]. To induce acute inflammation, 5% DSS (w/v) (MP Biochemicals, US) was dissolved in sterile water for oral intake *ad libitum* for stages 1 - 3 (Figure 3.4).

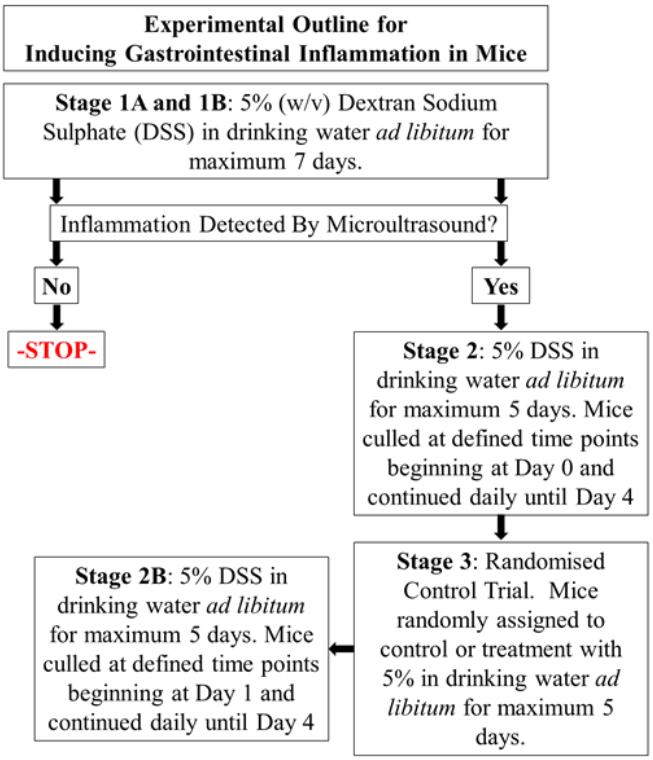

Figure 3.4. Experimental plan for inducing inflammation in the gastrointestinal (GI) tract of mice. Stage 1A and 1B were pilot studies with the intention to induce visual signs of inflammation to determine microultrasound (µUS) feasibility in detecting inflammation. Stage 2 (34 MHz) and 2B (62 MHz) examined the feasibility of µUS to detect the lowest inflammatory grade possible though daily culls and scanning of explanted bowel. Stage 3 was a randomised control trial where animals were assigned to control or treatment status by chance. Individual researchers assigned to interpreting data were blinded to status. This stage was designed to determine the lowest grade of inflammation detectable by µUS. This study was designated moderate on the severity scale in terms of animal discomfort by the University's Named Veterinary Surgeon (NVS). This figure was adapted from project licence number 70/8813 which was reviewed and approved by the UK Home Office.

3.2.2. Mouse: *Ex vivo*

Mouse: Acute Inflammation

Stage 1.

Stage 1 was a pilot study to determine the ability of µUS to detect overt (i.e. visually perceptible) inflammation. To achieve this, 2 groups of 4 mice segregated by sex were used. Stage 1A used an all-male group (N = 4) and stage 1B used an all-female group.

Mode	Expected Adverse Effect of the Technique	Health Assessment	Technique	Humane End-Point and Action To Be Taken
Dextran Sodium Sulphate 5% (w/v) in drinking water *ad libitum* .	Bowel Inflammation: Diaorrhea, Blood in Stool	0: Normal stools 1: Soft or very soft stools with positive blood on appropriate testing 2: Very soft stools with visual traces of blood 3: Watery stools with visible rectal bleeding	Visual inspection aided by using white paper to enhance presence of blood	Vetrinary Notification: Loose stools Cull: Blood is detected in the faeces (score 2 or 3 on scale above)
	Weight Loss	10% Weight Loss, 20% Weight Loss	Daily weights	Vetrinary Notification: Any animal that loses more than 10% bodyweight Cull: Loss greater than 20% of their body weight
	Dehydration	Daily Observations in conjunction with animal technicians	Observe for piloerection, skin tenting	Vetrinary Notification: Greater than than transient piloerection Cull: Demonstrates overt signs of dehydration (skin tenting)
	Pain	Daily Observations in conjunction with animal technicians	Abnormal behavioural assesment e.g. stool in bedding, obsessive behaviour, abnormal locomotion	Vetrinary Notification: Demonstrates evidence of abdominal discomfort/pain. Cull: Greater than transient abdominal discomfort/pain, hypothermia

Table 3.4. Study plan outlining the expected adverse events of inducing bowel inflammation with Dextran Sodium Sulphate (DSS) 5% (w/v) in drinking water *ad libitum*. The parameter and means of assessing animal status and resulting action if an adverse event was encountered are also presented. Stool grading scheme adapted from Chassaing *et al* [190].

Each group was sex matched to a DSS negative (DSS^{neg}) control. The two groups were to control for sex response differences reported in the literature [197]. Each stage began on Day 0 with introduction of 5% (w/v) DSS in drinking water with an intention of dosing for 7 days (Day 6) or until a humane endpoint had been reached. Humane endpoints were predefined in cooperation with the Named Veterinary Surgeon (NVS) along with the means of assessing tissue for scanning. All mice underwent daily observations which included health assessment, weigh-in and faecal examination (Table 3.4). Daily health assessments were done in close collaboration with the WBRU staff. Trained in recognising mouse distress, opinions expressed by a staff member were deemed authoritative and prospectively recorded.

Animals were culled by cervical dislocation and confirmation of death was by exsanguination by femoral incision. *Post-mortem* dissection of the bowel occurred after confirmation of death. Upon removal, the small bowel, caecum and colon were measured for length. This was followed by preparation of each anatomical section for scanning. This involved cleaning and transection along the bowel long axis allowing exposure of the mucosa to the transducer.

A preliminary inspection was done by dissecting microscope (Olympus SZ61, Olympus, JP) to ensure the mucosa was facing up and free of debris. If positive for debris, each section was further cleaned in an attempt to achieve total removal of food and faecal material to prevent misleading μUS signals. The tissue was also examined for overall status including naturally occurring variations such as Peyer's Patches. Finally, the sections were assessed for overt signs of inflammation which generally manifested as well circumscribed erythematous (i.e. blood red) lesions (Figure 3.5A-B).

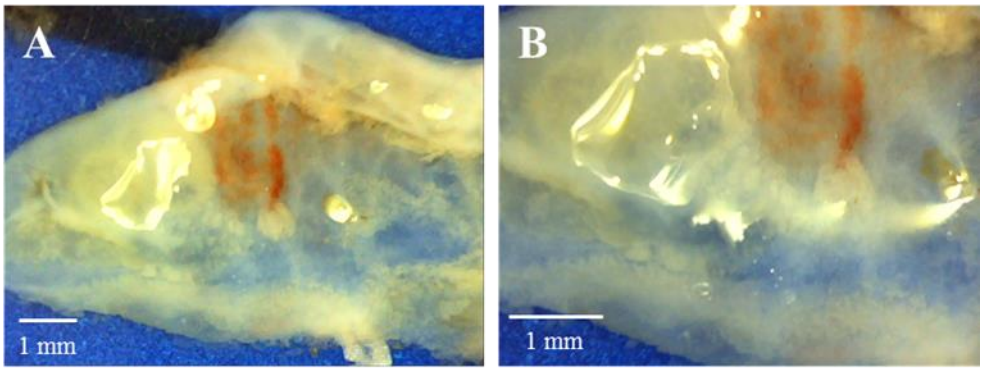

Figure 3.5A-B. (A) Example of an erythematous inflammatory lesion in the caecum after 5 days of 5% (w/v) Dextran Sodium Sulphate treatment. (B) Close up of the lesion demonstrating an overt central area of erythema bordered by subtler signs of inflammation.

Following initial assessment, the samples were transferred to the scanning tray (Figure 3.6). This consisted of a 12.5 cm x 8.5 cm x 2 cm (L x W x H, respectively) plastic dish containing an acoustic absorber (Aptflex F28, Precision Acoustics, UK) that doubled as a tissue pinning board. The tissue clamp was pinned to the absorber and the tray was filled with 1% (w/v) agar (Formedium, UK) to the level of the struts (i.e. 2 cm depth). The inner space of the clamp measured 30 mm x 15 mm. During the setting of the agar a removable 3.2 cm (L) x 1.5 cm (W) x 0.3 cm (H) Lego (LEGO®, DK) piece was used to create a trough between the struts This was done to prevent contact between the tissue and agar and provide a distinct µUS tissue signal. The recess was filled with acoustic coupling gel to avoid tissue sag during preparation. Tissue was secured using a Lego constructed tissue scaffold which was designed to secure the tissue and prevent excessive curling. Upon securing the tissue, the scan tray was placed in a slightly larger receptacle to contain a combined nutrient - µUS coupling fluid. Krebs-Henseleit Buffer (Sigma-Aldrich, US) titrated to pH 7.4 was used to maintain tissue viability and act as a µUS conducting medium for the duration of the scan.

Prior to scanning, the tissue was optically imaged using a Leica DM750 dissection microscope (Leica, Wetzlar, DE). Care was taken to assure optical images would align with µUS images. This was facilitated by the use of visual markers indicating the proximal tissue edge and right side of the Lego clamp (Figure 3.6).

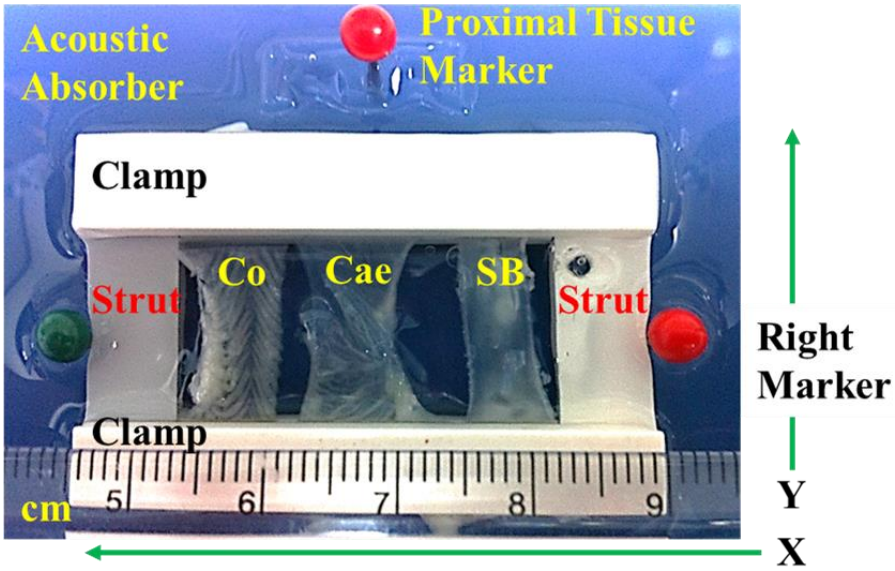

Figure 3.6. Lego mouse scanning tray for *ex vivo* bowel scanning. The clamp rested upon an acoustic absorber to diminish stray echoes and act as a pinning board. The scaffold and absorber were placed in a plastic container which was back-filled with 1% (w/v) agar to the top level of the struts. During the setting of the agar a separate 3.2 cm (L) x 1.5 cm (W) x 0.3 cm (H) Lego piece was used to create trough between the struts. This granted a 3 mm free space between the tissue and agar which was filled with acoustic gel. This kept the tissue free from contact with the agar and granted an independent acoustic signal from the two interfaces. Also shown in this image is the typical tissue arrangement for stage 2 scanning. The green arrows indicating the X and Y direction. Tissue was arranged from small bowel (SB), Caecum (Cae) and Colon (Co) from right to left. After the tissue was laid across the horizontal strut and secured in place using an overlying clamp. In addition to anchoring the tissue the clamps helped mitigate excessive tissue curl that occurred *post-mortem*. To ensure proper tissue orientation during optical imaging and microultrasound scanning, visual markers were used to indicate the right side and proximal tissue portion. The scanning tray was then placed in a second, slightly larger container and filled with nutrient-coupling fluid of choice, e.g. Krebs Henseleit solution. The tissue was submerged to appropriate scanning depth. Stage 3 scanning omitted use of the agar and replaced its lost volume with increased fluid. Co-Colon, Cae-Caecum, SB-Small Bowel

Tissue was scanned using a single element transducer and the Continuous Scanner described in Sections 3.1.5 and 3.1.6, respectively.

Scanning tissue samples involved common parameters outlined in Table 3.5. Transducer focal depth, as dictated by the transducers focus point, was set approximately to mid tissue depth to account for irregularities in tissue thickness and data acquisition included the agar signal. This resulted in an ultrasound travel time of 6.0 µs on the oscilloscope or a focal depth of approximately 4.62 mm. Gain was set to 40 dB and data averaged 32 times per scan point. Gain and data averaging were arrived at through an iterative process. The two-setting provided suitable imaging results within an acceptable time frame in regards

Stage	Section Scanned	X 'Slice' Distance (mm)	X Speed (mm/s)	Y Total Distance (mm)	Y Step Distance (mm/step)
1A	Lesion	9-40	0.1	0-7	0-0.3
1B	Lesion	9-31	0.1-0.2	0.1-0.5	0.5
2	SB_Cae_Co	32	0.2	18	0.2
3	SB_Cae_Co	32	0.2	18	0.2
2B	Co_Cae_SB	32	0.2	18	0.2

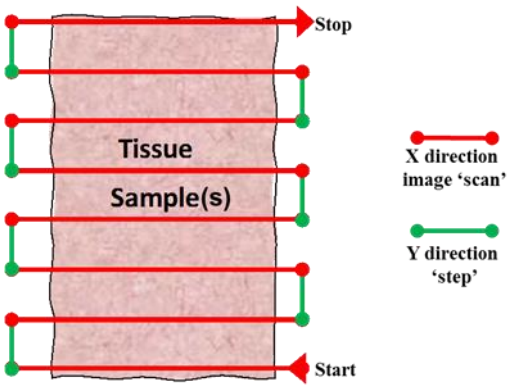

Scanning movement

Table 3.5. Scanning parameters for stages 1A, 1B, 2, 2B and 3 for the mouse inflammatory study. X direction variables (distance and speed) and Y direction variables (total distance and millimetre per step) varied until stage 2, 2B and 3 where dimensions were finalised to account for full tissue scanning, time per scan and maintaining tissue viability. The image below illustrates transducer movement in both X and Y directions. This resulted in a microultrasound image composed of several X cross-sectional 'slices' of variable length separated by a number of Y 'steps'. Abbreviations: Co-Colon, SB-Small Bowel, Cae-Caecum.

to tissue viability. For stages 1A and 1B, total distances in the X and Y directions were adjusted for lesion size.

	Grade			
Parameter	**0**	**1**	**2**	**3**
WBC Infiltration	Normal	Mucosa Only	Mucosa and Submucosa	Transmural
Mucosal Alteration	None, Intact epithelium	Focal: Loss of surface epithelium	Focal: Extends to Lamina Propria	Epithelial defect reaching beyond muscularis mucosae

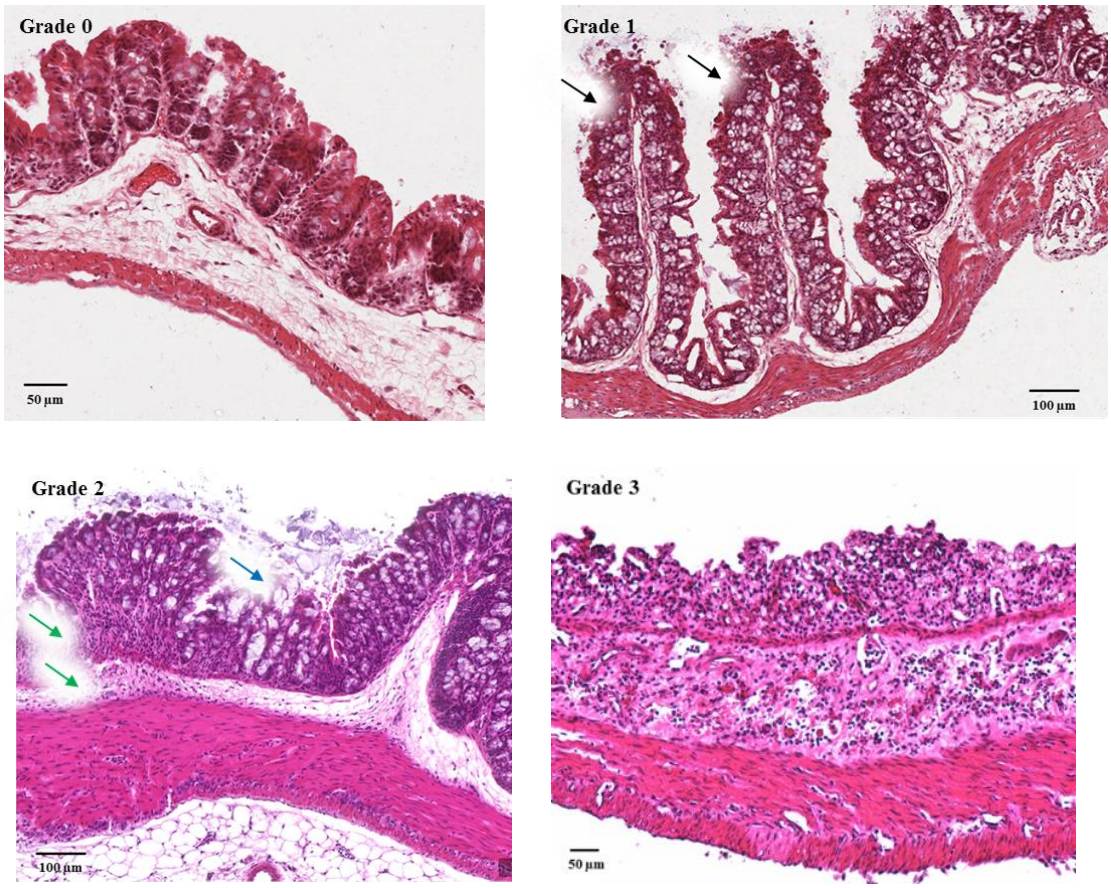

Table 3.6. Table and illustrative figures of the ordinal grading scheme to assess bowel inflammation. Haematoxylin and eosin stained tissue was assessed for histomorphologic alterations which include white cell infiltration and mucosal alterations. Grade 0 demonstrates no signs of inflammatory cell infiltration and continuous, intact epithelium. Grade 1 demonstrates signs of mucosal inflammatory cell infiltration (black arrows) without mucosal disruption. Grade 2 illustrates infiltration at the mucosa and submucosa (green arrows) and focal epithelial disruption (blue arrow). Grade 3 is an example of transmural inflammation with infiltration at all histologic levels and confluent disruption of the epithelium. Grading scheme was adapted from Erben *et al* and Elsheikh *et al*, [194], [201] respectively. WBC-White blood cells.

Following scanning, the tissue was fixed in 4% Paraformaldehyde (PFA) and cold stored (4^{o}C) in preparation for histological analysis. Tissue was stained with Haematoxylin and

Eosin (H&E) and slide mounted per established protocol (Appendix B). Microscopic analysis was accomplished with a Zeiss Axioskop (Zeiss, Wetzlar, DE). Tissue was assessed for changes in morphology, presence of inflammatory cells. Table 3.6 summarises the inflammatory grading scheme based on the aforementioned criteria as adapted from Erben *et al* and Elsheikh *et al* [194], [201], respectively.

Scan images were analysed qualitatively and compared to both optical images and histology slides. Scan reconstruction is described in Section 3.4.6. Scan images were first assessed for image quality, matched and aligned with their optical images. Scans were then examined for aberrant acoustic signals. Atypical images would include interruptions to normal tissue reconstructions as compared to DSS^{neg} controls. Images were also scrutinised and correlated with the optical appearance of the tissue. This included noting if an aberrant signal was due to the presence of debris. Images were also compared with histology to confirm the presence of inflammation and to correlate scan images with histological grading.

Stage 2

The aim of Stage 2 was to identify the lowest grade of inflammation detectable by µUS. Stage 2 involved 12 mice divided equally between male (N = 6) and female (N = 6) in sex separate cages. Mice were provided 5% DSS (w/v) in the drinking water *ad libitum* for a period of 5 days (Day 0 - Day 4). Days on DSS were adjusted as males and females from stage 1 reached a common humane endpoint on Day 4. Culling was by cervical dislocation and confirmation of death by femoral exsanguination. Prior to introduction of DSS on Day 0, one mouse from each sex was culled and served as a baseline DSS^{neg} control. Subsequently, mice were culled and scanned sequentially every 24 hours. Cull selection of 1 x Male and 1 x Female was done sequentially per unique identifier. However, this could be overridden if a humane endpoint was encountered. All mice underwent daily observations which included health assessment, weigh-in and faecal examination per Table 3.4.

The procedure for tissue scanning generally followed the details outlined in stage 1. Notable exceptions will be highlighted. Stage 2 inflammation often lacked visual evidence (e.g. erythematous lesions) for targeted scanning. Therefore, a comprehensive scan of the samples was required. This involved loading the tissue clamp with the distal ileum, caecum and proximal colon simultaneously as seen in Figure 3.5. Scan parameters were set to 32 mm x 18 mm in the X and Y directions, respectively. This overlapped with

the 30 mm x 15 mm window between struts to include a Lego signal on all 4 sides. This was done to include the Lego as a fiducial marker, ensure full tissue coverage and reduce scanner motor errors. The X direction speed was set to 0.2 mm/second and the Y direction step size was set to 0.2 mm/step. This was to ensure complete tissue coverage in a reasonable time frame and preserve tissue viability. Due to limited clamp capacity and lengthy scan time (> 4 hours per sample), morning and afternoon scanning were necessary. Morning and afternoon sessions alternated between sexes daily.

Post scanning, the tissue was processed as described previously. In order to analyse the tissue blindly, histology slides were randomised and coded by the Lab's Scientific Officer [202]. Slides were then batch scanned and digitised by the Tayside Tissue Bank on an Aperio Digital Pathology Slide Scanner (Aperio Scanscope XT, Leica, DE) at 40x. The slides were then examined with ImageScope software (Aperio ImageScope, Leica, Wetzlar, DE) and QuPath [203]. For each histology sample, an anatomic location was assigned, and inflammation was graded based on criteria from Table 3.6.

Stage 3

The aim of Stage 3 was to identify the lowest grade of inflammation detectable by µUS in a randomised control trial (RCT). Mice were randomly assigned to either a control or treatment group. The treatment group was further assigned to length of treatment randomly. This was done by the Lab's Scientific Officer using a list randomiser [204].

Stage 3 involved 16 mice in total (N = 16). Treated mice were provided with 5% DSS (w/v) in the drinking water *ad libitum*. All mice underwent daily observations which included health assessment, weigh-in and faecal examination per Table 3.4. Culling was by cervical dislocation and confirmation of death by femoral exsanguination.

The procedures for tissue scanning followed Stage 2 with two notable exceptions. Bowel prep was improved by gently brushing the tissue with a paint brush. This helped remove adherent debris from the tissue mucosa. Secondly, the scanning tray arrangement did not use agar and substituted the lost agar volume with additional Krebs-Henseleit Buffer. Complete scanning of the samples involved loading the tissue clamp with the distal ileum, caecum and proximal colon simultaneously similarly arranged as in Figure 3.6. Scan parameters were set to 32 mm x 18 mm. The X direction (32 mm) speed was set to 0.2 mm/second and the Y direction (18 mm) step size was set to 0.2 mm/step. Scanning sessions were in both the morning and afternoon.

Post scanning, the tissue was processed as described previously. One notable exception was to keep the tissue in the Lego scaffold for a period of 24 hours during fixation. This was to prevent tissue curl that occurred during the fixation process. In order to analyse the tissue blindly, the tissue was coded by the Lab's Scientific Officer [202]. Slides were then batch scanned and digitised by the TMA and Image Analysis Unit at the University of Glasgow on a Hamamatsu NanoZoomer NDP (Hamamatsu, JP) at 40x. The slides were then examined on QuPath. Each tissue scan was compared to the dissection microscope image simultaneously to rule out the presence of debris as a cause of aberrant signals. Scans were then examined for evidence of inflammation (i.e. aberrant signals) and results were correlated with histology to confirm the presence of inflammation.

Stage 2B

The aim of Stage 2B was to identify the lowest grade of inflammation detectable by µUS at 62 MHz. Stage 2B involved 7 mice (4 female, 3 male). Mice were provided 5% DSS (w/v) in the drinking water *ad libitum* for a period of 5 days (i.e. Day 0-Day 4). Culling was by cervical dislocation and confirmation of death by femoral exsanguination. Prior to introduction of DSS on Day 0, one female mouse was culled and served as a baseline DSS^{neg} control. Culls began on Day 2 after 48 hours of DSS exposure. All mice underwent daily observations which included health assessment, weigh-in and faecal examination per Table 3.4.

The procedure for tissue scanning generally followed the details outlined in Stage 3. Post scanning, the tissue was processed as described previously. Slides were then batch scanned and digitised by the TMA and Image Analysis Unit at the University of Glasgow on a Hamamatsu NanoZoomer NDP (Hamamatsu, JP) at 40x. The slides were then examined on QuPath.

3.2.3. Human *Ex vivo*

The aim of scanning *ex vivo* human tissue was to apply various µUS frequencies to determine their ability to resolve the histological layers of the GI tract. This pilot study was reviewed and approved by the Tayside Tissue Bank Committee and conducted in collaboration with NHS Tayside and Tayside Biorepository.

Surgical (i.e. bowel resection) cases were identified by the Biorepository Nurse, Sally Chalmers. Anatomical inclusion criteria included ileum, ileocaecal valve, ascending colon and intestine not otherwise specified. This was later amended to include transverse and descending colon in order to provide appropriate numbers to complete the project. Pathology criteria included inflammatory and neoplastic diseases. All patients were informed and consented prior to surgery by the Biorepository Nurse.

Immediately following surgical excision, tissue was delivered to the Consultant Pathologist for processing. This involved transecting the bowel and inspection by the Consultant Pathologist. After visually identifying the location of the tumour, an area of bowel, approximately 20 cm from the tumour, was chosen and sectioned out for µUS scanning. The sectioned-out samples were approximately 3 cm x 3 cm in size. As the samples were remote from the site of pathology, they were presumed healthy.

The tissue was then moved to a µUS scanning chamber comprising an acoustic absorber covered with 2% agar (w/w) (Fisher Scientific, UK) in a 135 x 85 x 55 mm^3 plastic tub containing a Lego Scaffold (LEGO®, Billund, DK) to raise the tissue off the agar (Figure 3.8). The agar between the scaffold platforms was covered with 1 - 2 mm of ultrasound coupling gel (Diagnostic Sonar Ltd, Livingston, UK) to ensure that the tissue was lifted off the agar to produce an isolated acoustic signal. The samples were pinned using 4 x 25G Microlances (Becton Dickinson, UK) and submerged in dPBS to a level allowing for sufficient µUS transducer immersion. Ultrasound focal depth was approximately at the level of the submucosa. The focus was set below the surface to account for variations in the height of the tissue and resulted in a transducer to tissue distance of approximately 4.0 mm.

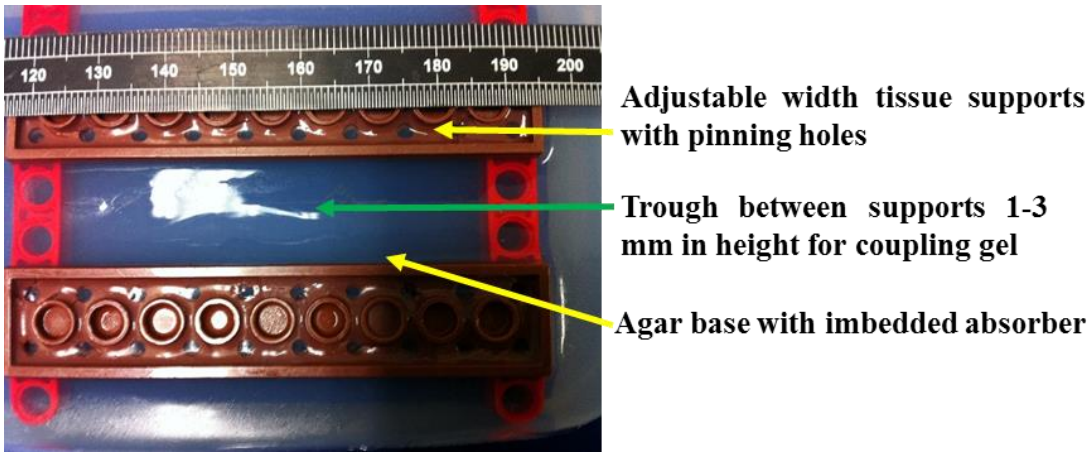

Figure 3.7. Lego scaffold used to support *ex vivo* tissue, both human and pig, during scanning. The tissue supports were adjustable in width and had 20 pin holes to accommodate tissue of varied sizes. The scaffold rested upon an acoustic absorber which served to diminish stray echoes and act as a pinning board. The scaffold and absorber were placed in a plastic container which was back-filled with 1% (w/v) agar to the bottom level of the tissue supports. This granted 1 - 3 mm free space between the tissue and agar which was filled with acoustic gel, keeping the tissue free from contact with the agar and granting independent acoustic tissue signals. Coupling fluid of choice, e.g. PBS, could then be used to submerge the tissue to an appropriate scanning depth.

Microultrasound scanning was performed using a selection of single element transducers operating at frequencies in the range 25 - 50 MHz (Table 3.3).

Analysis consisted primarily of reviewing the resultant µUS data and comparing results to human colon histology. Results were specifically analysed for discerning and display the cardinal histologic layers (i.e. mucosa, submucosa, muscularis propria and serosa).

3.2.4. Pig *In Vivo*

Pigs were used to test the feasibility of our prototype USCE to image the GI tract. Experiments were designed to address three fundamental concerns regarding the *in vivo* performance of USCE: whether intimate contact occurred between the US transducer and the gut mucosa, the quality of the acoustic signal (i.e. to discern cardinal bowel layers), and the optimal acoustic position of the transducer on the capsule (e.g. mid or end capsule).

All pig trials were conducted at Dryden Farm, a constituent of the Roslin Institute, University of Edinburgh, and attended by certified veterinary staff. Pigs were kept in licensed housing (UK Project Establishment License 60/4604) in groups of no less than two animals. Environmental variables were maintained within the limits detailed by the

Project Establishment License (PEL). This study was approved by the Animal Welfare and Ethical Review Board of the Roslin Institute, Roslin, Midlothian, EH25 9RG, and was carried out under Home Office (UK) License PPL PF5151DAF. All *in vivo* capsule manipulation was performed by individuals hold a Home Office issued Personal Licence (PIL). Obtaining a licence required attending the ScotPIL training course at the University of Edinburgh. Course work and training (animal familiarity/handling) was on both small animal (e.g. rodent) and large (e.g. pig and cow). A passing mark permitted application for a Home Office issued alpha-numeric licence. In addition, operators required competency assessment by the University of Edinburgh NVS. Capsule manipulation and endoscopy were performed by Dr R. McPhillips (PIL I9999073A) and the author, Dr B.F. Cox (PIL IA8090490).

Over the course of seven separate experiments, twelve Landrace pigs (*Sus scrofa domesticus*) were non-recovery anaesthetized and prepared for *in vivo* USCE testing. All pigs were female, approximately 6 months in age and weighed between 50-60 kg. Per Home Office directive, all animals were euthanized upon completion of the experiment.

Prior to unit arrival at Dryden Farm pigs were provided full rations and housed on straw. Upon arrival they were housed in a pen with rubber matting replacing the straw. The removal of straw was necessary as the consumption of high fibre straw and associated debris (e.g. pebbles) proved difficult to flush out of the small bowel. This interfered with conventional endoscopic and USCE imaging. Cleanliness of pigs on the rubber matting was initially poor, but much improved by increasing the floor space available and raising the rubber matted area so the pigs could designate separate latrine and sleeping areas more effectively. Heat lamps and environmental enrichment items (e.g. chew toys) were provided for warmth and to maintain healthy behaviour, respectively [205].

Originally, pigs were provided full rations and housed in straw bedded pens. However, it was apparent that pig consumption of the high fibre straw and associated material (e.g. pebbles) compromised bowel cleanliness. Furthermore, the indigestible fibre proved difficult to flush from the lumen. This may have led to bowel injury through over manipulation as evidenced by post-mortem examination. Therefore, a modified diet was necessary to improve bowel preparation. This entailed providing a low residue (i.e. low fibre) based nutritional supplement. Glutalyte® (Norbrook®, Newry, UK) is a commercially available product consisting principally of electrolytes and carbohydrates. It is intended for calves during periods of digestive disturbance. It was prepared according to manufacturer's recommendations of one sachet dissolved in 2 L of warm water.

Glutalyte was introduced in small volumes of 2 L between two pigs every 12 hours. This was done upon arrival at Dryden Farm to acclimate the pigs to the supplement. Generally, the supplement was found to be palatable by the pigs. Commercial pig feed (Rearer Pellets, ABN, UK) was provided until 36 hours prior to induction of anaesthesia. The pigs were then offered Glutalyte *ad libitum* equating to 2 L per pig every 12 hours until they were anaesthetised. Water was always available at 2 L per pigs every 12 hours *ad libitum*. During this period, baseline body weight was maintained, and blood glucose was found to be within normal limits.

Pigs were arranged in either a lateral (e.g. right side) or supine (i.e. on their back) position on the surgical table (Figure 3.9A). Position depended on abdominal stoma placement (Figure 3.9C and 3.9D). For oesophageal access, pigs were placed in a supine position. To preserve body temperature but maintain stoma access, the pigs were provided with a Bair Hugger warming blanket (3M™, US). The trachea was intubated, and anaesthesia was induced with isoflurane (IsoFlo, Zoetis, UK) vaporized in oxygen and nitrous oxide administered via a breathing system and facemask. Anaesthesia was maintained with isoflurane. Ringer's lactate solution (Aqupharm No 11, Animalcare, UK) was administered at 10 ml kg^{-1} hr^{-1} throughout each study to maintain fluid and electrolyte levels. The anesthetized pigs' lungs were mechanically ventilated to maintain normocapnia (i.e. normal blood CO_2 levels). Vital signs were monitored throughout the experiment by a licenced veterinary anaesthetist. When the experiments were complete, the animals were euthanized using pentobarbital.

Oesophageal Experiments

For the oesophageal experiments, a modified wide-diameter endotracheal (ET) tube was placed directly in the oesophagus. This was done to bypass the obstacle created by the anaesthetic tubing (Figure 3.9B). To assist with transducer-tissue coupling, a saline drip (≈ 1 - 2 drips/s) was used. The capsule was inserted orally, down the length of the ET tube into the proximal oesophagus. Capsule imaging of the oesophagus consisted of both static and dynamic scans. Static imaging was done in 3x positions which included proximal, middle and distal (i.e. gastroesophageal junction (GOJ)). Dynamic scans involved placing the capsule at the GOJ and slowly drawing it towards the mouth at rate of approximately 1 cm/s.

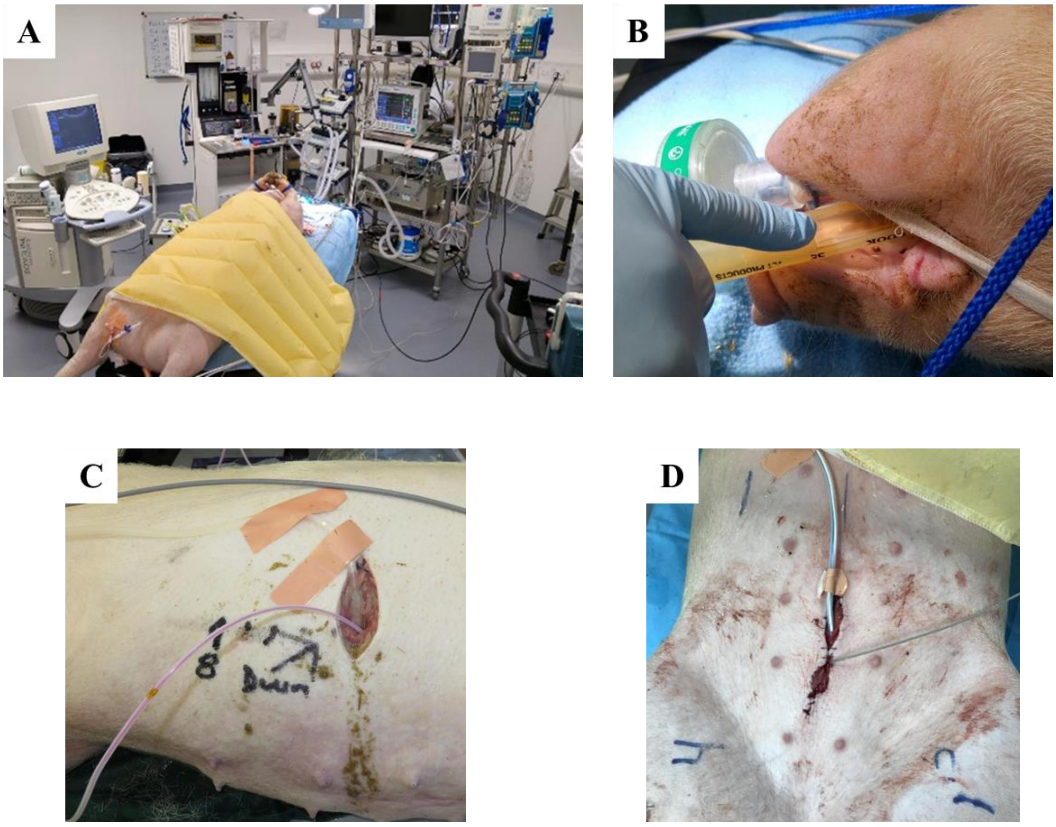

Figure 3.8A-D. Operating room set-up for pig trials. (A) Equipment setup including anaesthetic and monitoring devices (upper right), standard ultrasound machine (centre left) and experimental trolley (lower right). Test subject with warming blanket (centre). (B) Modified endotracheal tube (ET) allowing direct access to the oesophagus. (C) An artificial enterocutaneous small bowel stoma located on the lateral side of the abdomen with inserted capsule (tether visible). Also visible is saline drip used to assist with ultrasound coupling and prevent wound dehydration. (D) A midline small bowel stoma with a capsule and thermometer inserted distally and proximally, respectively (tethers visible).

Small Bowel Experiments

For small bowel experiments, direct access to the small bowel was gained through the surgical creation of an enterocutaneous stoma, bypassing the upper GI tract (oesophagus, stomach and duodenum). This avoided the challenges of having to navigate the capsule into the small bowel. Furthermore, it mitigated the need for longer capsule tethers. Stoma creation began with a 10 cm incision in the lateral side or midline of the abdomen by a qualified veterinary surgeon. The jejunum was identified and a 10 cm incision along the long axis of the bowel was created, allowing access to the lumen. The bowel was then suture secured to the subcutaneous layer of the dermis (Figure 3.9C). The long axis bowel incision opened the lumen to both antegrade (i.e. stoma to distal bowel) and retrograde (i.e. stoma to proximal bowel) capsule manipulation (Figure 3.9D). Following stoma

creation, the bowel was inspected for the presence of food residue. The bowel was then flushed with 37°C normal saline solution (0.9% NaCl g/L) if necessary.

Capsule examination of the small bowel involved both static and dynamic modes of imaging. In each case, an attempt was made to insert the capsule in the antegrade (i.e. proximal to distal) direction; however, the lack of reliable external guidance meant that this could not be guaranteed. Static imaging consisted of inserting the capsule in a proscribed distance (≈ 60 cm) and stationary transmural µUS data was collected for all four transducers. The process was repeated with capsule movement ≈10 cm retrograde until the capsule exited the stoma. Although static in terms of operator manipulation, movement due to peristalsis could not be ruled out. Dynamic scans involved inserting the capsule ≈ 60 cm and pulling the capsule back in 12 cm increments over a 30 second duration while µUS signals were recorded. As with the oesophageal studies, a saline drip (≈ 1 - 2 drips/s) was used to assist with µUS coupling and prevent dehydration of the stoma exposed bowel [206][207].

Scan analysis focused on addressing the three fundamental concerns regarding *in vivo* performance of USCE. Images were analysed for adequate transducer-mucosal coupling, image quality, identifying bowel tissue and cardinal layers. Results from *in vivo* experiments were also compared to *ex vivo* capsule results which provided isolated tissue images of pig bowel [208]. Optimal placement of the transducer on the capsule was also reviewed.

3.2.5. Microultrasound Image Reconstruction

Brightness (B) scan images were reconstructed from *in vivo* and *ex vivo* A-scan µUS data. This was achieved using a bespoke MATLAB (Mathworks, Natick, US) script designed to work in conjunction with the single-element scanning systems to streamline data acquisition, simplify data reconstruction and allow custom B-scan image presentation. Two-dimensional B-scans were created using averaged radiofrequency (RF) echo data with relative echo strength and colour mapped.

MATLAB programming was done by Drs S. Sharma, V. Bentivegna, H. Lay, C. Lemke and A. Chandra.

Chapter 4. Human Tissue Experiments

4. Chapter Introduction

This chapter describes microultrasound (µUS) scanning of surgically explanted human colonic tissue. The purpose of this pilot study was twofold. One aim was to tentatively identify a suitable frequency for inclusion into USCE. The other aim was to examine the relationship between acoustic tissue layers and histological layers as illustrated in chapter 1, figure 1.6A-C (p. 13). To achieve both of these aims, freshly acquired human colonic tissue was scanned at various µUS frequencies in three different orientations with respect to the µUS transducer (Figure 4.1). Scanning tissue in various orientations with high frequency µUS transducers has the potential to further elucidate the relationship between histology and the acoustic layers. This maybe particularly true at 90° as signals are generated exclusively from layer components. As introduced in Chapter 1, there is a debate as to the origin of the ultrasonic layers and whether they directly equate with histologic layers. Kimmey *et al* hypothesised that echoes arose from both layer interfaces and the components of each layer [56].

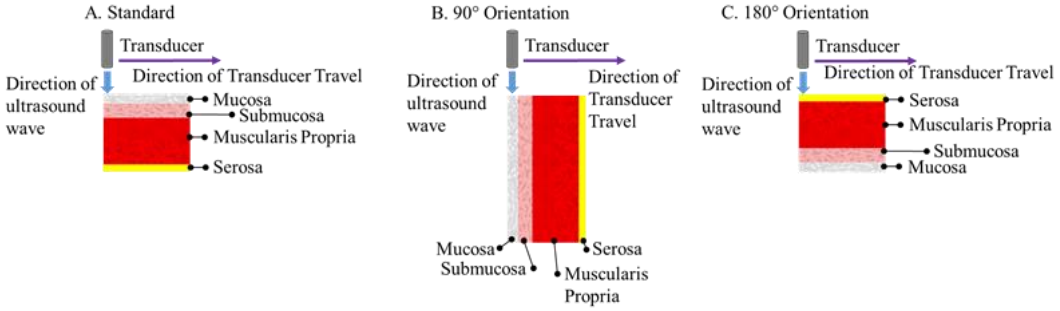

Figure 4.1A-C. Illustration of tissue orientation in relation to the transducers. (A) Standard scan where the mucosa faced the transducer. This orientation provided a mucosa to serosa cross-sectional image. (B) The tissue was rotated 90° so that each individual tissue layer faced the transducer. (C) The tissue was rotated 180° so that the serosa faced the transducer. This orientation provided a reversed cross-sectional image.

4.1. Optical Tissue Examination

Tissue from each patient or ‘case’ was brought directly from the surgical theatre to Pathology for inspection and processing. The tissue was examined at both the macroscopic (gross) and microscopic (histologic) levels. This was done to enable a comparison between the scan results and more conventional methods of tissue examination and to assist with interpreting ultrasound (US) results.

4.1.1. Macroscopic Examination

A total of five cases were included in this study and tissue was collected exclusively from the colon. Neoplastic disease was the reason for all five procedures. The site of the tumour was identified by the consultant pathologist (Figure 4.2). A 3x3 cm healthy section roughly 20 cm from the tumour was removed for scanning. Samples were inspected and photographed prior to US scanning (Figure 4.3).

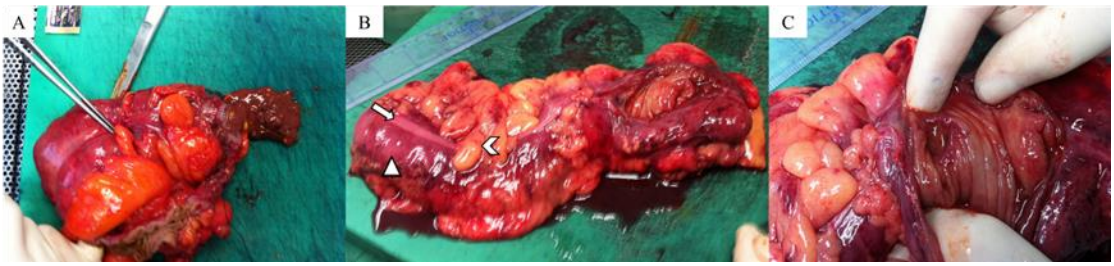

Figure 4.2A-C. (A) Ascending colon from Case 2. The pathologist has indicated the location of the tumour with forceps from the serosal side. (B) Ascending colon from Case 3. The subserosal taenia coli (arrow), a ribbon of smooth muscle that runs the length of the colon, can be seen. Haustra or sacculations were visible (arrowhead), which are created by contraction of the taenia coli. Both Cases 2 and 3 were imbued with numerous fatty appendages termed epiploic appendices (chevron). (C) In this image, the pathologist has shown the ileocaecal valve from the mucosal side of the caecum.

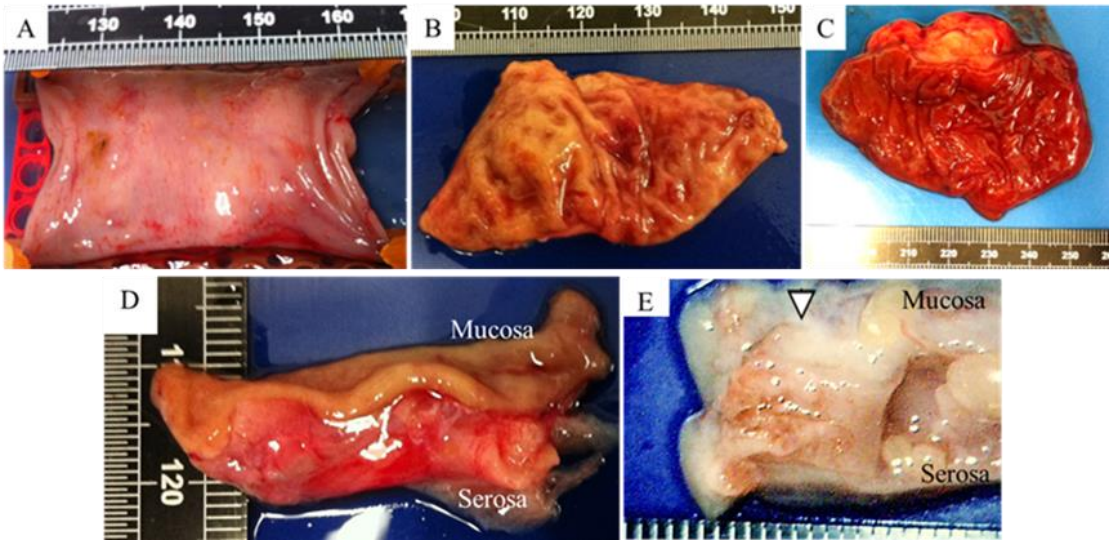

Figure 4.3A-E. Colon sections from Cases 1-4. Sections were taken from an area approximately 20 cm from the tumour. At this distance, the tissue was presumed healthy. (A) Case 1 image of the mucosa in the tissue scaffold. The mucosa appeared smooth, without visible defects. (B) Case 2 had multiple mucosal surface irregularities which included pitting and folds. (C) Case 3 also showed multiple surface irregularities in the form of mucosal folding. (D) Case 2 transmural image from the mucosa to serosa. The tissue appeared well organised without obvious defects. (E) Case 4 transmural image. Although a large defect is noted on the right of the sample, the scanned area (arrowhead) did not appear grossly deformed.

4.1.2. Histologic Examination

Histologic examination of the tissue was performed on Cases 1, 2 and 4 (Figure 4.4). Slides were produced by the Pathology Department and originated from locations in close proximity to the tumour but were from outside the tumour margins and considered disease free. As the slides were not from the scanned tissue, histology was used only as a rough indicator of the colon architecture and morphology.

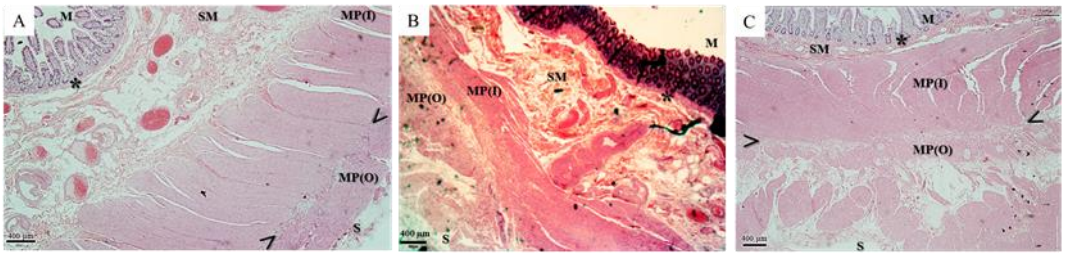

Figure 4.4A-C. Haematoxylin and eosin histology slides from Cases 1, 2 and 4. Tissue for histology originated from locations in close proximity to the tumour and was, therefore, distant from the ultrasound (US) scanned area. Nevertheless, the figure slides were from outside the tumour margin, considered disease free and were used only to approximate colon status. (A) Case 1 appeared morphologically normal and architecturally well organised compared to text references [70]. (B) Case 2 appeared architecturally normal, however, the submucosa appeared thickened and the muscularis propria thinned. (C) Case 4 appeared architecturally normal, however, the submucosa appeared thinned and the division between the inner and outer muscularis propria muscles was pronounced. M (mucosa), *(muscularis mucosa), SM (submucosa), MP(I) (inner muscularis propria), < > (division between muscle layers), MP(O) (outer muscularis propria), S (serosa).

4.2. Microultrasound Results

Microultrasound results were grouped according to tissue orientation. Cases 1-3 were scanned with the mucosa facing the transducer providing a mucosa to serosa cross-sectional image. Case 4 tissue was rotated 90° so each histological layer was individually scanned. For Case 5, the tissue was rotated 180° so the transducer faced the serosa which provided a serosa to mucosa cross-sectional image. All images are presented in 'Jet' colour format which showed hyperechoic, hypoechoic and anechoic signals as red-orange, yellow-light blue and dark blue, respectively. Results are summarised in Table 4.1.

Case	Orientation	25 MHz	34 MHz	37 MHz	50 MHz
1	Mucosa Up	Full Transmural Imaging, 5 Distinct Layers Detected	Full Transmural Imaging, 7 Distinct Layers Detected		Only partial tissue penetration, 7 Distinct Layers Detected
2	Mucosa Up	Full Transmural Imaging, 3 Distinct Layers Detected	Full Transmural Imaging, 4 Distinct Layers Detected		
3	Mucosa Up	Full Transmural Imaging, 0 Distinct Layers Detected		Full Transmural Imaging, 0 Distinct Layers Detected	
4	90°	5 Distinct Layers Detected		7 Distinct Layers Detected	
5	180°			Full Transmural Imaging, 5 Distinct Layers Detected	

Table 4.1. Summary of human tissue scan results at various microultrasound (µUS) frequencies. Greyed out blocks indicate that scan was not done at that particular frequency. This was often due to lack of transducer availability, transducer failure or time constraints.

4.2.1. Cases 1-3

Case 1

Tissue from Case 1 was scanned at 25, 34 and 50 MHz (Figure 4.5A-C). Case 1 at 25 MHz showed five distinct µUS layers between the surface (i.e. mucosa) and the serosa. The superficial mucosal layer was hyperechoic, which was followed by a deeper hypoechoic layer. The signal became uniformly hyperechoic and formed the third layer. The signal then changed and formed a predominately anechoic layer with hypoechoic elements. The final layer was a mixed hyper/echoic layer which corresponded to the serosa and mesenteric fat. The same tissue at 34 MHz revealed seven distinct ultrasonic layers from the mucosa to serosa. The first layer was a thin hypoechoic band and was followed by a thin anechoic stripe. The third layer was mixed hyper/hypoechoic. The fourth layer was a mixed hypo/anechoic layer. The final layer was hypoechoic, containing scattered hyperechoic elements. Tissue at 50 MHz showed seven distinct layers. The first and second layers were thin hypoechoic and anechoic stripes, respectively. The third layer was mixed hyper/hypoechoic and the fourth layer was anechoic with hypoechoic elements. The next layer was predominately hyperechoic with hypoechoic regions and was followed by a sixth uniformly anechoic layer. The final layer was a mixture of all three signal types. The decreased acoustic layers from nine at 34 MHz indicated signal attenuation. This was illustrated by the increased contribution of anechoic signals at deep layers compared to at 25 and 34 MHz.

Case 2

Tissue from Case 2 was scanned at 25 and 34 MHz (Figure 4.6A-B). The 25 MHz scan revealed three layers from mucosa to serosa. The first layer was hyperechoic and the second was hypoechoic. The final layer was predominately hyperechoic with hypoechoic elements. The same tissue at 34 MHz showed four layers from mucosa to serosa. The first layer was a hyper/hypoechoic layer. The second layer was predominately anechoic with scattered hypoechoic regions. The third layer was mixed hyper/hypoechoic and transitioned into a hypoechoic fourth and final layer.

Case 3

Tissue from Case 3 was scanned at 25 and 37 MHz (Figure 4.7A-B). Images from both frequencies failed to depict any distinct tissue layers. The only notable difference between 25 MHz and 37 MHz is the increased signal intensity at the tissue surface at 37 MHz.

4.2.2. Case 4

The tissue for Case 4 was orientated so that all layers faced the transducer and could be scanned individually (Figure 4.8A-B). In this arrangement, each histologic layer generated its own acoustic signal which was generated by the tissue composition alone. The tissue was scanned at 25 and 37 MHz. The scan began at the mucosa (X=0 mm) and terminated at the serosa (X=15 mm).

At 25 MHz, five distinct layers were detected. The first layer was predominately hyperechoic with scattered hypoechoic regions. The second layer was hypoechoic and became hyperechoic to form the third layer. The fourth layer was hypoechoic and transitioned to a mixed hyper/hypoechoic final fifth layer.

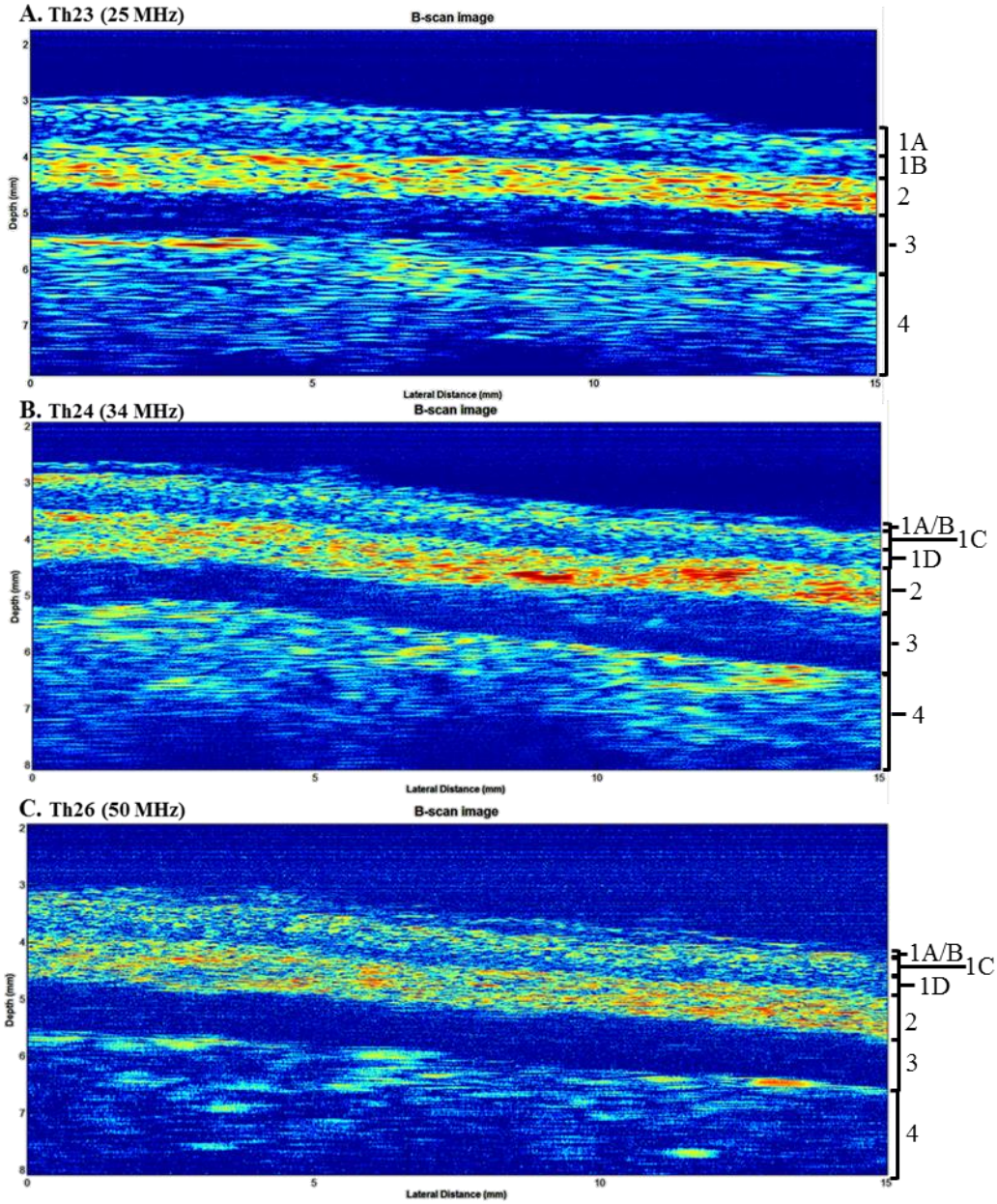

Figure 6.5A-C. Results from Case 1 scanned at 25, 34 and 50 MHz (A, B, and C, respectively). Ultrasonic layers were depicted as hyperechoic (e.g. red-orange), hypoechoic (yellow-light blue) and anechoic (e.g. dark blue). Results demonstrated both enhanced resolution as well as decreased tissue penetration with increasing frequency. At the superficial level, 25 MHz showed 2 distinct layers (1A and 1B) whilst 34 and 50 MHz showed 4 distinct layers (1A-1D). All 3 frequencies portrayed a hyperechoic second layer and a predominately anechoic third layer. Scans at 25 and 34 MHz included a mixed anechoic/hypoechoic third layer (3). Layer 3 at 50 MHz scan was predominately anechoic. Signal is also diminished from the fourth layer with 50 MHz as compared to 25 and 34 MHz

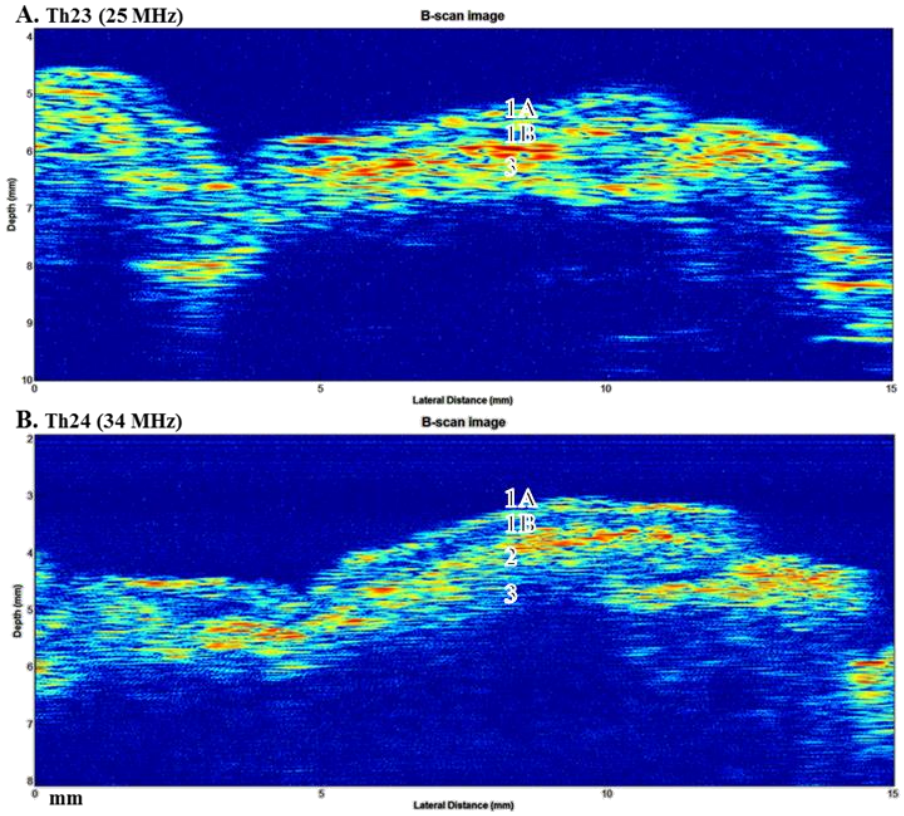

Figure 4.6A-B. Tissue from Case 2 was scanned at 25 and 34 MHz (A and B, respectively). Ultrasonic layers were depicted as hyperechoic (e.g. red-orange), hypoechoic (e.g. yellow-light blue) and anechoic (e.g. dark blue). The results showed enhanced resolution with increasing frequency. The 25 MHz scan demonstrated three layers with a first hyperechoic layer and second hypoechoic layer. The final layer was predominately hyperechoic with hypoechoic elements. At 34 MHz, four layers were detected. The first layer was a mixed hyper/hypoechoic layer. The second layer was predominately anechoic with scattered hypoechoic regions. The third layer was mixed hyper/hypoechoic and transitioned into a hypoechoic fourth and final layer.

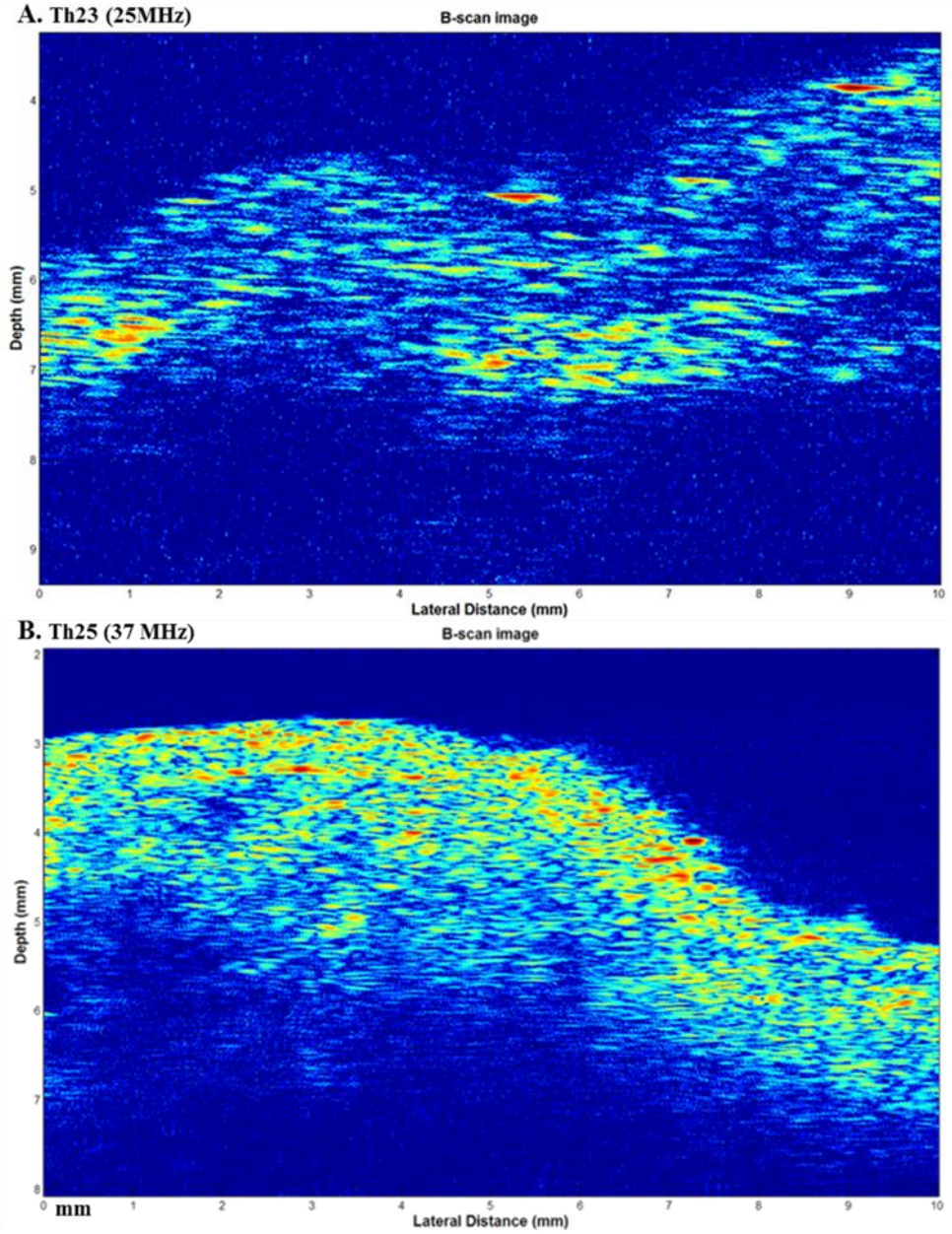

Figure 4.7A-B. Tissue from Case 3 was scanned at 25 and 37 MHz (A and B, respectively). Ultrasonic layers were depicted as hyperechoic (e.g. red-orange), hypoechoic (e.g. yellow-light blue) and anechoic (e.g. dark blue). At 25 MHz, the image was a mix of all three signal types, but no discernible layers were detected. At 37 MHz, signals were also a mix of all three signal types.

At 37 MHz, nine distinct ultrasonic layers were detected. The first layer was mixed hyper/hypoechoic, which was followed by a hypoechoic layer. The next layer was mixed hyper/hypoechoic and the fourth layer was hypoechoic. The fifth layer was hyperechoic. The sixth, seventh and eighth layers were hypoechoic, hyperechoic and hypoechoic, respectively. The final ninth layer was hyper/hypoechoic.

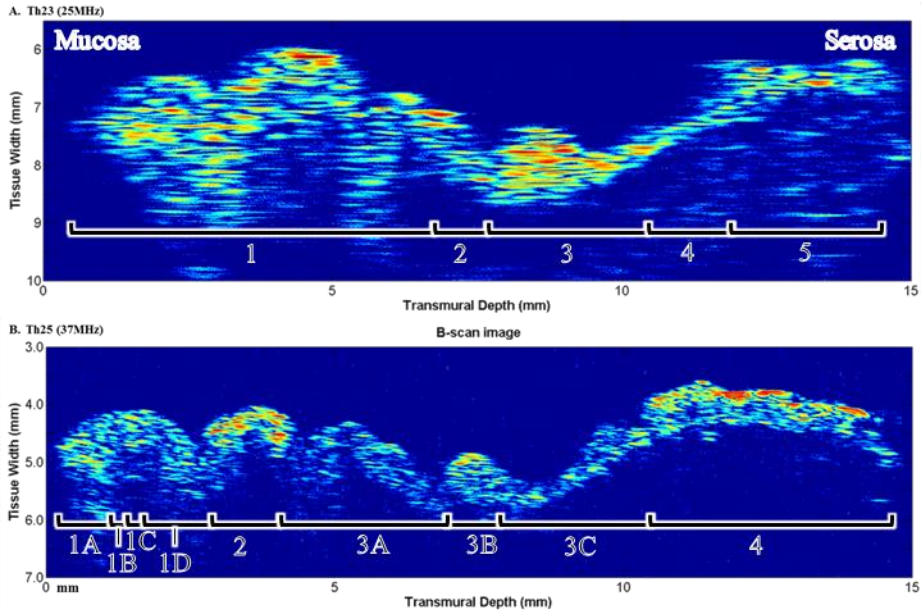

Fig 4.8A-B. Case 4 at 25 MHz and 37 MHz (A and B, respectively). The tissue was oriented so that each histological layer was scanned individually. Tissue was depicted by hyperechoic (orange-red) and hypoechoic (yellow-light blue) signals. At 25 MHz, five layers were revealed. The first layer was predominately hyperechoic with scattered hypoechoic regions. The second layer was hypoechoic and became hyperechoic to form the third layer. The fourth layer was hypoechoic and transitioned into a mixed hyper/hypoechoic final fifth layer. At 37 MHz, there were nine ultrasonic layers. The first layer encountered was mixed hyper/hypoechoic and was followed by a hypoechoic layer (1A-1B). The next layer was mixed hyper/hypoechoic and the fourth layer was hypoechoic (1C-1D). The fifth layer (2) was hyperechoic. The sixth, seventh and eighth layers were hypoechoic, hyperechoic and hypoechoic, respectively (3A-3C). The final layer was hyper/hypoechoic (4).

4.2.3. Case 5

Tissue from Case 5 was arranged with the serosa facing the transducer to generate a serosa to mucosa cross-sectional image (Figure 4.9). The tissue was scanned at 25 and 37 MHz. Image reconstruction and analysis was hampered by the poor signal-to-noise ratio (SNR). The 25 MHz scan has not been included. The 37 MHz scan showed mixed echoic signal types. There were five distinct signals on either side of a mixed hyperechoic/hypoechoic cluster located mid-tissue. The serosa was mixed hyperechoic/hypoechoic. The second and fourth layers were predominately anechoic, separated by a thin hypoechoic stripe. The final fifth signal, which corresponded to the mucosa, appeared as a patchy mix of all three signal types.

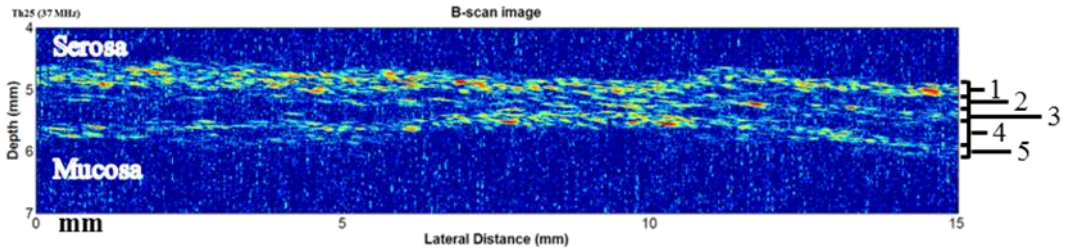

Figure 4.9. Tissue from Case 5 was scanned at 37 MHz and the serosa faced the transducer. Ultrasonic layers were depicted with hyperechoic (e.g. red-orange), hypoechoic (e.g. yellow-light blue) and anechoic (e.g. dark blue) signals, although the signal-to-noise ratio (SNR) was compromised. There were five distinct layers on either side of the mixed hyperechoic/hypoechoic cluster located at 8-11 mm along the horizontal axis. The superficial layer, which equated to the serosa, was mixed hyperechoic/hypoechoic. The second and fourth layers were predominately anechoic and were separated by a thin hypoechoic stripe. The final fifth layer, which corresponded to the mucosa, appeared as a patchy mix of all three signal types.

4.3. Discussion

Scanning of human tissue with high frequency single element transducers demonstrated that µUS can image colonic tissue with greater detail than standard 7-12 MHz frequencies. As expected, higher frequencies revealed not just the primary histologic layers, but also a number of sublayers. This was evident at the superficial level, as the number of distinct layers increased up to four separate layers versus the single layer seen at standard frequencies. Additionally, the results demonstrated a decrease in tissue penetration at deeper layers, as seen in Case 1 results.

One aim of this pilot study was to tentatively identify an optimal frequency for inclusion into Sonopill. My results indicated that ≈35 MHz is a potentially acceptable frequency; 34 and 37 MHz provided a high degree of superficial tissue detail. Furthermore, both frequencies demonstrated sufficient transmural penetration. Similar conclusions regarding 35 MHz were reached in an independent project on the µUS surveillance of Barrett's oesophagus using explanted pig oesophagus [209]. Confirming these preliminary conclusions will require a functional USCE operating at a similar centre frequency tested *in vivo*.

The second aim was to examine the relationship between high frequency µUS, detailed by acoustic tissue layers and histology. Histologically, the tissue from Case 1 appeared to be well organised and morphologically unremarkable. This was consistent with the µUS scan of the tissue showing distinct and well-demarcated acoustic layers. In fact, the 34 MHz scan closely resembled the acoustic-histologic relationship proposed by

Ødegaard *et al*. and introduced in Chapter 1 [36]. Nevertheless, none of the frequencies used depicted the myenteric plexus dividing the inner and outer muscles of the muscularis propria (MP). Histology from Case 2 showed a thickened submucosa (SM) and thinned MP. These morphological changes may have been detected by µUS. The scan showed a prominent hyperechoic band, which potentially corresponded to the thickened SM. Furthermore, the deep anechoic-hyperechoic bands normally associated with the MP were not detected. The results from Case 1 indicated that µUS was capable of replicating normal histology. The results from Case 2 indicated that µUS was capable of depicting pathophysiologic changes associated with age and/or disease [210]–[212].

Regardless, the standard orientation µUS scans failed to resolve the exact relationship between US layers and histology. A major contribution to this shortcoming was the lack of histology that corresponded more directly with scanned areas. While the slides provided an approximate picture of the state of the tissue. However, this resulted to considerable speculation when comparing scan results to histology. Any future studies will require sampling, both scanning and histology, from the same location.

By rearranging the tissue by 90° and 180°, the effects of tissue composition and layer interface on image generation could be further examined. Scans performed in the 90° orientation produced variable strength echoes that appeared to be arranged in distinct layers (Figure 4.8). This arrangement permitted each histological layer to be scanned separately. The signals generated were based predominately on the internal composition of each layer. The 90° scan at 37 MHz produced a multi-layered image that approximately matched Ødegaard's figure in terms of layer numbers and distribution (see Figure 1.6A-C, Chapter 1, page 13). A comparison of Case 1 and Case 4 revealed a similar echo pattern based on layer composition (Table 4.2). Case 4 results could be improved with better tissue support (e.g. suspending the sample) to prevent artificial elongation and weight-induced buckling. Additionally, placing the transducer closer to the tissue would better isolate the signal generated by each layer [56]. Tissue scanned in this orientation relationship offers an alternate means of looking at the ultrasound-histology relationship.

Tissue scanned at 180°, where the tissue interfaces were reversed, was intended to determine if this would produce a mirror image of a standard orientation scan. As the µUS wave travel was simply reversed, the potential to produce a mirror image seemed logical. However, reversing the order of tissue interfaces could potentially alter image generation. For instance, the smooth serosa would reflect µUS differently than the

Ultrasonic Layer	µUS (~35 MHz)		**Histology Layer** (1° Compostion)
	Standard Orientation	90° Orientation	
1A/1B	Hypoechoic/Anechoic	Hyperechoic/Hypoechoic	**Mucosa-Luminal Interface** (Single Layer of Epithelial Cells)
1C	Hyperechoic	Hyperechoic	**Mucosa-Lamina Propria** (Loose Connective Tissue)
1D	Anechoic/Hypoechoic Elements	Hypoechoic	**Mucosa-Muscularis Mucosae** (Smooth Muscle)
2	Hyperechoic	Hyperechoic	**Submucosa** (Dense Connective Tissue)
3A	Anechoic/Hypoechoic Elements	Hypoechoic	**Muscualris Propria-Inner** (Smooth Muscle in Ring Orientation)
3B		Hyperechoic	**Muscularis Propria-Myenteric Plexus** (Fibrous Nerve Bundle)
3C		Hypoechoic	**Muscualris Propria-Outer** (Smooth Muscle in Longitudinal Orientation)
4	Hyperechoic/Hypoechoic	Hyperechoic	**Serosa-Visceral Membrane** (Single Layer of Serosal Cells)
5	Hyperechoic	Hyperechoic	**Epiploic Appendices** (Fatty Appendages)

Table 4.2. Comparison of acoustic layers signal strength in standard (mucosa-to-serosa) and 90° (each layer scanned independently) orientations. Signals are also compared to the histological layers and primary composition of each layer.

irregular mucosal surface. It would be reasonable to expect a more specular reflection from the flatter serosa [56]. Unfortunately, the single result and poor SNR was insufficient to fully demonstrate the effect of reversing the tissue. Nevertheless, this method also represents a practical means of examining the ultrasound-histology relationship. This would be especially informative if done in conjunction with scanning of the same sample in both standard and reversed orientation.

4.4. Summary and Conclusion

In this chapter, I have described the results obtained from µUS scans on freshly acquired human colonic tissue scanned at various frequencies. This was done to identify a suitable frequency for USCE and further explore the ultrasound-histology relationship. Although constrained by a small sample size, particularly for the reoriented cases, the results of this pilot study met some of the stated aims. The results have indicated that a centre frequency of 35 MHz is a potentially suitable frequency for USCE inclusion. At ≈35 MHz, enhanced tissue detail and full transmural penetration were observed. Scan results were also compared to available histology. Case 1 scans replicated observed histological morphology and architecture. Tissue was also scanned in different orientations. Tissue scanned at 90° revealed an image based on layer composition alone. The intention of scanning at 180° was to show the effect of rearranging tissue interfaces on image generation.

Chapter 5. Pig Experiments

5. Chapter Introduction

This chapter describes the results obtained with a prototype USCE device *in vivo*. The purpose of these proof of concept experiments was to address the feasibility of USCE in the gastrointestinal (GI) tract. The primary clinical endpoint of this series of experiments was to determine whether sufficient coupling occurred between the capsule transducer(s) and the mucosa to generate a transmural microultrasound (μUS) bowel image in a suitably large mammal.

5.1. *In Vivo* Results

A total of 18 *in vivo* experiments were carried out with SonoCap, a tethered USCE prototype. Experiments were conducted in the oesophagus (N=6) and small bowel (N=12) in a living, anaesthetised pig. Scans were done in both static and dynamic capsule modes. Static imaging involved parking the capsule in a single position and scanning for 60 seconds. The dynamic mode involved operator retrieval or 'pullback' of the capsule with simultaneous imaging during motion. The purpose of the experiments was to determine whether the transducer(s) maintained contact with the bowel wall. It should be noted that capsule transducers were subject to movement due to normal physiologic activities such as bowel peristalsis, respiration, vessel pulsation and random muscle twitches. Furthermore, manual pullback could not be finely controlled and capsule speeds varied.

All case images are presented in 'Jet' colour format, showing hyperechoic (e.g. red-orange), hypoechoic (e.g. yellow-light blue) and anechoic (e.g. dark blue) signals.

5.1.1. Oesophagus

The prototype capsules were tested in three different stationary (i.e. static) oesophageal positions (e.g. distal, mid and proximal). The distal position equated to the gastroesophageal junction (GOJ) and the proximal position was located just below the shared area with the trachea (i.e. hypopharynx). Figure 5.1 represents a static oesophageal scan taken at the distal GOJ position for 60 seconds. The presence of potential tissue signals indicated that transducer to tissue coupling occurred.

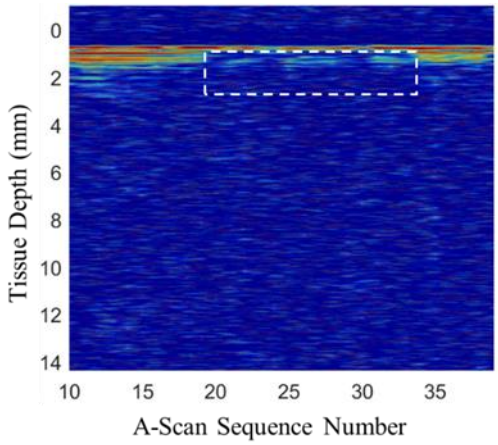

Figure 5.1. Static image of the gastroesophageal junction (GOJ) by a prototype ultrasound capsule endoscope (USCE) which used a single element 30 MHz transducer. Ultrasonic signals were depicted as hyperechoic (e.g. red-orange), hypoechoic (e.g. yellow-light blue) and anechoic (e.g. dark blue). Multiple A-scans were taken over a period of 60 seconds and compiled to create the figure. A-scans were averaged and filtered to remove the transducer pulse signal (i.e. ringdown) and improve the signal-to-noise ratio (SNR). Areas without a pulse signal revealed a tissue signal (dashed white box). The presence of a tissue signal indicated that good contact occurred between the transducer and tissue.

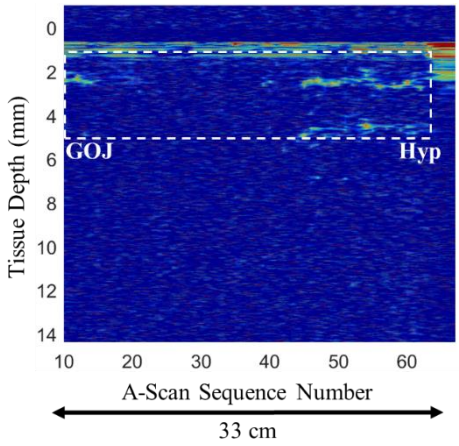

Figure 5.2. Dynamic scan of the oesophagus from the gastroesophageal junction (GOJ) to just below the hypopharynx. Scans were using a tethered prototype ultrasound capsule endoscope (USCE) with a single element 30 MHz transducer. Ultrasonic signals were depicted as hyperechoic (e.g. red-orange), hypoechoic (e.g. yellow-light blue) and anechoic (e.g. dark blue). Multiple A-scans covering the 33 cm scan length were taken during the 60-second pullback. A-scans have been averaged and filtered to remove the transducer pulse signal and improve the signal-to-noise ratio (SNR). Areas without a pulse signal revealed a tissue signal (dashed white box). The presence of a tissue signal indicated that good contact occurred between the transducer and tissue for the length of the pullback.

The results of the dynamic oesophageal scan are represented by Figure 5.2. In this particular case, the capsule was pulled back for 60 seconds from the GOJ to the hypopharynx over a distance of ≈33 cm. Tissue signals were present throughout the length of the scan. This indicated that the capsule transducer(s) maintained constant contact with the tissue during the length of the pullback.

5.1.2. Small Bowel

The capsule was introduced directly into the small bowel via a surgically created stoma which bypassed the oesophagus and stomach. Both static and dynamic scans were performed.

Static images of the bowel are presented in Figure 5.3. The capsule was placed into the small bowel and advanced approximately 20 cm beyond the stoma. Three sets of static images were recorded at 20, 13 and 6 cm from the stoma. Scans were performed over a period of 60 seconds and the resultant B-scan was created from the multiple A-scans. Good transducer to tissue contact was noted in the B-scans based on the appearance of tissue signals.

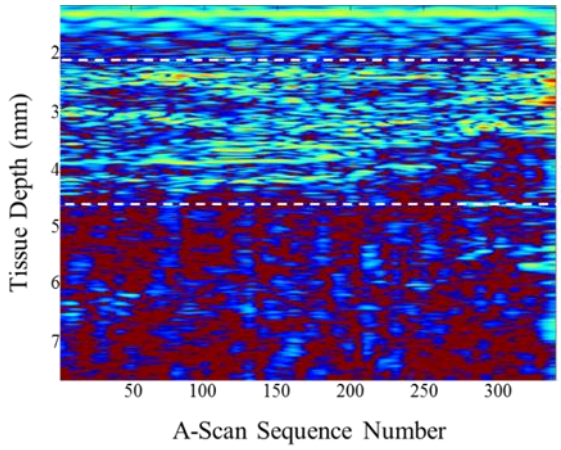

Figure 5.3. Static image of the small bowel by a prototype ultrasound capsule endoscope (USCE). Scans were achieved using a capsule-based single element 30 MHz transducer. Ultrasonic signals were depicted as hyperechoic (e.g. red-orange), hypoechoic (e.g. yellow-light blue) and anechoic (e.g. dark blue). Multiple A-scans taken over a period of 60 seconds were compiled to create the figure. A-scans have been averaged and filtered to remove the transducer pulse signal and improve the signal-to-noise ratio (SNR). Areas without pulse signal have revealed a tissue signal (dashed white box). The presence of a tissue signal indicated that good contact occurred between the transducer and tissue.

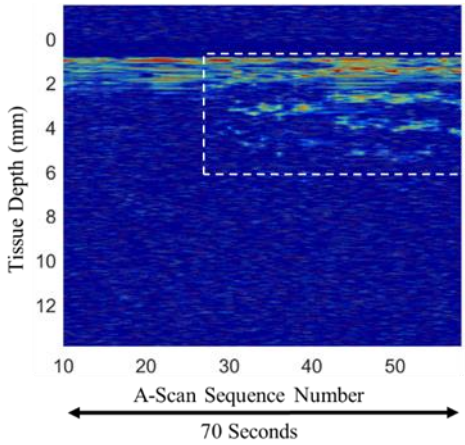

Figure 5.4. Dynamic image of the small bowel by a prototype ultrasound capsule endoscope (USCE). Scans were achieved using a capsule-based single element 30 MHz transducer. Ultrasonic signals were depicted as hyperechoic (e.g. red-orange), hypoechoic (e.g. yellow-light blue) and anechoic (e.g. dark blue). Multiple A-scans taken over a period of 70 seconds were compiled to create the figure. The presence of a tissue signal (dashed white box) indicated that good contact occurred between transducer and tissue.

Dynamic images of the small bowel are presented in Figure 5.4. The capsule was inserted into the stoma and advanced approximately 20 cm from the stoma. The capsule was then pulled back for 60 seconds. Again, good transducer to tissue contact was noted in the resultant B-scan, as indicated by tissue signals.

5.2. Shenzhen Capsule

Imaging results were also achieved using an alternative USCE. This tethered prototype was designed and manufactured by colleagues at Shenzhen University (Figure 5.5) [213], [214]. This device consisted of a 10 x 30 mm capsule. Unlike SonoCap where the transducers made direct tissue contact, the 30 MHz Shenzhen transducer was separated from the tissue by an acoustic window at a distance of ≈2 mm. In order to generate a 360° image, the transducer oscillated between 0° and 360° in an alternative clockwise and counter clockwise manner.

The results showed coupling between the capsule's acoustic window and transmural images of the oesophagus and small bowel were captured (Figure 5.6). Oesophageal results showed a single ultrasonic layer. An extra adventitial/serosal structure was also detected. This structure may have represented either a lymph node or blood vessel due to its cystic appearance. Images from the small bowel showed three distinct ultrasonic layers.

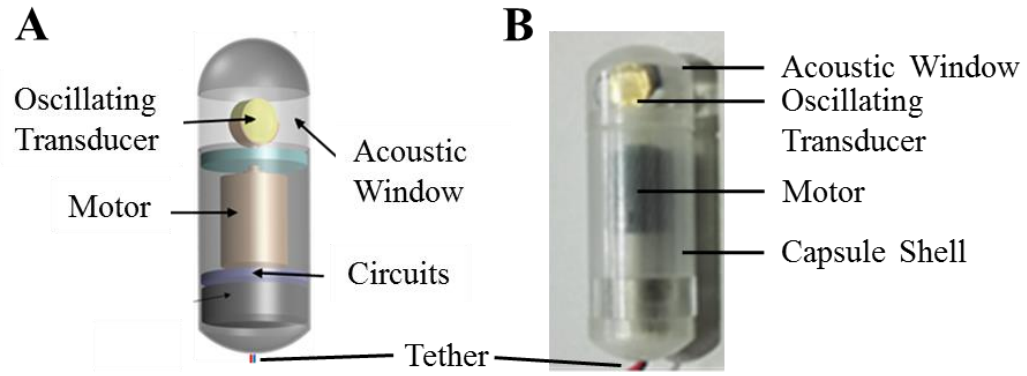

Figure 5.5A-B. A) Capsule schematic and (B) prototype ultrasound capsule endoscope (USCE) designed by colleagues at Shenzhen University. The 10 x 30 mm capsule used a 30 MHz single element transducer that oscillated 360°, which was driven by an alternating motor. The transducer was housed inside the capsule and separated from the tissue by ≈2 mm by an acoustic window. Power and data transfer were done via the capsule tether. Figures adapted from Qiu *et al*. [214].

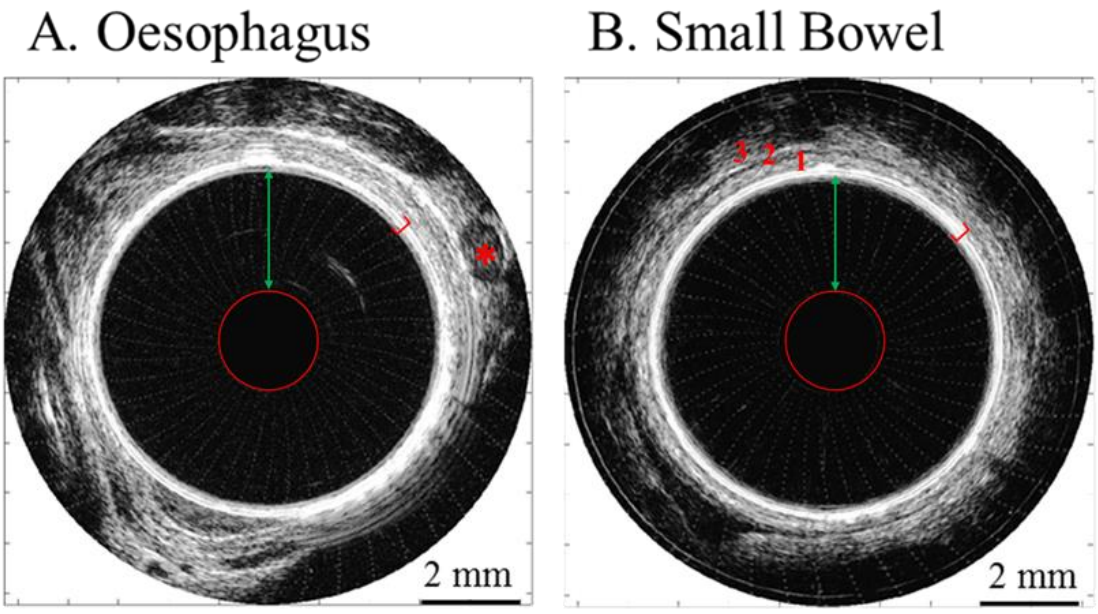

Figure 5.6A-B. Static grey scale ultrasound images of a pig's oesophagus (A) and small bowel (B). Both results demonstrated adequate capsule to tissue coupling. Both transducer (red circles) and coupling medium (green arrows) were isolated from direct tissue contact by an acoustic window. Ultrasound signals passed through an acoustic window (red brackets) in both pulse and echo modes. Both results demonstrated adequate capsule to tissue coupling. This resulted in good ultrasound representation of the tissue. This included distinct hyper/hypoechoic ultrasonic layers in the small bowel (red numbers 1-3) representing histologic layers. Furthermore, associated anatomic structures such as a vessel or node were seen in the periphery of the oesophagus (red asterisk).

5.3. Discussion

The purpose of the experiment discussed in this chapter was to test the feasibility of USCE *in vivo*. Specifically, the experiments were designed to determine whether adequate transducer to bowel wall contact occurred. Direct contact was required in order to generate transmural images.

This experiment demonstrated that satisfactory coupling occurred between the transducer and tissue and generated μUS bowel wall images. Good contact was demonstrated in the oesophagus and small bowel under static and dynamic conditions. These observations were an important milestone in providing crucial evidence regarding the feasibility of USCE as a diagnostic device [192]. Further evidence of USCE feasibility was observed using the alternative designed Shenzhen capsule. Satisfactory transmural tissue visualisation was achieved and included distinct small bowel ultrasonic layers and associated oesophageal structures.

The next step in USCE development is to improve image quality. It was evident that the prototype capsules were unable to clearly delineate ultrasonic tissue layers despite evidence of good tissue coupling. This issue may have arisen from the close proximity of the tissue and transducer [192]. Correcting this issue can be achieved by narrowing the focal distance of the transducers. This can be achieved by either further recessing the transducer(s) into the capsule or reducing the focal distance during transducer fabrication. There was some indication of ultrasonic layering, however, it is not known whether the acoustic layers corresponded to histologic bowel layers, neighbouring structures (e.g. adjacent bowel loops) or both. Shenzhen capsule tissue contact was facilitated by the acoustic window of the capsule. The 2 mm distance between the transducer and tissue assisted in producing better images and detecting distinct ultrasonic layers. This placed the tissue closer to the 8 mm focal distance of the transducer.

5.4. Summary and Conclusion

The results from this experiment demonstrated the feasibility of USCE *in vivo*. Establishing transducer to tissue contact was crucial step in USCE development. Insufficient contact would have compromised image generation and negatively affected USCE diagnostic capabilities. Proof of concept was achieved *in vivo* by two capsule prototypes. Further USCE development will require improved capsule and/or transducer design to improve tissue imaging.

Chapter 6. Mouse Experiments

6. Chapter Introduction

This chapter describes the results of mouse gastrointestinal (GI) inflammation experiments. The purpose of these experiments was twofold. The first objective was to determine whether high resolution microultrasound (µUS) could detect GI inflammation. The second objective was to determine the lowest grade of inflammation detectable. The results are reported per stage, which comprise Stages 1A, 1B, 2, 2B and 3. Stage 1 was a pilot study to determine the ability of µUS to detect overt (i.e. visually perceptible) inflammation. The aim of Stages 2 and 2B was to identify the lowest grade of inflammation detectable by µUS. The goal of Stage 3 was to identify the lowest grade of inflammation detectable by µUS in a randomised control trial (RCT).

6.1. Stage 1A and 1B

The purpose of Stages 1A and 1B was to determine the ability to detect high grade inflammation. Stage 1A was an all-male group (N=5) and four mice were treated with 5% (w/v) dextran sodium sulphate (DSS) in drinking water *ad libitum*. Stage 1B was an all-female group (N=5) and four mice were treated with 5% (w/v) DSS in drinking water *ad libitum*. Clinical information, including individual responses to DSS, are presented in Table 6.1.

ID	Sex	Trial	5% DSS	Cull Day	BPR	Stool	Discomfort
20171128M1	M	1A	+	5	-	-	+
20171128M2	M	1A	+	5	-	-	+
20171129M1	M	1A	+	6	-	-	+
20171129M2	M	1A	+	6	-	-	+
20171206M1	M	1A	-	0	-	-	-

ID	Sex	Trial	5% DSS	Cull Day	BPR	Stool	Discomfort
20180130M1	F	1B	+	4	+	+	+
20180130M2	F	1B	+	4	+	-	+
20180131M1	F	1B	+	5	-	-	-
20180131 M2	F	1B	+	5	-	-	-
20180201 M1	F	1B	-	0	-	-	-

Table 6.1. Stage 1A (top) and 1B (bottom) clinical response to dextran sodium sulphate (DSS). Blood per rectum (BPR), blood in stool (Stool) and discomfort (e.g. nest soiling, piloerection, hair removal and abnormal gait).

Baseline scans were done on untreated mice for both Stages 1A and 1B. Visually, baseline caecal tissue was uniformly translucent and negative for signs of blood (Figure 6.1). The µUS scan showed mixed echoic signals with three distinct layers. The acoustic layering was hyperechoic-hypoechoic-hyperechoic. This pattern was consistent along the length of the scan, with the transducer perpendicular to the tissue. Tissue width was relatively uniform at ≈0.2 mm. Histology revealed the caecum to be well-organised architecturally and morphologically uniform with a continuous, uninterrupted epithelial cell layer. Baseline small bowel tissue was uniformly translucent (Figure 6.2). Bowel vessels were visible. The µUS scan was performed across the short axis of the bowel. The resultant image was a mixed hyperechoic-hypoechoic image. Hyperechoic signals were predominately seen at deep serosal levels, which provided a degree of acoustic layering to the scans. A central, deep serosal hyperechoic signal corresponded to the fatty mesentery. The oblique histology cut appeared relatively normal, however, the angle of the cut blurred the division between the mucosa (M) and submucosa (SM) and the small bowel lacked characteristic villi. Nevertheless, bowel morphology, architecture and the cell population appeared to be normal. The baseline colon also appeared translucent with multiple folds that radiated out from a central trough (Figure 6.3). The µUS scan showed mixed signals ranging from anechoic to hyperechoic. At 37 MHz, µUS was able to distinguish colonic folds. The frequency was also sensitive enough to depict layering at the level of the muscularis propria (MP) and serosa (S). Although not apparent in Figure 6.3, hyperechoic signals were found at all levels of the bowel wall and not just at deep levels. The accompanying histology slide appeared well organised and showed normal morphology. The tissue was cut through a colonic fold and demonstrated a clear division between the M and SM. The cellular composition of the M appeared to be dominated by epithelial colonocytes and goblet cells (GC) that greatly outnumbered interstitial support cells. The M also contained an aggregate of lymphoid tissue that may have represented the colonic portion of GALT. The aggregation appeared well organised with clear borders between it and neighbouring tissue. The MP appeared well structured and organised.

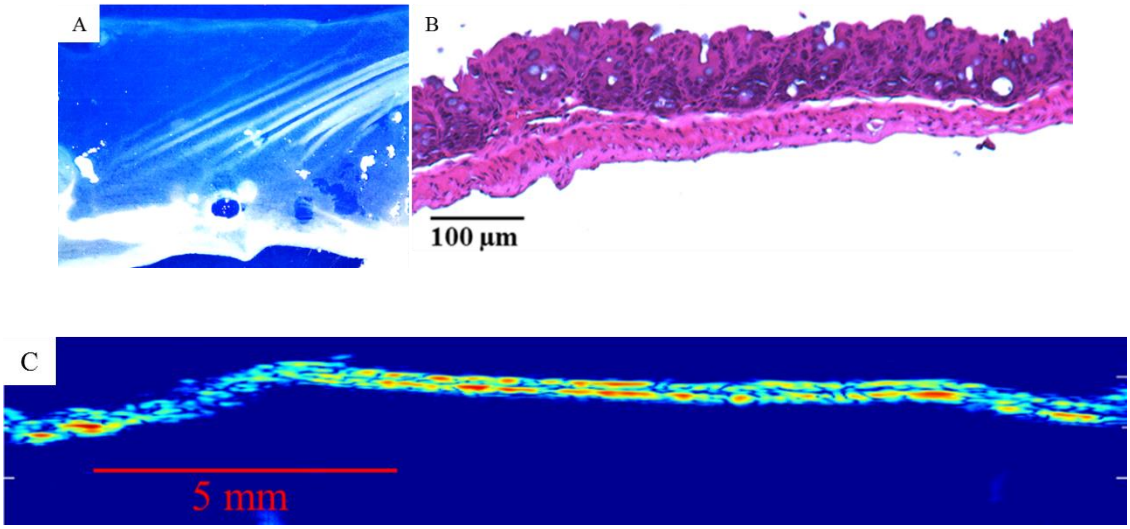

Figure 6.1A-C. Caecum result from a healthy mouse. (A) Dissection microscope image of the caecum showed a translucent organ without visible pathologic defects. (B) Haematoxylin and eosin histology revealed tissue that was architecturally and morphologically normal in appearance. The tissue was non-oedematous and consistent in appearance. (C) The corresponding microultrasound (µUS) scan was also predominately uniform in appearance. The scan was mixed hyperechoic (red-yellow) and hypoechoic (blue-green) with a central anechoic (dark blue) stripe forming three distinct layers. Angulation of the tissue appeared to have reduced the ability of µUS to discern all three layers, which is noted on the left-hand side of the scan.

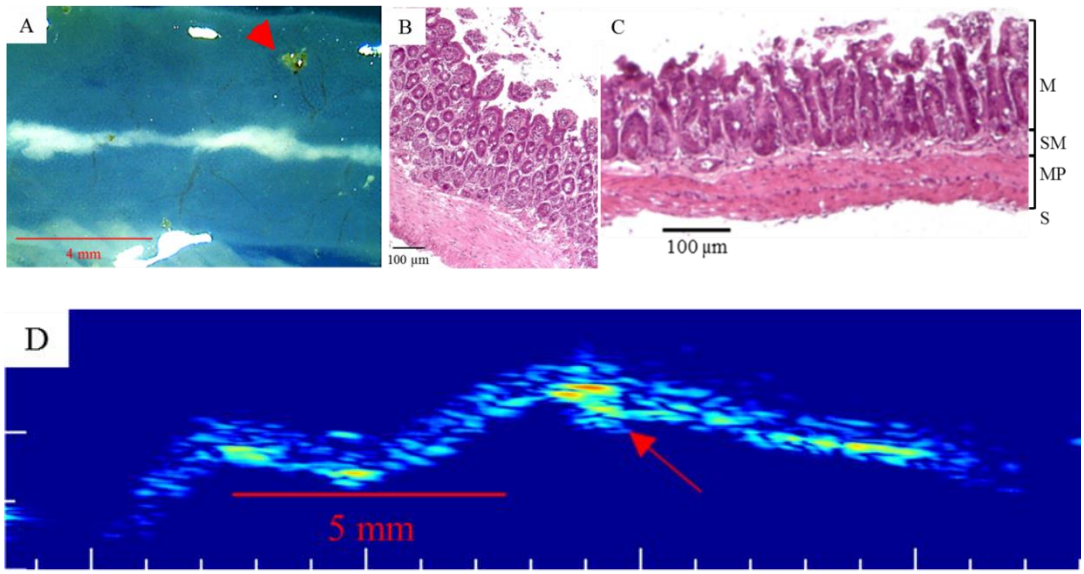

Figure 6.2A-D. Sample baseline small bowel result from an untreated mouse. (A) Photograph of the small bowel. The bowel was predominately translucent, permitting visualisation of the vasculature and the deep, fatty mesentery. While the tissue vasculature was seen, there were no signs of haemorrhagic lesions. Food residue (red arrow head) was also present, which could present as a superficial hyperechoic signal. (B) A haematoxylin and eosin slide of an oblique tissue cut. This slide lacked features normally associated with healthy tissue, such as prominent villi. The poor state of the tissue may have been due to tissue necrosis during scanning or inadequate fixation. (C) A perpendicular cut of a haematoxylin and eosin slide. Although this cut lacked villi, the submucosa (SM) was present. Crypts were tightly packed and lined with columnar epithelium. (D) Short axis microultrasound (µUS) scan of the small bowel featuring the mesentery (red arrow). The tissue signal was predominately hypoechoic (e.g. blue-green) with hyperechoic (e.g. red-yellow) elements in the deeper layers. The fatty mesentery was represented by the deep hyperechoic signal (red arrow). Mucosa (M), muscularis mucosae (Mm), muscularis propria (MP), serosa (S).

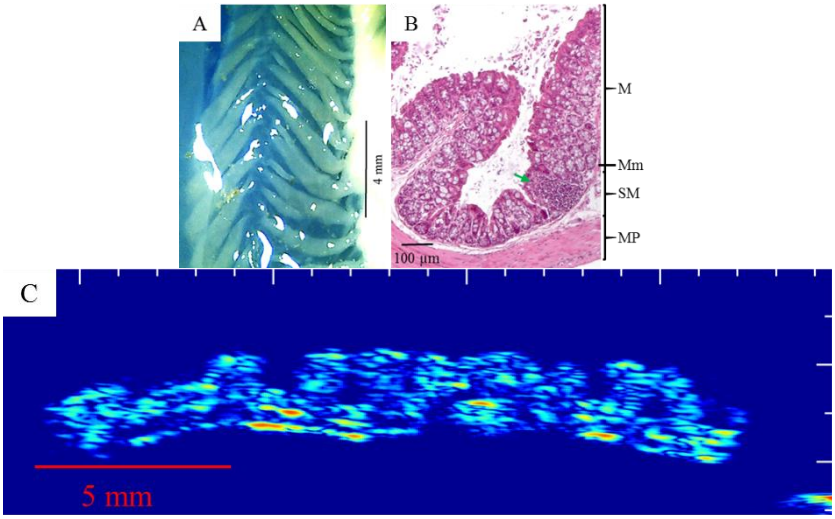

Figure 6.3A-C. Sample colon result from an untreated mouse. (A) Photograph of the proximal colon. Tissue was translucent and contained numerous folds along a central trough. Notably, there were minimal amounts of debris present. (B) Haematoxylin and eosin slide, the tissue was highly organised with clear histologic layers. The epithelium along the microfolds was continuous and housed numerous pale purple goblet cells. A cluster of immune cells (green arrow) was also present. This was most likely a normal (i.e. non-inflammatory) lymphoid nodule and not a collection of reactive cells. (C) Microultrasound (µUS) scan of the proximal colon across the short axis of the bowel. Signals ranged from hyperechoic to anechoic. The resultant image nicely demonstrated the colonic folds. The image also showed deep tissue layering, particularly on the left-hand side. An anechoic layer was present just above the mixed hyperechoic-hypoechoic serosa. Mucosa (M), muscularis mucosae (Mm), submucosa (SM), muscularis propria (MP).

All Stage 1A treated mice reached a humane endpoint by Days 5 (N=2) and 6 (N=2). Clinical signs of discomfort, which included behavioural indications of discomfort such as nest soiling, were observed (Table 6.1). Overt haemorrhagic lesions were noted post-mortem in the caecum of all four mice. The small bowel and colon of all mice were visually judged to be lesion free. Tissue with lesions was photographed, scanned and prepared for histological analysis (Figure 6.4).

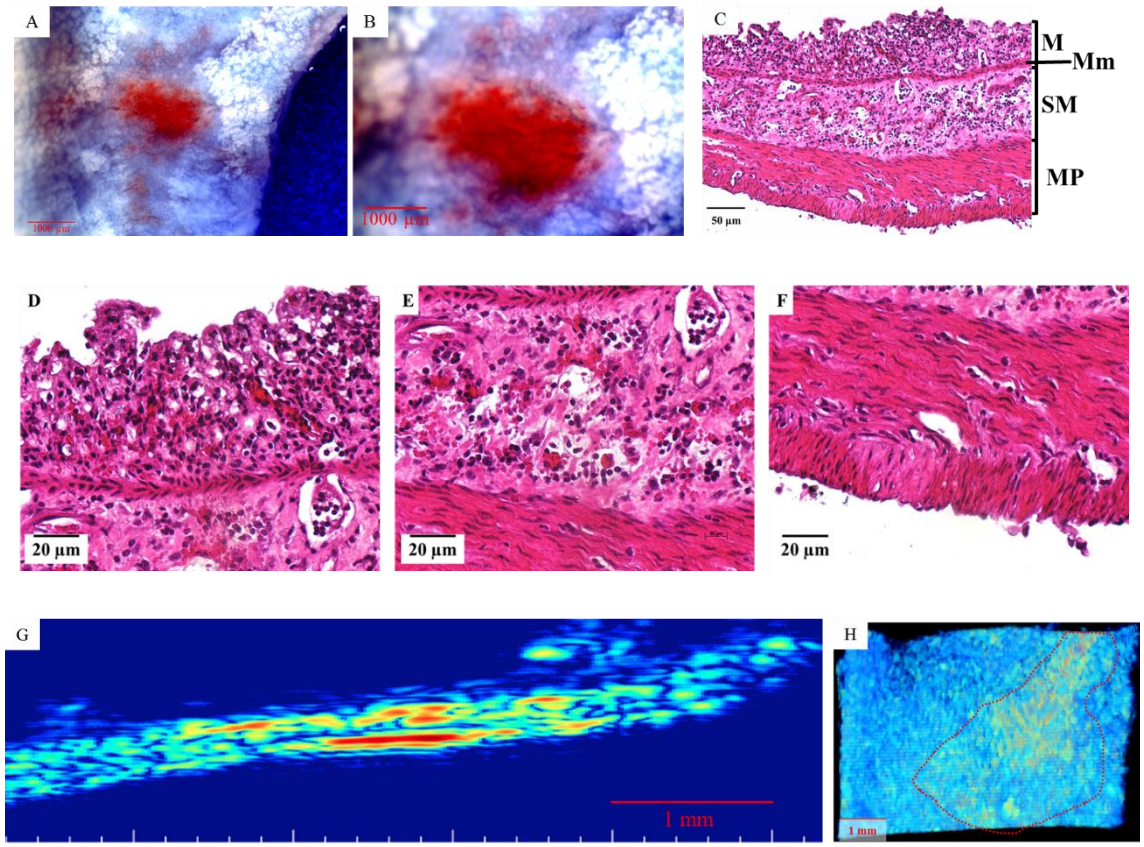

Figure 6.4A-H. Sample results from a Stage 1A mouse treated with dextran sodium sulphate (DSS) for five days. (A-B) Photographs of the caecum and associated lesion. Grossly, the lesion manifested as a bright red haemorrhagic wound that appeared to have breached the mucosal surface. At the periphery of the wound, the colour appeared muted, which possibly indicated a subsurface component to the lesion. (C) Haematoxylin and eosin staining revealed acute transmural inflammation with white cell infiltrates extending from the mucosa (M) to serosa. This was judged as severe transmural inflammation and equated to a grade of 3. There was also considerable morphologic change in relation to mucosal destruction, tissue oedema and the presence of extravasated red blood cells. (D-F) Magnified images of the image C, roughly mid-slide (D-Mucosa, E-Submucosa and F-Muscularis Propria). (G) Microultrasound (µUS) scan of the caecal lesion. This is a representative image slice which was 1 of 56 slices produced in total. The image showed a transmural hyperechoic (e.g. red-yellow) patch. The hyperechoic signal involved both mid and deep tissue layers, but not the uppermost superficial layer. This may have indicated the scan was at the periphery of the lesion and inflammation had not breached the surface. (D) Volumetric reconstruction using all 56 slices from the scan. The image was created using Volocity® (Volocity 5.5.1, PerkinElmer Inc., Waltham, US). The extent of the hyperechoic lesion is indicated by the dashed red line and includes subsurface components. Key: Muscularis mucosae (Mm), submucosa (SM), muscularis propria (MP).

In general, caecal lesions from Stage 1A appeared as bright red haemorrhagic lesions. The central portion of the lesions appeared to have breached the mucosal layer. The peripheral areas of the wound were muted red, indicating that these areas were most likely subsurface. µUS scans showed a hyperechoic (red-yellow) signal corresponding to the lesion. The hyperechoic signal was full thickness (i.e. M to S).

Haematoxylin and eosin (H&E) histology of 20171129M2 (Figure 6.4E-F) demonstrated acute transmural inflammation with white cell infiltrates extending from the M to S. Based on the large presence and the transmural infiltration of white cells, the lesion was judged to be severe, transmural and graded as a 3. There was also considerable morphologic change with regard to mucosal disruption, tissue oedema and the presence of extravasated red blood cells.

Stage 1B mice reached humane endpoints by Days 4 (N=2) and 5 (N=2). Visible haemorrhagic lesions were noted in the small bowel (N=1), caecum (N=1) and colon (N=1) of three individual mice (i.e. one lesion per animal). One mouse was lesion free upon visual inspection.

The small bowel sample with the visible lesion was photographed, scanned and prepared for histological analysis (Figure 6.5). On visual inspection, the small bowel lesion was located in the mid-ileum and appeared to have two small haemorrhagic lesions along the mesentery. Approximately mid-tissue, part of the ileum appeared to have a muted red appearance compared to the rest of the tissue. This was judged to potentially indicate inflammation and a 37 MHz scan was performed along the long axis. The tissue was predominately hypoechoic, unless the lesion or fatty mesentery, which were hyperechoic, were in the scan plane. The lesion appeared transmural with the mesentery located on the deep (i.e. serosal) side of the bowel. Histology of the ileum was compromised, possibly due to poor preservation and an oblique cut. Determining whether the tissue was inflamed was not possible. A small cluster of immune cells was noted; however, this may have represented a baseline feature.

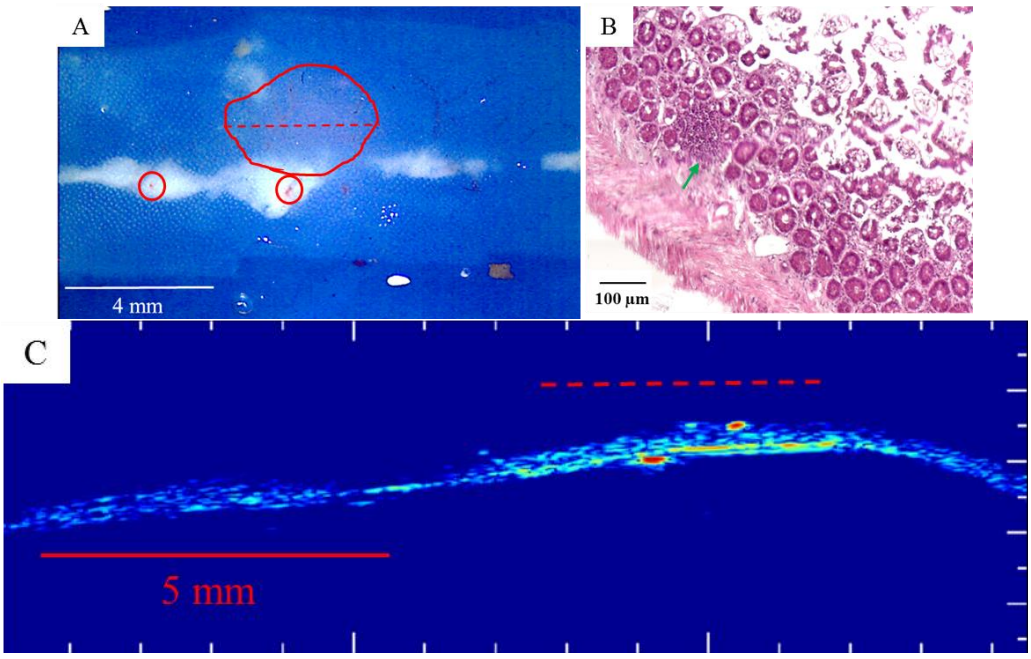

Figure 6.5A-C. Sample small bowel result from a Stage 1B mouse treated with dextran sodium sulphate (DSS) for four days. (A) Photograph of the small bowel at mid-ileum. The tissue appeared to have two pinpoint haemorrhagic lesions along the mesentery. Additionally, a slight opaque discolouration is encircled by the red line. It was suspected that this represented an area of inflammation. (B) Haematoxylin and eosin slide of the opaque area. Poor preservation and an oblique cut compromised tissue interpretation. Familiar landmarks such as the submucosa (SM) and signature villi of the small bowel were absent. The cause, whether due to necrosis during scanning, inflammation or poor fixation, was unknown. There was a cluster of immune cells present in the deep mucosa (green arrow). Determining whether the cluster was a baseline structure or induced was not possible. (C) The opaque area was scanned at 37 MHz along the long axis of the ileum. The scan was roughly mid-lesion, which is marked by the dashed red line in Figure 6.3A. The resultant image showed an area of enhanced echogenicity. The signal appeared transmural, which indicated an inflammatory response had occurred, however, this could not be definitely correlated by histology.

The proximal colonic lesion was bright red centrally with a muted red periphery (Figure 6.6). Again, this indicated the central portion breached the surface layer while the peripheral areas remained subsurface. The lesion was located along the mesentery of the colon. There was also a high degree of faecal debris. The µUS scan was mixed signal with two superficial hyperechoic signals. One signal corresponded to the lesion location whilst the second signal may have depicted the faecal debris. Histology revealed a surface to mid-tissue acute inflammatory process that spared the deeper MP. The inflammatory grade was considered 2 solely due to the location of infiltrates. Normal surface features were absent, including the loss of the epithelial lining.

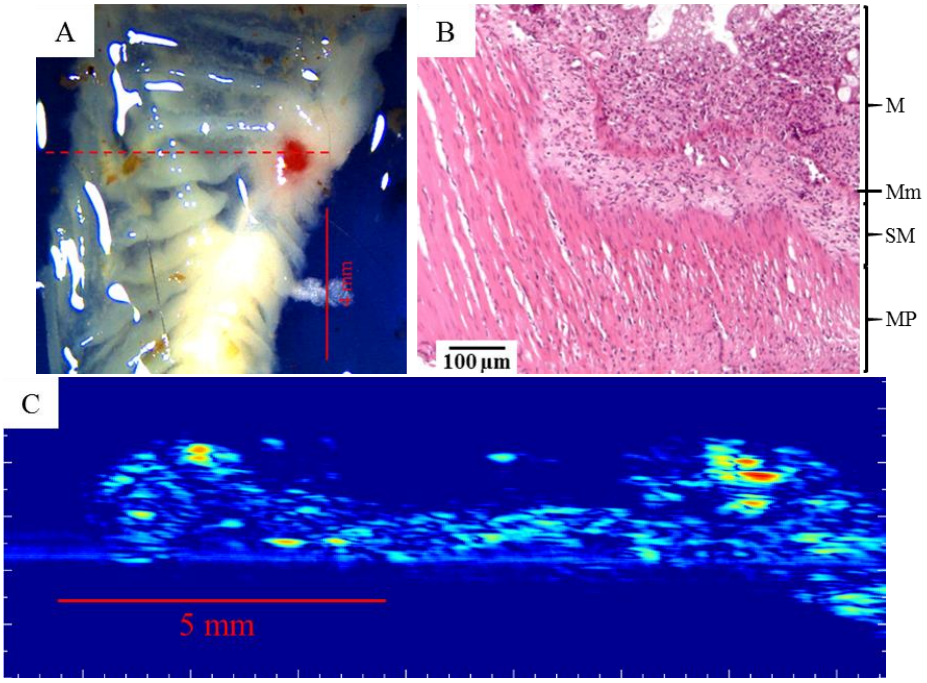

Figure 6.6A-C. Sample colon result from a Stage 1B mouse treated with dextran sodium sulphate (DSS) for five days. (A) Photograph of the proximal bowel and associated lesion. The tissue was characterised by multiple folds. There was a bright red lesion present on the mesentery. The lesion appeared as a bright red spot which was muted in the peripheral areas. (B) Haematoxylin and eosin staining revealed acute inflammation with white cell infiltrates which extended from the mucosa (M) to submucosa (SM). The muscularis propria (MP) appeared to be free from infiltrates, thus the inflammatory grade was considered 2 solely due to the location of infiltrates. The mucosal epithelium was compromised and accompanied by the loss of normal features, but did not extend beyond the M. The representative microultrasound (µUS) slice was from the dashed red line on the camera image. The signal was mixed, ranging from hyperechoic to anechoic. The hyperechoic signal on the right side corresponded with the location of the lesion. In this instance, the signal was not transmural. It extended from the surface to mid-tissue. There was a second superficial hyperechoic signal located on the left side of the tissue. This signal potentially corresponded to the debris seen on the camera image. N.B. It should be noted that this slide was potentially incorrectly labelled and attributed to the second mouse day 5 mouse scanned that day. This was due to a clerical error. Nevertheless, the histology slide represents an inflamed colon after treatment with DSS after five days. Muscularis mucosae (Mm).

The results from Stages 1A and 1B indicated that µUS could detect overt inflammation. This satisfied the criteria for advancing to Stage 2.

6.2. Stage 2

The purpose of Stage 2 was to determine the lowest grade of inflammation detectable by µUS. Mice were treated with 5% DSS in drinking water. Each day, one pair of mice, one female and one male, were culled and scanned. This provided data for 12 mice (six males and six females). Culls began on Day 0 (i.e. baseline) and ended on Day 4. This created a variable length of exposure to DSS and induced graduated inflammatory levels depending on the length of exposure. No animal reached the predetermined humane endpoints (Table 6.2). Behavioural changes were not encountered until Days 3 and 4. Positive GI bleeding, confirmed at post-mortem, was not encountered until Day 4 and was present in both mice.

ID	Sex	Trial	5% DSS	Cull Day	BPR	Stool	Discomfort
20180219M1	F	2	-	0	-	-	-
20180219M2	M	2	-	0	-	-	-
20180220M1	M	2	+	1	-	-	-
20180220M2	F	2	+	1	-	-	-
20180220M3	F	2	+	1	-	-	-
20180221M1	F	2	+	2	-	-	-
20180221M2	M	2	+	2	-	-	-
20180221M3	M	2	+	2	-	-	-
20180222M1	M	2	+	3	-	-	-
20180222M2	F	2	+	3	-	-	+
20180223M1	F	2	+	4	+	-	+
20180223M2	M	2	+	4	+	-	+

Table 6.2. Stage 2 clinical response to dextran sodium sulphate (DSS). Blood per rectum (BPR), test for blood in stool (Stool) and discomfort (e.g. nest soiling, piloerection, hair removal and abnormal gait).

ID	DSS	Day	Small Bowel	Caecum	Colon
20180219M1	-	0	1	1	X
20180219M2	-	0	1	1	1
20180220M1	+	1	0	2	1
20180220M2	+	1	X	2	2
20180221M1	+	2	1	1	0
20180221M2	+	2	0	2	1
20180222M1	+	3	1	2	X
20180222M2	+	3	1	1	2
20180223M1	+	4	2	X	X
20180223M2	+	4	1	3	2

Table 6.3. Stage 2 histological response to dextran sodium sulphate (DSS). 'X' indicates that the slide was illegible due to poor preservation, missing during shipping or poorly digitised (i.e. out of focus).

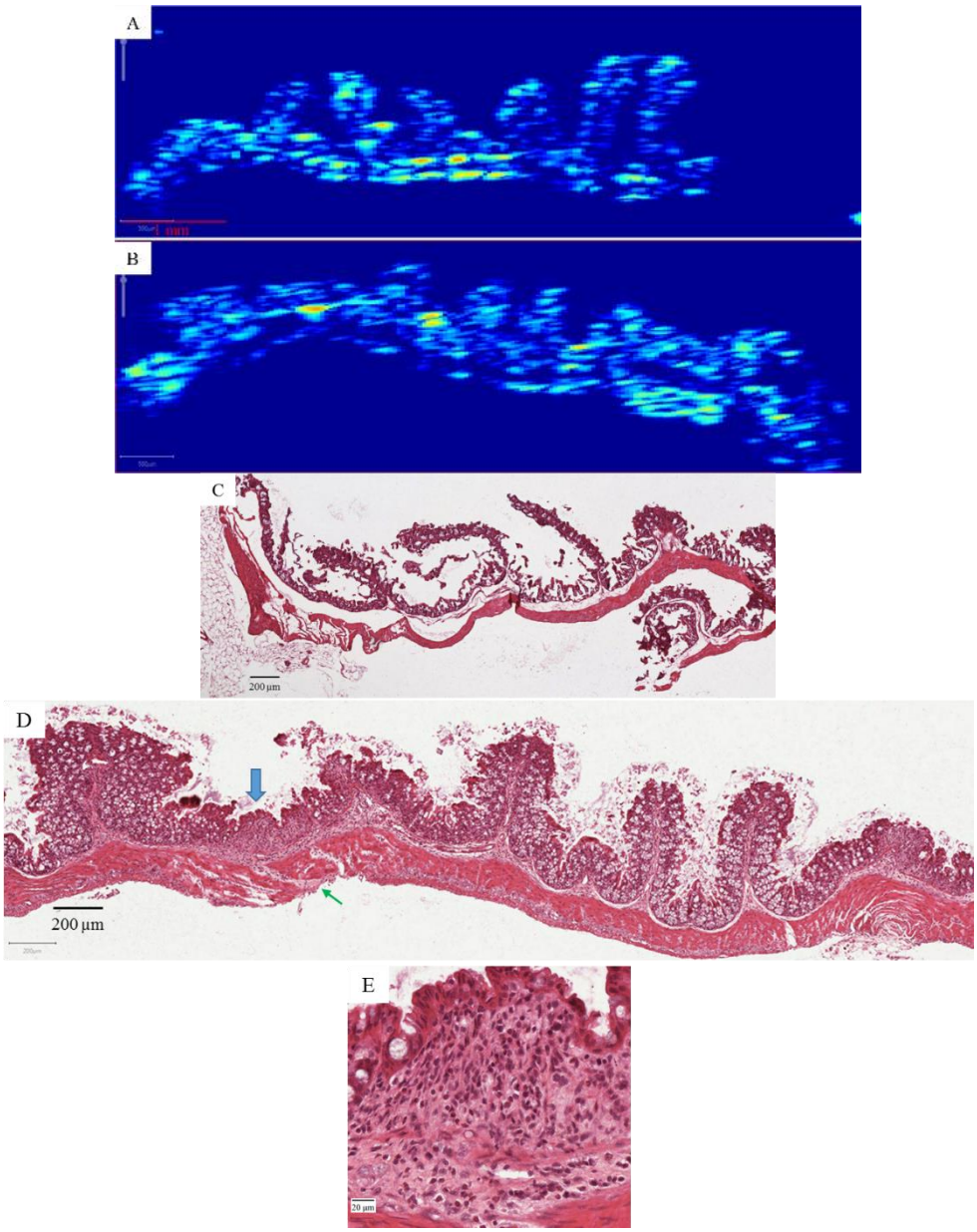

Figure 6.7A-E. Colon results from Stage 2. Microultrasound (µUS) of scans of an untreated mouse (A) and treated mouse after four days of 5% dextran sodium sulphate (DSS) (B). The baseline scan signals were predominately hypoechoic (e.g. blue-green) with scattered hyperechoic (e.g. red-yellow) and anechoic (e.g. dark blue) elements. Hyperechoic elements were largely found in the deep tissue, forming distinct layers in conjunction with the anechoic signals. Superficial hyperechoic signals may have been due to debris signals. Tall colonic folds could be easily seen across the short axis of the bowel. The scan from the treated mouse was also a mix of all three signal types. The hyperechoic signals were shifted more superficially and appeared more scattered. Nevertheless, the deep tissue layering was preserved. Transmural dimensions appeared thicker and colonic folds also appeared shortened, which may have resulted from oedema. Corresponding haematoxylin and eosin slides of the untreated colon (C) and treated mouse (D). Despite its poor state of preservation, the untreated colon appeared free from inflammation. Long colonic folds could also be seen on histology which accorded with the µUS scan. Histology from the treated colon demonstrated inflamed section of bowel. (E) Confluent white cell infiltration at the level of the mucosa (M) and submucosa (SM) were seen in a magnified section (Image D, blue arrow). Infiltration into the muscularis propria (MP) was also noted (green arrow). Inflammation was graded as Grade 2 with minor transmural elements (i.e. Grade 3). The mucosa appeared largely intact and the colonic folds could be identified, albeit stunted, as seen in the µUS scan. Additionally, the tissue appeared thickened transmurally.

No overt (i.e. haemorrhagic) lesions were noted on *post-mortem* optical examination, which included the mice with blood per rectum. Scanning failed to reveal any appreciable difference between untreated and treated mice. On the other hand, histology demonstrated variable grades of inflammation and was noted as early as Day 1 (Table 6.3). Early onset inflammation was confined to the M and graded 1. The lesions were patchy and very small (e.g. <100 μm) in size. Further histological analysis showed an evolving inflammatory process resulting in Grades 2 (i.e. M + SM) and 3 (i.e. transmural) being encountered by Day 4. A qualitative μUS comparison between Day 0 and Day 4 failed to reveal any difference despite histological evidence of grade 2-3 inflammation on Day 4 (Figure 6.7). Nonspecific signs of inflammation such as tissue oedema could be noted on μUS scans.

The decision to advance from Stage 2 to 3 before having all the data from stage 2 became necessary because of a very long delay in being able to process the histology slides from stage 2 samples. The University of Dundee histology slide scanner and associated software were not available due to technical issue and it took a while before it emerged that alternative services would have to be used and I sent my slides to University of Glasgow to be scanned. The time required to then receive the scans, meant that the scheduled start for Stage 3 occurred before a thorough analysis was completed. Thus, I made the decision to progress to Stage 3 based on positive results from Stage 1A/B and the availability of the appropriate animals at the time (e.g. sufficient numbers, acceptable age, and sex matched). A further delay would have required additional animals to be bred and reared until an acceptable age.

6.3. Stage 3

Stage 3 was done to determine the lowest inflammatory grade detectable in a RCT. The author was blinded to treatment status. This involved 16 mice in total (N=16). Treated mice were provided 5% DSS (w/v) in the drinking water *ad libitum*. All mice underwent daily observations which included health assessment, weigh-in and faecal examination, with records remaining sealed until the study was completed (Table 6.4). Behavioural information related to GI inflammation was not recorded in this instance.

Blinded histological review of the tissue confirmed inflammation (Table 6.5). Importantly, low grade inflammation was detected in non-treated mice. The baseline presence of inflammation may have been due to bacterial contamination in the mouse facility. It was reported that mice were harbouring *Klebsiella* (*K. oxytoca, K.*

pneumoniae) following faecal analysis [215]. *Klebsiella* is considered an opportunistic pathogen which may have had a baseline affect mouse bowel [216]. Good tissue preservation and H&E staining was consistently seen with the colon and to a lesser degree, the caecum. This permitted reliable grading of the inflammatory state of colonic tissue with a good degree of confidence. The small bowel samples, however, did not preserve well and were judged to be a poor indicator of inflammation and grading.

µUS results were reviewed without knowledge of treatment status. By comparing results against one another, it was determined that there were no definitive qualitative differences between the scans. The results were also compared against other baseline (i.e. DSS negative) scans which, again, resulted in no appreciable difference between scans. This

ID	Sex	Trial	5% DSS	Cull Day	BPR	Stool
20180906M1	F	3	-	0	-	-
20180906M2	F	3	-	0	-	-
20180907M1	F	3	+	2	-	-
20180907M2	F	3	+	2	-	-
20180910M1	F	3	+	3	-	-
20180910M2	F	3	-	0	-	-
20180911M1	F	3	+	4	-	-
20180912M1	M	3	+	2	-	-
20180912M2	M	3	+	2	-	-
20180914M1	F	3	+	4	+	-
20180914M2	F	3	+	4	+	-
20180917M1	M	3	-	0	-	-
20180917M2	M	3	-	0	-	-
20180918M1	M	3	+	4	+	-
20180919M1	F	3	+	2	-	-
20180919M2	F	3	+	2	-	-

Table 6.4. Stage 3 clinical response to dextran sodium sulphate (DSS). Blood per rectum (BPR), blood in stool (Stool).

ID	DSS	Day	Caecum	Colon	Small Bowel
20180906M1	-	0	0	1	0
20180906M2	-	0	1	1	0
20180907M1	+	2	0	2	1
20180907M2	+	2	2	2	x
20180910M1	+	3	1	3	0
20180910M2	-	0	0	1	0
20180911M1	+	4	1	2	0
20180912M1	+	2	2	1	0
20180912M2	+	2	0	2	1
20180914M1	+	4	1	3	1
20180914M2	+	4	1	0	1
20180917M1	-	0	0	0	0
20180917M2	-	0	0	1	1
20180918M1	+	4	1	2	1
20180919M1	+	2	2	1	1
20180919M2	+	2	2	1	1

Table 6.5. Stage 3 histological response to dextran sodium sulphate (DSS). Length of treatment (Day), treated (+), healthy (0), mucosal inflammation (1), mucosal and submucosal inflammation (2), transmural inflammation (3), unknown (x).

indicated that µUS at 37 MHz could not distinguish between healthy tissue and mild grades of inflammation in mice.

6.4. Stage 2B

Stage 2B occurred after Stage 3 as the higher frequency transducers were not available until after the completion of Stage 3. Stage 2B was conducted in a similar manner as Stage 2. The purpose of Stage 2B was to determine whether lower grades of inflammation could be detected using a higher frequency transducer. The frequency was increased from 37 MHz to 62 MHz, which provided enhanced image resolution. Inflammation was generated using the protocol from Stage 2 with culls occurring on Days 0, 2, 3 and 4. Day 1 was omitted due to a small sample size (N=7) and the experience that nascent inflammation was too difficult to detect ultrasonically and be confirmed with histology. Stage 2B consisted of three females and four males, of which two females differed genetically from the standard wild-type mice (Table 6.6). The two females were heterozygote mutants for the adenomatous polyposis coli ($Apc^{Min/+}$) gene, a murine model of human familial adenomatous polyposis (FAP). It was suspected that $Apc^{Min/+}$ may display increased sensitivity to DSS, otherwise the inclusion of these mice was not expected to dramatically affect the results [217], [218]

ID	Sex	Strain	Trial	5% DSS	Cull Day	BPR	Stool	Discomfort
20190128M1	F	WT (BLK6)	2B	-	0	-	-	-
20190130M1	M	WT (BLK6)	2B	+	2	-	-	-
20190130M2	M	WT (BLK6)	2B	+	2	-	-	-
20190131M1	F	Apc^{min}	2B	+	3	-	-	-
20190131M2	F	Apc^{min}	2B	+	3	-	-*	+
20190201M1	M	WT (BLK6)	2B	+	4	-	-	+
20190201M2	M	WT (BLK6)	2B	+	4	-	-	+

Table 6.6. Stage 2B clinical response to Dextran Sodium Sulphate. Dextran Sodium Sulphate (DSS), Blood Per Rectum (BPR), Blood in Stool (Stool), Blood in stool at *post-mortem* examination (*) and discomfort (e.g. nest soiling, piloerection, hair removal and abnormal gait).

µUS results at 62 MHz demonstrated an enhanced resolution over the previously employed 37 MHz, as expected (Figure 6.8). The higher frequency was able to discern smaller microstructures and provided improved resolution in both the axial and lateral direction. Immediately noticeable was the reduction of anechoic signals within the tissue. There was also an improved definition of the deep tissue layers of the colon at the level of the MP and S. This was indicated by the consistent presence of a hypoechoic band that resided between two hyperechoic stripes. No other ultrasonic layers, such as the interface between the M and SM, were noted.

Inflammation was detected by histology (Table 6.7). Despite the improved resolution, definitive µUS signs of inflammation could not be discerned. A comparison of an

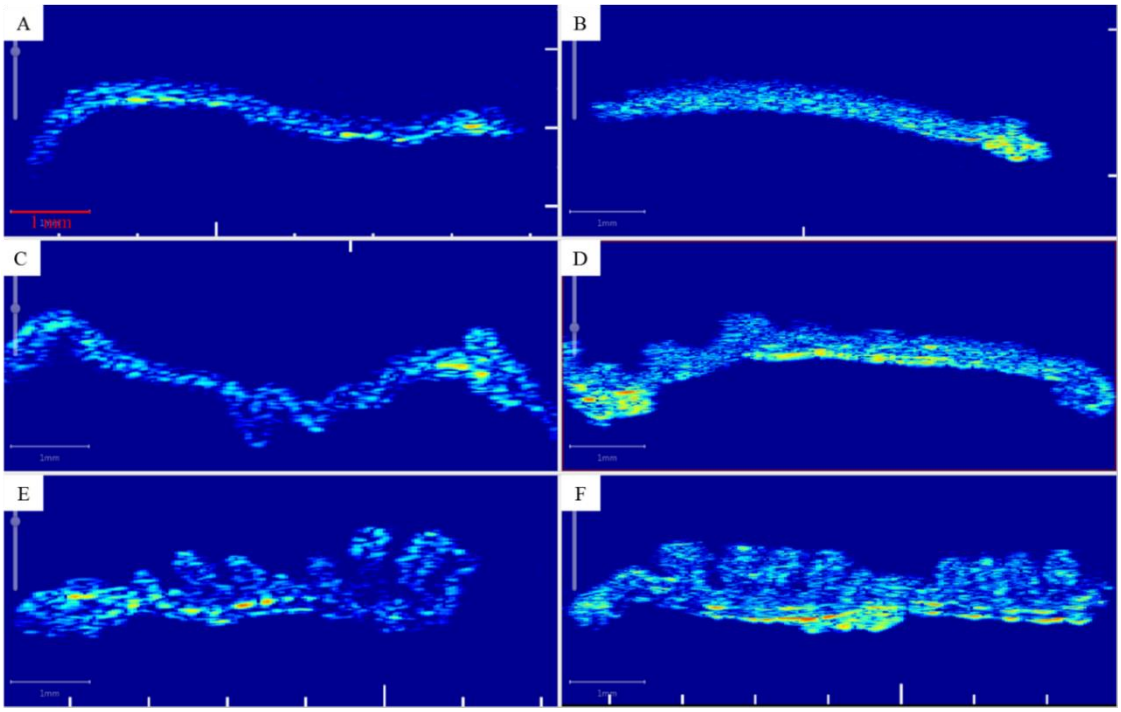

Figure 6.8A-F. Comparison of scans at 37 MHz (left column) against 62 MHz (right column) for the three anatomic sites. Scans are of the small bowel (A-B), caecum (C-D) and colon (E-F). Scans are of untreated mice from Stages 2 and 2B. Images at 62 MHz demonstrated enhanced resolution. Details from deeper tissue layers can be noted in all three anatomic sites due to the improved axial and lateral resolution. In the 62 MHz colon scan (F), the consistent presence of a deep hypoechoic band that resided between two hyperechoic stripes.

ID	DSS	Day	SB	Cae	Co
20190128M1	-	0	1	1	1
20190130M1	-	2	X	1	2
20190130M2	+	2	0	1	1
20190131M1	+	3	1	2	2
20190131M2	+	3	2	2	2
20190201M1	+	4	2	2	2
20190201M2	+	4	2	2	3

Table 6.7. Stage 2B histological response to dextran sodium sulphate (DSS). 'X' indicates that the slide was illegible due to poor tissue preservation.

untreated Day 0 mouse against two treated mice with histological signs of inflammation failed to reveal any acoustic indications of inflammation (Figure 6.9).

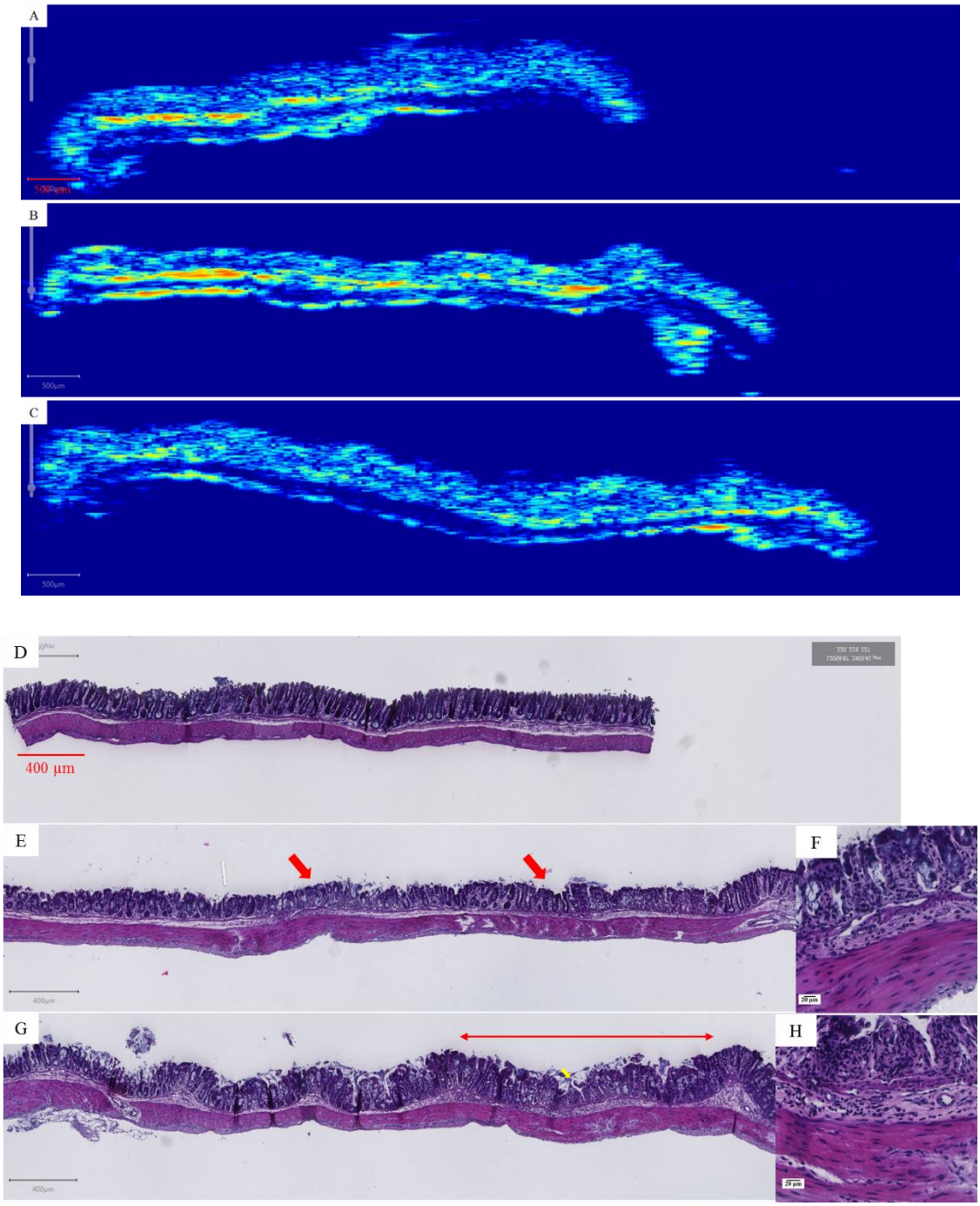

Figure 6.9A-H. Microultrasound (µUS) and histology results from Stage 2B. Representative results are from the distal colons of an untreated mouse (A and D) and two mice after four days of dextran sodium sulphate (DSS) treatment (M1: B, E and F, M2: C, G and H). Both treated mice demonstrated histological signs of inflammation. Inflammatory cell infiltration for M1 (E) was grade 2, but patchy (red arrows). (F) Magnified area from left red arrow. Inflammatory cell infiltration for M2 (G) was also grade 2 but was considerably larger and confluent (double-headed red arrow, H Magnified area at yellow arrow). The untreated mouse colon (D) was unremarkable and appeared to be healthy and without white cell infiltrates. However, the associated µUS scans of M1 (B) and M2 (C) failed to reveal any definitive signs of inflammation when compared to the untreated mouse (A).

6.5. Discussion

The first objective of this set of experiments was to determine whether high resolution µUS could detect GI inflammation. The second objective was to determine the lowest grade of inflammation detectable. Initial results indicated that detection of high grade (i.e. severe), transmural inflammation was possible, and coincided with clear optical signs of inflammation in the form of visible bright red haemorrhagic lesions. However, my experiment failed to reveal any direct µUS signs of low grade (i.e. milder) inflammation using 37 and 62 MHz.

Initially, µUS analysis was hampered by the presence of faecal debris which had the potential to be viewed as a lesion as it produced superficial hyperechoic signals. Improved cleaning methods reduced the amount of debris and improved the ability to rule out debris-generated signals. This was done by aligning the scan results with camera images using landmarks visible in both modalities (e.g. air bubbles or specific anatomic cues). µUS signs of debris that corresponded with optical signs were discounted as false positive and unexplained signals that remained were considered to potentially indicate inflammation. However, aligning the suspicious signals with histology proved far more challenging. A significant challenge in this study was the difficulty of precisely aligning scan data with histological data. This was in part due to the scale difference of the two modalities. Histology scales are in µm while µUS scales are in mm. Furthermore, histology slices lacked the large-scale landmarks to assist with matching scan slices. In other words, histology results could only be approximated to either a proximal or distal location along an anatomical sample. With stage 2B tissue samples, I attempted to narrow anatomic locations by dividing each tissue sample into quarters. Each 4 mm quarter sample was labelled as proximal, mid-proximal, mid-distal and distal. The same division was also applied to each µUS scan. This resulted in a slight improvement in aligning the two images from both modalities, but a degree of uncertainty still remained. This uncertainty was further exacerbated by the seemingly random hyperechoic signals distributed throughout all tissue depths in both treated and untreated tissue. Without the ability to precisely align a scan slice with the corresponding histology slice, hyperechoic signals could not be interpreted as true positive (i.e. inflammation) or false positive with confidence.

It is also possible that the detection of low-grade inflammation in mouse bowel is limited by the resolution of the two utilised frequencies. The µUS wavelengths at 37 and 62 MHz are 0.04 mm and 0.02 mm, respectively. Mouse colon wall thickness, as measured by

Brückner *et al* is 0.3 mm (± 0.03) [219]. This means that a µUS wavelength of 0.04 mm spans 13% and 0.02 mm spans 6.7% of a mouse bowel wall. These relatively large wavelengths may have been of insufficient resolution and may explain why minute low grade lesions could not be detected.

The primary endpoint of this study was to directly detect acute inflammation via the infiltration and accumulation of monocytes and neutrophils. Nevertheless, other signs, such as wall thickening, and fold shortening, of inflammation were observed. These observations were not formally collected given their non-specificity. However, this does not rule out their use as an adjunct to diagnosis. Radiometric measurements have the potential provide additional diagnostic information and can be applied to µUS scans. However, these metrics may not account for residual disease activity, such as acute inflammatory cells in the superficial layers, that direct tissue imaging would theoretically permit. As introduced in Chapter 1, it is this approach that can potentially achieve a therapeutic endpoint of complete remission.

6.6. Summary and Conclusion

This chapter described the results of mouse GI inflammatory experiments. The first objective of determining whether µUS could detect GI inflammation was achieved. The results showed that high grade transmural inflammation was detected by a 37 MHz transducer. Further experiments indicated that mild to moderate inflammation could not be detected with either 37 or 62 MHz transducers. Improved alignment between µUS and histology could help with cross modality comparisons. Nevertheless, the detection of low-grade inflammation may be beyond the capabilities of the two frequencies used in this series of experiments.

Chapter 7. Conclusion

7. Chapter Introduction

This chapter discusses the main findings from each chapter as they relate to ultrasound capsule endoscopy (USCE) and the diagnosis and management of gastrointestinal (GI) disorders. Potential avenues of future research are also discussed.

7.1. Crohn's Disease and Capsule Endoscopy

Crohn's disease (CD) is an inflammatory bowel disease (IBD) of the GI tract. It is chronic, progressive and marked by intermittent periods of remission and relapse. The disease can affect any part of the gastrointestinal (GI) tract [1].

The prevalence of IBD is estimated at ≈ 0.3% of the population in the UK and another 1.45 cases per 100,000 persons will be added per year [220]. Roughly a third of the newly diagnosed will be under the age of 21 [221]. Despite the illness, patients with CD do not appear to have a significantly elevated mortality rate over the general population [222]. Additionally, patients can experience numerous diagnostic tests including endoscopic examination throughout their lives [223].

Capsule endoscopy (CE) has emerged as a valuable means of GI examination. Benefits of CE include entire GI tract visualisation, non-invasive administration and good tolerance by patients [19]. Due to its benefits, CE is well suited for diagnosis and monitoring in IBD, including treatment responses [5]. The latter benefit becomes more salient when considering that premature discontinuation of treatment results in residual disease, particularly in remote bowel sections. This illustrates the need for whole bowel assessment to guide therapy in order to achieve a complete response [224].

Currently, CE is not considered a frontline examination due to a number of limitations including the reliance on optical imaging. Optical cameras cannot perform transmural cross-sectional imaging nor provide subsurface pathological information. By equipping CEs with a means to image subsurface pathology, clinicians could examine the subsurface components of the GI tract in its entirety. This has the potential to move beyond using mucosal healing as a therapeutic endpoint and aim at achieving complete histological remission [12], [225].

Ultrasound CE (USCE) is a potential means of transmural imaging [64]. Furthermore, high resolution microultrasound (µUS) has the potential to guide treatment and achieve histological remission by means of virtual biopsy [226]. As shown by Fatehullah *et al.*, µUS can detect premalignant changes in mutant adenomatous polyposis coli ($Apc^{Min/+}$) mouse small bowel before the onset of optically detectable changes [63]. Based on these results, it can be reasonably inferred that µUS may be capable of detecting the massive convergence of immune cells that accompanies acute inflammation.

My research examined a number of facets associated with the development of USCE. This work was done in order to fulfil a clinical need for an improved means of diagnosis and management of CD.

7.2. Results Discussion

The following section summarises key findings obtained using human, mice and pig tissue, and how these findings advances the development of USCE.

7.2.1. Human

Results for the human tissue scans indicated that ≈ 35 MHz is an acceptable frequency range for human tissue and inclusion into USCE. Frequencies near 35 MHz provided an acceptable balance between depth of tissue penetration and detail. Scans from Case 1 illustrated the enhanced imaging capabilities of µUS over the standard 7 – 12 MHz clinically used frequencies. At 34 MHz the number of acoustic layers increased to 9 layers from the 5 layers visualised with standard frequencies. Of particular interest was the increased level of detail of mucosa.

At standard frequencies, there are only two distinguishable acoustic layers generated by the mucosa [55]. At $\geq$ 35 MHz there are four layers generated by the mucosa. These include the lamina propria (LP), a major immune effector site, represented by the 2nd and 3rd acoustic layers. The muscularis mucosae (Mm) is represented the 3rd and 4th signals [227]. This indicates that µUS frequencies have the potential to detect inflammatory changes in the mucosal LP. For example, Nylund *et al* detected a thickened Mm in CD patients which is not normally ultrasonically visible [228]. Additionally, they were able to visualise a hypoechoic lymphocyte aggregate at the level of the muscularis propria at

10 MHz. These results are consistent with the hypothesis that ≈ 35 MHz has the potential to detect changes associated with inflammation in human GI tissue.

Although only lightly touched upon, comparing µUS results with histology indicated that further work is required. This would help with understanding the relationship between acoustic layers and histologic layers [57]. In addition, scanning tissue in the standard mucosal to serosal manner, other orientations were to be a viable means of tissue imaging. In fact, scanning each tissue layer independently at 90° to the transducer represents a novel technique. This may assist in determining how the composition of each layer contributes to µUS image formation.

Further research into the acoustic-histologic relationship would also help advance concepts in virtual histology. This is especially pertinent, as it was apparent that µUS showed wide morphologic and organisational variation between cases. Reasons for the differences between samples were unknown but may have been due to primary disease, comorbidities, age or other factors [210], [211], [229], [230]. Results from Chapter 4 strongly suggest that a more rigorous comparison of human µUS and histology is warranted.

Results for the human tissue scanning have indicated that µUS is capable of displaying tissue with a high degree of detail. This would indicate that high resolution USCE has the potential to provide a means of analysing tissue and associated pathology *in situ* [64], [231]. In order to do so effectively, it will be necessary to correlate µUS signals with histology definitively. Tissue analysis is critical in medical decision making and any new means of analysis must be consistent with histology, the current gold standard.

7.2.2. Pig

Results from both experimental prototype capsules demonstrated that USCE is feasible. Sufficient contact occurred between capsule transducers and mucosa to produce a transmural bowel image.

Future work should centre on developing an improved µUS array for inclusion into the capsule. Required improvements need to adjust transducer focus to account for depth of regions of interest [206]. For effective imaging of acute inflammation, a transducer focused at relatively shallow depths is required. This is because the LP, the primary immune effector site, lies close to the surface. Also required is a 360° cross-sectional

image of the bowel wall to improve USCE diagnostic yield over multiple single element transducers. A ring shaped annular transducer has been suggested as a possible configuration to meet this requirement (Figure 7.1) [232]. Based on the results from the human tissue trial such a transducer should use a centre frequency of 35 MHz.

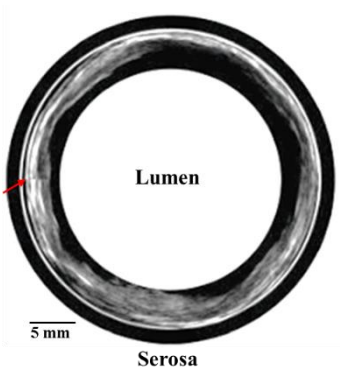

Figure 7.1. Simulated annular image of *ex vivo* pig small bowel. The image was processed to form a circular image from a flat image. The image was stitched (red arrow) to simulate a single slice transmural ultrasound capsule endoscope view. Image adapted from Lay *et al* [232].

Further pre-clinical development could continue to use pigs as they represent a practical large animal model for GI biomedical research [233], [234]. As a monogastric and omnivorous animal, the pig shares a high degree of anatomical and physiologic similarity with humans. Most importantly, the calibre of the bowel lumen and bowel wall thickness are comparable to humans (Figure 7.2) [235].

The similarity in bowel dimensions will permit the use of full scale USCE prototypes, like those demonstrated here. Similar bowel dimensions would eliminate the need to scale the dimensions of the capsule shell (i.e. 10 mm Ø x 30 mm L). Furthermore, similar bowel wall thickness would permit direct assessment of the capsule µUS frequency because µUS wavelengths correspond well between the two species, unlike mouse bowel dimensions.

Pig models of human disease are available including models of IBD based on the use of DSS and precancerous conditions such as Familial Adenomatous Polyposis (FAP) pigs [233], [236], [237].

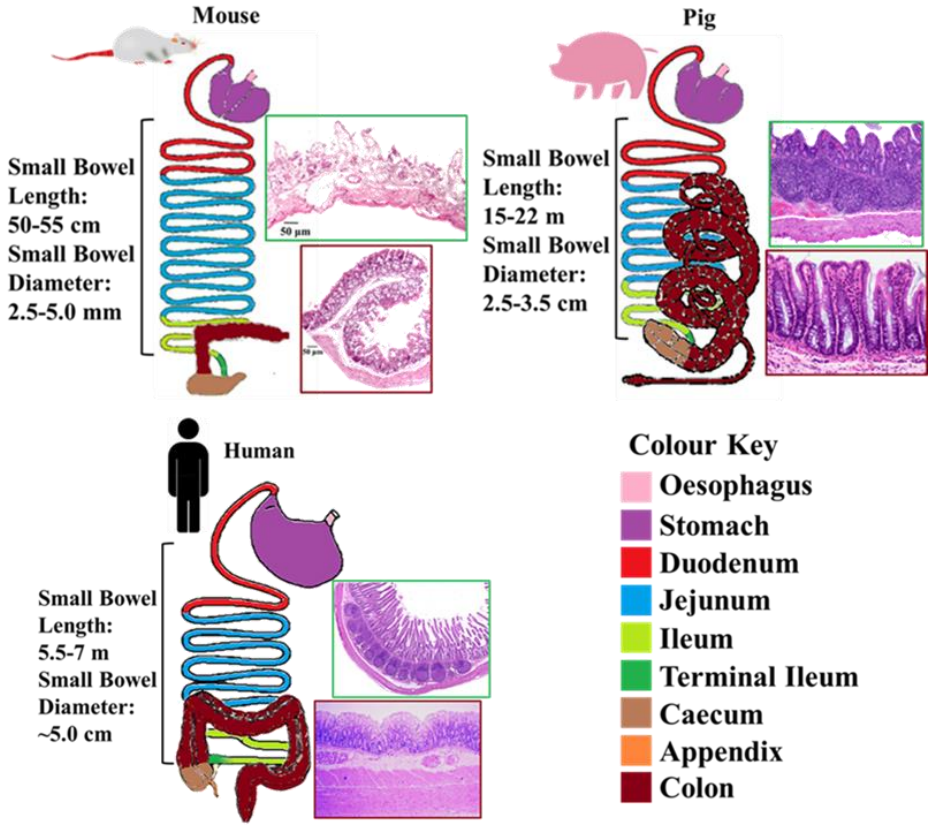

Figure 7.2. Comparitive anatomy and histology of the three organisms used for experiments. All three systems have similar gross anatomical structure from oesophagus to rectum. Interspecies differences can be noted such as the relatively large caecum of the mouse. Although humans and pigs are monogastric and omnivourous; colonic structures differ signigicantly including the characteristic spiral colon of the pig. In terms of gross measurments, pigs and humans exhibit similar bowel diameters and wall thickness that is not shared by the mouse. Microscopically, all three share the same four cardinal bowel layers (mucosa, submucosa, muscularis propria and serosa). Image adapted from T. Kararli [235].

7.2.3. Mouse

The results from the inflammatory mouse bowel experiments indicate that µUS can detect high grade inflammation. Lower grade inflammation, which would equate to early onset or post-treatment residual IBD, was not detectable. It is possible that the frequencies used were an inappropriate scale for the thickness of mouse bowel. Evidence for this argument is the number of acoustic layers revealed in the scans. At 37 MHz, the maximum number of acoustic layers displayed was limited to 3, which were seen predominately in the colon scans, nor did the number of visible layers increase when the frequency was raised to 62 MHz. This was unlike the results from the human colon experiments where higher frequencies revealed additional acoustic layers over standard frequencies of 5 - 12 MHz.

This suggests that neither 37 nor 62 MHz is suitable for detecting low grade GI inflammation in mice.

Regardless, µUS studies on mouse bowel could be conducted using even higher frequencies. This would help to resolve the potential wavelength to tissue dimension issue, and whether enhanced resolution could identify low grade inflammation. Alternatively, high resolution imaging can be done with Optical Coherence Tomography (OCT).

OCT operates on the same transmit/receive principle as US but uses light to provide high resolution subsurface images (Figure 7.3) [238]. Additionally, OCT has already been incorporated into a tethered capsule endoscope and tested clinically. Gora *et al* developed a OCT capsule to examine the oesophagus and monitor Barrett's Oesophagus [239], [240]. The authors were able to produce highly detailed 3-dimensional images of the oesophagus. Furthermore, OCT represents an attractive modality for facilitating virtual biopsy [241], [242]. This is because it can rapidly produce highly detailed (axial resolution ~10 µm and lateral resolution ~30 µm) volumetric images. The primary drawbacks are the limited depth of tissue penetration, estimated to be 3 mm maximum depending on pressure and probe type [243]. This potentially limits its utility to superficial diseases of the mucosa which includes inflammation and neoplasms of epithelial origin [244].

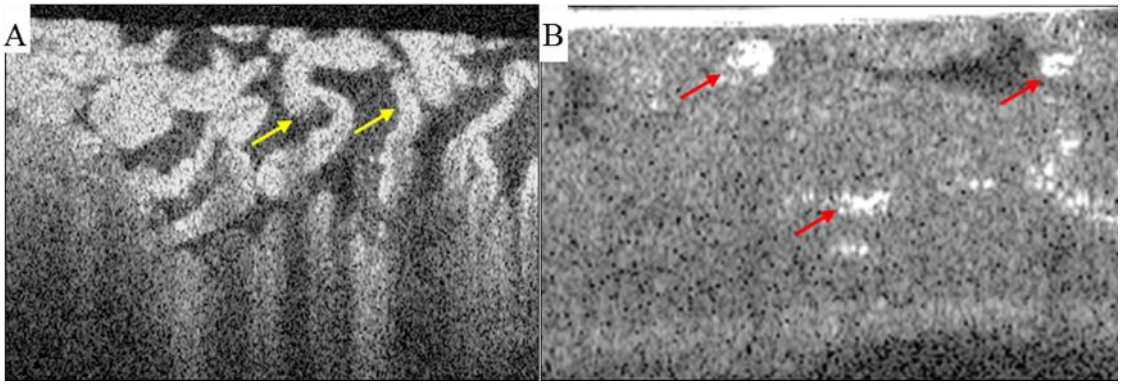

Figure 7.3A-B. Optical Coherence Tomography (OCT) scan of *ex vivo* pig small bowel. (A) Image of a perfused section of small bowel. The level of mucosal detail is clear and individual villi (yellow arrows) can be discerned. Also evident is the limited depth of tissue penetration by the light waves. (B) Image of a bowel section post perfusion with 10 µm diameter polystyrene beads (red arrows). OCT is able to detect the subsurface accumulation of beads. Images created in collaboration in Y. Ling.

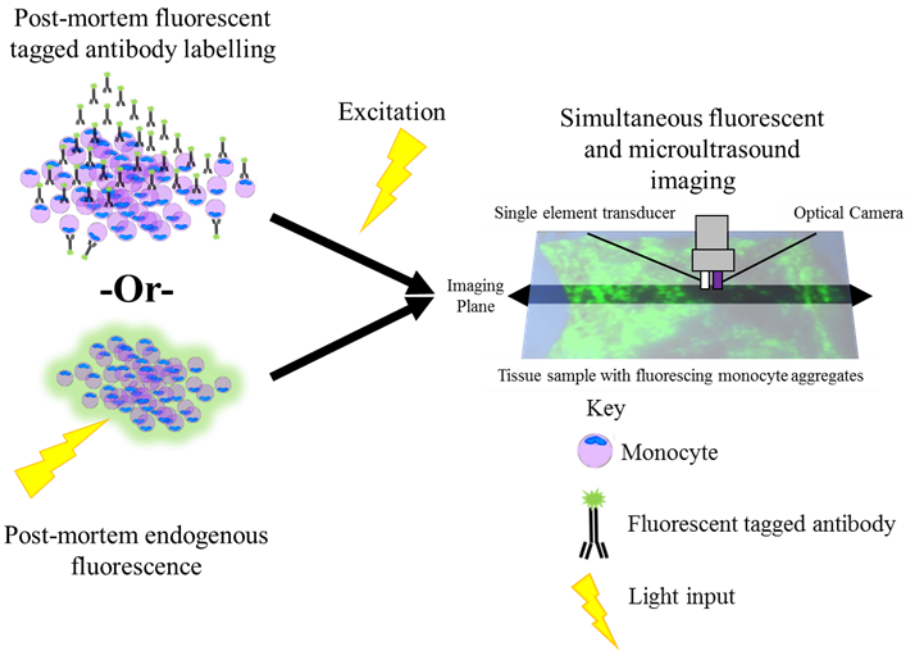

Figure 7.4. Conceptual image of a combined microultrasound (µUS) and optical fluorescent modality scanner. Fluorescent imaging could provide an optical means to detect inflammatory cell accumulation. Post-mortem monocyte fluorescence could be achieved by either labelling with fluorescent tagged antibodies or inducing endogenous molecules to fluoresce. Fluorescing leukocytes would permit optical visualisation of inflammation in conjunction with µUS scanning. This would assist with categorising anomalous µUS signals as being created accumulated inflammatory cells. Image adapted from Cox *et al* [245].

As discussed in Chapter 6, there was difficulty aligning scan results with corresponding histology slices. Simultaneous optical and µUS imaging of the tissue may be a potential means of resolving this problem. Optical images in the same plane as the µUS images would provide a means of eliminating anomalous signals due to non-inflammatory sources such as debris. However, low grade inflammation did not result in overt optical signs. Therefore, a means of detecting accumulation of inflammatory cells would also be necessary. As leukocytes can be made to fluoresce through artificial or endogenous means, it offers a possible means of complimentary inflammatory imaging. Post-mortem tissue can be labelled with fluorescent antibodies or made to fluoresce via endogenous molecules [246], [247]. By employing fluorescent imaging, it may be possible to detect monocyte aggregation at lower inflammatory grades. Simultaneous µUS and optical fluorescent imaging would enable direct comparison between the two modalities and improve interpretation of anomalous US signals as illustrated in figure 7.4.

7.3. Related µUS Future Work

As introduced in Chapter 2, the GI tract comprises a relatively massive area in which to examine at high resolution levels. The surface area of the human GI tract is measured in square meters while µUS wavelengths are sub-mm in scale. As it stands, standard optical CE interpretation times are considered lengthy and automated detection of pathology is absolutely needed [248]. The addition of a second imaging modality, namely µUS, would substantially increase the number of images requiring review. An automated means of diagnosis is, therefore, essential to manage both data volume and interpretation times.

Preliminary work focused on image processing and data analysis has been done [249] exploring machine learning to develop computer assisted diagnosis (CADx). Early results have yet to be validated but have shown potential promise in distinguishing healthy tissue from inflamed [250].

7.4. Summary and Conclusion

The principal motivation driving this research was to improve the diagnosis and management of IBD and GI disorders in general. The route taken involved the design and development of USCE. Such a device could transit the entire GI tract and provide high resolution transmural µUS images to gain subsurface information on pathology. This, in turn, would enhance the ability to accurately monitor disease activity and improve treatment capabilities. Clinicians could be provided a means to achieve complete histological remission without the need for tissue biopsy.

My research into USCE used three species to test different aspect of USCE design and function. Human tissue results indicated that a centre frequency of ≈35 MHz could provide satisfactory high resolution transmural images. *In vivo* pig experiments successfully demonstrated USCE could generate cross-sectional bowel images. Inflammation experiments using mice showed that frequencies appropriate for human bowel dimensions could detect high grade inflammation in mice.

USCE has the potential to positively impact the diagnosis and management of IBD and other GI disorders [251]. My work has successfully demonstrated the feasibility and potential of USCE. The results of this endeavour have provided the foundation and impetus for continued research in this much needed area.

Bibliography

[1] R. G. Farmer, W. A. Hawk, and R. B. Turnbull, “Clinical patterns in Crohn’s disease: a statistical study of 615 cases.,” *Gastroenterology*, vol. 68, no. 4 Pt 1, pp. 627–35, Apr. 1975.

[2] R. J. Xavier and D. K. Podolsky, “Unravelling the pathogenesis of inflammatory bowel disease.,” *Nature*, vol. 448, no. 7152, pp. 427–34, Jul. 2007.

[3] M. Gajendran, P. Loganathan, A. P. Catinella, and J. G. Hashash, “A comprehensive review and update on Crohn’s disease.,” *Dis. Mon.*, vol. 64, no. 2, pp. 20–57, Feb. 2018.

[4] W. R. Best, J. M. Becktel, J. W. Singleton, and F. Kern, “Development of a Crohn’s disease activity index. National Cooperative Crohn’s Disease Study.,” *Gastroenterology*, vol. 70, no. 3, pp. 439–44, Mar. 1976.

[5] G. R. Lichtenstein, E. V Loftus, K. L. Isaacs, M. D. Regueiro, L. B. Gerson, and B. E. Sands, “ACG Clinical Guideline: Management of Crohn’s Disease in Adults.,” *Am. J. Gastroenterol.*, vol. 113, no. 4, pp. 481–517, Apr. 2018.

[6] M. Dave and E. V Loftus, “Mucosal healing in inflammatory bowel disease-a true paradigm of success?,” *Gastroenterol. Hepatol. (N. Y).*, vol. 8, no. 1, pp. 29–38, Jan. 2012.

[7] J. Y. Mary and R. Modigliani, “Development and validation of an endoscopic index of the severity for Crohn’s disease: a prospective multicentre study. Groupe d’Etudes Thérapeutiques des Affections Inflammatoires du Tube Digestif (GETAID).,” *Gut*, vol. 30, no. 7, pp. 983–9, Jul. 1989.

[8] B. P. Vaughn, S. Shah, and A. S. Cheifetz, “The role of mucosal healing in the treatment of patients with inflammatory bowel disease.,” *Curr. Treat. Options Gastroenterol.*, vol. 12, no. 1, pp. 103–17, Mar. 2014.

[9] C. Zallot and L. Peyrin-Biroulet, “Deep remission in inflammatory bowel disease: looking beyond symptoms.,” *Curr. Gastroenterol. Rep.*, vol. 15, no. 3, p. 315, Mar. 2013.

[10] R. K. Pai and K. Geboes, “Disease activity and mucosal healing in inflammatory bowel disease: a new role for histopathology?,” *Virchows Arch.*, vol. 472, no. 1,

pp. 99–110, Jan. 2018.

[11] R. V Bryant, S. Winer, S. P. L. Travis, and R. H. Riddell, “Systematic review: histological remission in inflammatory bowel disease. Is ‘complete’ remission the new treatment paradigm? An IOIBD initiative.,” *J. Crohns. Colitis*, vol. 8, no. 12, pp. 1582–97, Dec. 2014.

[12] V. Villanacci, E. Antonelli, K. Geboes, G. Casella, and G. Bassotti, “Histological healing in inflammatory bowel disease: a still unfulfilled promise.,” *World J. Gastroenterol.*, vol. 19, no. 7, pp. 968–78, Feb. 2013.

[13] K. Geboes and I. Dalle, “Influence of treatment on morphological features of mucosal inflammation.,” *Gut*, vol. 50 Suppl 3, no. Cd, pp. III37-I42, 2002.

[14] F. Magro *et al.*, “European consensus on the histopathology of inflammatory bowel disease.,” *J. Crohns. Colitis*, vol. 7, no. 10, pp. 827–51, Nov. 2013.

[15] P. Molander *et al.*, “Achievement of deep remission during scheduled maintenance therapy with TNFα-blocking agents in IBD.,” *J. Crohns. Colitis*, vol. 7, no. 9, pp. 730–5, Oct. 2013.

[16] B. I. Korelitz and S. C. Sommers, “Response to drug therapy in Crohn’s disease: evaluation by rectal biopsy and mucosal cell counts.,” *J. Clin. Gastroenterol.*, vol. 6, no. 2, pp. 123–7, Apr. 1984.

[17] A. Kakkar, S. K. Wasan, and F. A. Farraye, “Targeting mucosal healing in crohn’s disease,” *Gastroenterol. Hepatol.*, vol. 7, no. 6, pp. 374–380, 2011.

[18] G. Iddan, G. Meron, A. Glukhovsky, and P. Swain, “Wireless capsule endoscopy.,” *Nature*, vol. 405, no. 6785, p. 417, May 2000.

[19] H. Ojidu *et al.*, “Patient tolerance and acceptance of different colonic imaging modalities: an observational cohort study.,” *Eur. J. Gastroenterol. Hepatol.*, vol. 30, no. 5, pp. 520–525, May 2018.

[20] H. J. Song and K. Shim, “Current status and future perspectives of capsule endoscopy,” *Intest. Res.*, vol. 14, no. 1, p. 21, 2016.

[21] ASGE, “Capsule Endoscopy,” *American Society for Gastrointestinal Endoscopy*, 2014. [Online]. Available: https://www.asge.org/home/about-asge/newsroom/media-backgrounders-detail/wireless-capsule-endoscopy. [Accessed: 01-Nov-2018].

[22] R. Koprowski, “Overview of technical solutions and assessment of clinical usefulness of capsule endoscopy.,” *Biomed. Eng. Online*, vol. 14, no. 1, p. 111, 2015.

[23] K. Nakamura, “Further Development of Endoscopic Imaging: ‘Era of Light’ Activities with Optics and Image Processing Technology,” in *New Challenges in Gastrointestinal Endoscopy*, H. Niwa, H. Tajiri, M. Nakajima, and K. Yasuda, Eds. Tokyo: Springer Japan, 2008, pp. 40–54.

[24] T. D. Wang and J. Van Dam, “Optical biopsy: a new frontier in endoscopic detection and diagnosis.,” *Clin. Gastroenterol. Hepatol.*, vol. 2, no. 9, pp. 744–53, Sep. 2004.

[25] E. J. Ciaccio, G. Bhagat, S. K. Lewis, and P. H. Green, “Suggestions for automatic quantitation of endoscopic image analysis to improve detection of small intestinal pathology in celiac disease patients,” *Comput. Biol. Med.*, vol. 65, pp. 364–368, Oct. 2015.

[26] B. C. Dickson, C. J. Streutker, and R. Chetty, “Coeliac disease: an update for pathologists.,” *J. Clin. Pathol.*, vol. 59, no. 10, pp. 1008–16, 2006.

[27] T. Kav and B. Sivri, “Is enteroscopy necessary for diagnosis of celiac disease?,” *World J. Gastroenterol.*, vol. 18, no. 31, pp. 4095–101, Aug. 2012.

[28] A. Wang *et al.*, “Wireless capsule endoscopy.,” *Gastrointest. Endosc.*, vol. 78, no. 6, pp. 805–15, Dec. 2013.

[29] G. Cummins *et al.*, “Non-optical capsule based gastrointestinal diagnosis,” 2018.

[30] K. T. Dussik, “Über die Möglichkeit, hochfrequente mechanische Schwingungen als diagnostisches Hilfsmittel zu verwerten,” *Zeitschrift für die gesamte Neurol. und Psychiatr.*, vol. 174, no. 1, pp. 153–168, Dec. 1942.

[31] G. D. Ludwig and F. . Struthers, “Considerations underlying the use of Ultrasound to detect Gallstones and Foregn Bodies in Tissue,” Naval Medical Research Institute Reports, Project #004 001, Report No. 4, 1949.

[32] I. DONALD, J. MACVICAR, and T. G. BROWN, “Investigation of abdominal masses by pulsed ultrasound.,” *Lancet (London, England)*, vol. 1, no. 7032, pp. 1188–95, Jun. 1958.

[33] E. P. DiMagno and M. J. DiMagno, “Endoscopic Ultrasonography: From the

Origins to Routine EUS," *Dig. Dis. Sci.*, vol. 61, no. 2, pp. 342–353, 2016.

[34] S. Cochran, M. P. Y. Desmulliez, R. J. C. Steele, A. Cuschieri, and D. R. S. Cumming, "Sonopill: Minimally Invasive Gastrointestinal Diagnosis and Therapy, Case for Support," 2012.

[35] D. Lieu, "Ultrasound physics and instrumentation for pathologists.," *Arch. Pathol. Lab. Med.*, vol. 134, no. 10, pp. 1541–56, Oct. 2010.

[36] S. Ødegaard, L. B. Nesje, O. D. Lærum, and M. B. Kimmey, "High-frequency ultrasonographic imaging of the gastrointestinal wall.," *Expert Rev. Med. Devices*, vol. 9, no. 3, pp. 263–73, May 2012.

[37] S. K. Edelman, *Understanding Ultrasound Physics*, 4th ed. E.S.P. Ultrasound, 2012.

[38] J. Méndez and A. Keys, "Density and composition of mammalian muscle," *Metabolism*, vol. 9, pp. 184–188, 1960.

[39] M. S. Farvid, T. W. K. Ng, D. C. Chan, P. H. R. Barrett, and G. F. Watts, "Association of adiponectin and resistin with adipose tissue compartments, insulin resistance and dyslipidaemia.," *Diabetes. Obes. Metab.*, vol. 7, no. 4, pp. 406–13, Jul. 2005.

[40] J. E. Aldrich, "Basic physics of ultrasound imaging.," *Crit. Care Med.*, vol. 35, no. 5 Suppl, pp. S131-7, May 2007.

[41] J. Mamou and M. Oelze, *Quantitative Ultrasound in Soft Tissues*. Dordrecht: Springer Netherlands, 2013.

[42] "Reflection, Refraction, Scattering and Attenuation," *VAULT- Regional Anesthesia + Vascular Access Training*, 2017. [Online]. Available: https://www.vaultrasound.com/educational-resources/ultrasound-physics/reflection-refraction/. [Accessed: 08-Nov-2018].

[43] N. J. Hangiandreou, "AAPM/RSNA physics tutorial for residents. Topics in US: B-mode US: basic concepts and new technology.," *Radiographics*, vol. 23, no. 4, pp. 1019–33, 2005.

[44] N. M. Tole, "Basic physics of ultrasonographic imaging," *Diagnostic Imaging Lab. Technol. Essent. Heal. Technol. Heal. Technol. Pharm. WORLD Heal. Organ. Geneva*, p. 95, 2005.

[45] O. V Michailovich and A. Tannenbaum, “Despeckling of medical ultrasound images.,” *IEEE Trans. Ultrason. Ferroelectr. Freq. Control*, vol. 53, no. 1, pp. 64–78, Jan. 2006.

[46] K. K. Shung, *Ultrasonic Scattering in Biological Tissues*, 1st ed. CRC Press, 1992.

[47] M. A. Morgan and M. M. Nadrljanski, “Ultrasound frequencies,” *Radiopaedia*. .

[48] T. Anbarasan *et al.*, “High Resolution Microultrasound (μUS) Investigation of the Gastrointestinal (GI) Tract.,” *Methods Mol. Biol.*, vol. 1572, no. 1, pp. 541–561, Mar. 2017.

[49] A. May *et al.*, “Accuracy of staging in early oesophageal cancer using high resolution endoscopy and high resolution endosonography: a comparative, prospective, and blinded trial.,” *Gut*, vol. 53, no. 5, pp. 634–40, May 2004.

[50] T. Krill *et al.*, “Accuracy of endoscopic ultrasound in esophageal cancer staging,” *J. Thorac. Dis.*, vol. 11, no. S12, pp. S1602–S1609, Aug. 2019.

[51] F. S. Foster, C. J. Pavlin, K. A. Harasiewicz, D. A. Christopher, and D. H. Turnbull, “Advances in ultrasound biomicroscopy.,” *Ultrasound Med. Biol.*, vol. 26, no. 1, pp. 1–27, Jan. 2000.

[52] R. H. Silverman, “High-resolution ultrasound imaging of the eye - A review,” *Clin. Exp. Ophthalmol.*, vol. 37, no. 1, pp. 54–67, 2009.

[53] J. Beaulieu, R. Vlad, and L. Taggart, “High-frequency ultrasound characterization of microcellular components,” in *Proceedings of the 10th Congress of the World Federation for Ultrasound in Medicine and Biology*, 2002.

[54] G. Czarnota, “Czarnota GJ. Ultrasound imaging of apoptosis in vivo: Effects of subcellular nuclear morphology and cell membrane morphology,” in *Proceedings of the 10th Congress of the World Federation for Ultrasound in Medicine and Biology*, 2002.

[55] P. R. McNally, “Endoscopic Ultrasound,” in *GI/Liver Secrets*, Fourth., P. R. McNally, Ed. Elsevier, 2010, pp. 537–544.

[56] M. B. Kimmey, R. W. Martin, R. C. Haggitt, K. Y. Wang, D. W. Franklin, and F. E. Silverstein, “Histologic correlates of gastrointestinal ultrasound images,”

Gastroenterology, vol. 96, no. 2 PART 1, pp. 433–441, 1989.

[57] A. B. Le Roux, L. A. Granger, N. Wakamatsu, M. T. Kearney, and L. Gaschen, "Ex Vivo Correlation of Ultrasonographic Small Intestinal Wall Layering with Histology in Dogs," *Vet. Radiol. Ultrasound*, p. n/a-n/a, Jun. 2016.

[58] T. Aibe, T. Fuji, K. Okita, and T. Takemoto, "A Fundamental Study of Normal Layer Structure of the Gastrointestinal Wall Visualized by Endoscopic Ultrasonography," *Scand. J. Gastroenterol.*, vol. 21, no. sup123, pp. 6–15, Jan. 1986.

[59] N. Heyder, H. Kaarmann, and J. Giedl, "Experimental Investigations into the Possibility of Differentiating Early from Invasive Carcinoma of the Stomach by Means of Ultrasound," *Endoscopy*, vol. 19, no. 06, pp. 228–232, Nov. 1987.

[60] J. Yoshino *et al.*, "Gastric Wall Structure Using a 30 MHz Endoscopic Ultrasound Probe, Focusing upon Delineation of the Muscularis Mucosae," *Dig. Endosc.*, vol. 12, no. 3, pp. 233–236, Jul. 2000.

[61] M. J. Wiersema and L. M. Wiersema, "ultrasonography of the gastrointestinal wall : histologic correlates," *Gastrointest. Endosc.*, pp. 499–504, 1993.

[62] "Pathology," *Merriam-Webster, Incorporated*, 2018. [Online]. Available: https://www.merriam-webster.com/dictionary/pathology. [Accessed: 13-Nov-2018].

[63] A. Fatehullah *et al.*, "Increased variability in ApcMin/+ intestinal tissue can be measured with microultrasound," *Sci. Rep.*, vol. 6, no. July, p. 29570, Jul. 2016.

[64] B. F. Cox *et al.*, "Ultrasound capsule endoscopy: sounding out the future," *Ann. Transl. Med.*, vol. 5, no. 9, pp. 201–201, May 2017.

[65] N. M. Fried and A. L. Burnett, "Novel methods for mapping the cavernous nerves during radical prostatectomy," *Nat. Rev. Urol.*, vol. 12, no. 8, pp. 451–460, Aug. 2015.

[66] H. F. Helander and L. Fändriks, "Surface area of the digestive tract - revisited.," *Scand. J. Gastroenterol.*, vol. 49, no. 6, pp. 681–9, Jun. 2014.

[67] G. Hounnou, C. Destrieux, J. Desmé, P. Bertrand, and S. Velut, "Anatomical study of the length of the human intestine.," *Surg. Radiol. Anat.*, vol. 24, no. 5, pp. 290–4, Dec. 2002.

[68] F. Diep, “Human Gut Has The Surface Area Of A Studio Apartment,” *Popular Science*, 2014.

[69] D. Pascual, H. Kiyono, and J. McGhee, *Enteric Infections and Immunity*. Springer, 2014.

[70] L. C. Junqueira and J. Carneiro, *Junqueira’s Basic Histology: Text and Atlas*, 10th ed. McGraw-Hill, 2002.

[71] P. Kvietys, *The Gastrointestinal Circulation*. San Rafael (CA): Morgan & Claypool Life Sciences, 2010.

[72] A. S. Darwich, U. Aslam, D. M. Ashcroft, and A. Rostami-Hodjegan, “Meta-analysis of the turnover of intestinal epithelia in preclinical animal species and humans.,” *Drug Metab. Dispos.*, vol. 42, no. 12, pp. 2016–22, Dec. 2014.

[73] W. S. Garrett, J. I. Gordon, and L. H. Glimcher, “Homeostasis and inflammation in the intestine.,” *Cell*, vol. 140, no. 6, pp. 859–70, Mar. 2010.

[74] J. König *et al.*, “Human Intestinal Barrier Function in Health and Disease.,” *Clin. Transl. Gastroenterol.*, vol. 7, no. 10, p. e196, Oct. 2016.

[75] V. Snoeck, B. Goddeeris, and E. Cox, “The role of enterocytes in the intestinal barrier function and antigen uptake.,” *Microbes Infect.*, vol. 7, no. 7–8, pp. 997–1004, Jun. 2005.

[76] R. D. Specian and M. G. Oliver, “Functional biology of intestinal goblet cells.,” *Am. J. Physiol.*, vol. 260, no. 2 Pt 1, pp. C183-93, Feb. 1991.

[77] N. Miron and V. Cristea, “Enterocytes: active cells in tolerance to food and microbial antigens in the gut.,” *Clin. Exp. Immunol.*, vol. 167, no. 3, pp. 405–12, Mar. 2012.

[78] S. C. Corr, C. C. G. M. Gahan, and C. Hill, “M-cells: origin, morphology and role in mucosal immunity and microbial pathogenesis,” *FEMS Immunol. Med. Microbiol.*, vol. 52, no. 1, pp. 2–12, Jan. 2008.

[79] J. P. Kraehenbuhl and M. R. Neutra, “Molecular and cellular basis of immune protection of mucosal surfaces.,” *Physiol. Rev.*, vol. 72, no. 4, pp. 853–79, Oct. 1992.

[80] H. Ohno, “Intestinal M cells.,” *J. Biochem.*, vol. 159, no. 2, pp. 151–60, Feb. 2016.

[81] M. Karlsson, S. Lundin, U. Dahlgren, H. Kahu, I. Pettersson, and E. Telemo, “‘Tolerosomes’ are produced by intestinal epithelial cells.,” *Eur. J. Immunol.*, vol. 31, no. 10, pp. 2892–900, Oct. 2001.

[82] V. Snoeck, I. R. Peters, and E. Cox, “The IgA system: A comparison of structure and function in different species,” *Vet. Res.*, vol. 37, no. 3, pp. 455–467, May 2006.

[83] P. Brandtzaeg, H. S. Carlsen, and T. S. Halstensen, “The B-Cell System in Inflammatory Bowel Disease,” 2006, pp. 149–167.

[84] and M. J. S. Charles A Janeway, Jr, Paul Travers, Mark Walport, *Immunobiology, 5th edition*, 5th ed. New York, NY: Garland Science, 2001.

[85] F.-E. Johansen, R. Massol, K. Baker, E. Fiebiger, R. S. Blumberg, and W. I. Lencer, “Biology of Gut Immunoglobulins,” in *Physiology of the Gastrointestinal Tract*, Elsevier, 2012, pp. 1089–1118.

[86] P. Brandtzaeg, I. N. Farstad, F. E. Johansen, H. C. Morton, I. N. Norderhaug, and T. Yamanaka, “The B-cell system of human mucosae and exocrine glands.,” *Immunol. Rev.*, vol. 171, no. 1, pp. 45–87, Oct. 1999.

[87] M. Schenk and C. Mueller, “The mucosal immune system at the gastrointestinal barrier,” *Best Pract. Res. Clin. Gastroenterol.*, vol. 22, no. 3, pp. 391–409, Jun. 2008.

[88] P. Brandtzaeg *et al.*, “Immunobiology and immunopathology of human gut mucosa: humoral immunity and intraepithelial lymphocytes.,” *Gastroenterology*, vol. 97, no. 6, pp. 1562–84, Dec. 1989.

[89] M. L. Forchielli and W. A. Walker, “The role of gut-associated lymphoid tissues and mucosal defence,” *Br. J. Nutr.*, vol. 93, no. S1, p. S41, 2005.

[90] A. Hakansson and G. Molin, “Gut Microbiota and Inflammation,” *Nutrients*, vol. 3, no. 12, pp. 637–682, Jun. 2011.

[91] R. D. Newberry and R. G. Lorenz, “Organizing a mucosal defense,” *Immunol. Rev.*, vol. 206, pp. 6–21, 2005.

[92] J. R. McGhee and K. Fujihashi, “Inside the mucosal immune system.,” *PLoS Biol.*, vol. 10, no. 9, p. e1001397, 2012.

[93] R. van Furth, “THE ORIGIN AND KINETICS OF MONONUCLEAR PHAGOCYTES,” *J. Exp. Med.*, vol. 128, no. 3, pp. 415–435, Sep. 1968.

[94] M. Salmi and S. Jalkanen, “Molecules controlling lymphocyte migration to the gut,” *Gut*, vol. 45, no. 1, pp. 148–153, 1999.

[95] C. D. Braden, “Neutropenia,” *Medscape*, 2018. .

[96] P. Tyrer, A. R. Foxwell, A. W. Cripps, M. A. Apicella, and J. M. Kyd, “Microbial pattern recognition receptors mediate M-cell uptake of a gram-negative bacterium.,” *Infect. Immun.*, vol. 74, no. 1, pp. 625–31, Jan. 2006.

[97] R. Zaru, “Pattern recognition receptors,” *British Society for Immunology*, 2018. [Online]. Available: https://www.immunology.org/public-information/bitesized-immunology/receptors-and-molecules/pattern-recognition-receptors. [Accessed: 31-Aug-2018].

[98] O. Takeuchi and S. Akira, “Pattern recognition receptors and inflammation.,” *Cell*, vol. 140, no. 6, pp. 805–20, Mar. 2010.

[99] L. Schaefer, “Complexity of danger: the diverse nature of damage-associated molecular patterns.,” *J. Biol. Chem.*, vol. 289, no. 51, pp. 35237–45, Dec. 2014.

[100] K. Newton and V. M. Dixit, “Signaling in innate immunity and inflammation.,” *Cold Spring Harb. Perspect. Biol.*, vol. 4, no. 3, Mar. 2012.

[101] S. Gordon, A. Plüddemann, and F. Martinez Estrada, “Macrophage heterogeneity in tissues: phenotypic diversity and functions.,” *Immunol. Rev.*, vol. 262, no. 1, pp. 36–55, Nov. 2014.

[102] C. C. Bain and A. M. Mowat, “The monocyte-macrophage axis in the intestine.,” *Cell. Immunol.*, vol. 291, no. 1–2, pp. 41–8, 2014.

[103] D. A. Hume, V. H. Perry, and S. Gordon, “The mononuclear phagocyte system of the mouse defined by immunohistochemical localisation of antigen F4/80: Macrophages associated with epithelia,” *Anat. Rec.*, vol. 210, no. 3, pp. 503–512, Nov. 1984.

[104] A. Geremia, P. Biancheri, P. Allan, G. R. Corazza, and A. Di Sabatino, “Innate and adaptive immunity in inflammatory bowel disease.,” *Autoimmun. Rev.*, vol. 13, no. 1, pp. 3–10, Jan. 2014.

[105] “Normal Blood Counts,” *CML Support*, 2015. [Online]. Available: https://www.cmlsupport.org.uk/section/normal-blood-counts. [Accessed: 24-Sep-2018].

[106] C. Summers, S. M. Rankin, A. M. Condliffe, N. Singh, A. M. Peters, and E. R. Chilvers, “Neutrophil kinetics in health and disease.,” *Trends Immunol.*, vol. 31, no. 8, pp. 318–24, Aug. 2010.

[107] S. Bugl, S. Wirths, M. R. Müller, M. P. Radsak, and H.-G. Kopp, “Current insights into neutrophil homeostasis.,” *Ann. N. Y. Acad. Sci.*, vol. 1266, pp. 171–8, Aug. 2012.

[108] R. M. Feakins, “Inflammatory bowel disease biopsies: updated British Society of Gastroenterology reporting guidelines,” *J. Clin. Pathol.*, vol. 66, no. 12, pp. 1005–1026, Dec. 2013.

[109] D. S. Levine and R. C. Haggitt, “Normal histology of the colon.,” *Am. J. Surg. Pathol.*, vol. 13, no. 11, pp. 966–84, Nov. 1989.

[110] J. J. Barcia and N. Reissenweber, “Neutrophil count in the normal appendix and early appendicitis: diagnostic index of real acute inflammation.,” *Ann. Diagn. Pathol.*, vol. 6, no. 6, pp. 352–6, Dec. 2002.

[111] R. Pahwa and I. Jialal, “Chronic Inflammation,” *StatPearls*, 2018. [Online]. Available: https://www.ncbi.nlm.nih.gov/books/NBK493173/. [Accessed: 13-Jul-2018].

[112] V. Kumar, N. Abbas, and F. Abul, *Robbins & Cotran Pathologic Basis of Disease*, 7th ed. Philadelphia: Saunders, 2008.

[113] A. U. Ahmed, “An overview of inflammation: Mechanism and consequences,” *Front. Biol.*, vol. 6, no. 4, pp. 274–281, 2011.

[114] M. B. Witte and A. Barbul, “General principles of wound healing.,” *Surg. Clin. North Am.*, vol. 77, no. 3, pp. 509–28, Jun. 1997.

[115] S. Nourshargh and R. Alon, “Leukocyte Migration into Inflamed Tissues,” *Immunity*, vol. 41, no. 5, pp. 694–707, 2014.

[116] N. D. Kim and A. D. Luster, “The role of tissue resident cells in neutrophil recruitment.,” *Trends Immunol.*, vol. 36, no. 9, pp. 547–55, Sep. 2015.

[117] C. L. Sokol and A. D. Luster, “The chemokine system in innate immunity.,” *Cold Spring Harb. Perspect. Biol.*, vol. 7, no. 5, Jan. 2015.

[118] C. a Kunder, A. L. St John, and S. N. Abraham, “Mast cell modulation of the vascular and lymphatic endothelium,” *Blood*, vol. 118, no. 20, pp. 5383–5393, Nov. 2011.

[119] R. C. Furze and S. M. Rankin, “Neutrophil mobilization and clearance in the bone marrow.,” *Immunology*, vol. 125, no. 3, pp. 281–8, Nov. 2008.

[120] A. Glatman Zaretsky, J. B. Engiles, and C. A. Hunter, “Infection-induced changes in hematopoiesis.,” *J. Immunol.*, vol. 192, no. 1, pp. 27–33, Jan. 2014.

[121] B. M. Fournier and C. A. Parkos, “The role of neutrophils during intestinal inflammation.,” *Mucosal Immunol.*, vol. 5, no. 4, pp. 354–66, Jul. 2012.

[122] T. Lämmermann, “In the eye of the neutrophil swarm-navigation signals that bring neutrophils together in inflamed and infected tissues.,” *J. Leukoc. Biol.*, vol. 100, no. 1, pp. 55–63, 2016.

[123] K. Kienle and T. Lämmermann, “Neutrophil swarming: an essential process of the neutrophil tissue response.,” *Immunol. Rev.*, vol. 273, no. 1, pp. 76–93, 2016.

[124] Y. Li, A. Karlin, J. D. Loike, and S. C. Silverstein, “Determination of the critical concentration of neutrophils required to block bacterial growth in tissues,” *J. Exp. Med.*, vol. 200, no. 5, pp. 613–622, 2004.

[125] M. I. Cybulsky, I. J. Cybulsky, and H. Z. Movat, “Neutropenic responses to intradermal injections of Escherichia coli. Effects on the kinetics of polymorphonuclear leukocyte emigration,” *Am.J.Pathol.*, vol. 124, no. 0002-9440 SB-AIM SB-IM, pp. 1–9, 1986.

[126] J. Parkin and B. Cohen, “An overview of the immune system.,” *Lancet (London, England)*, vol. 357, no. 9270, pp. 1777–89, Jun. 2001.

[127] M. Polonsky, B. Chain, and N. Friedman, “Clonal expansion under the microscope: studying lymphocyte activation and differentiation using live-cell imaging.,” *Immunol. Cell Biol.*, vol. 94, no. 3, pp. 242–9, Mar. 2016.

[128] P. Scapini and M. Cassatella, “Social networking of human neutrophils within the immune system \n,” *Blood*, vol. 124, no. First Edition Paper, pp. 710–720, 2014.

[129] B. Amulic, C. Cazalet, G. L. Hayes, K. D. Metzler, and A. Zychlinsky, “Neutrophil function: from mechanisms to disease.,” *Annu. Rev. Immunol.*, vol. 30, no. 1, pp. 459–89, 2012.

[130] V. Kumar and A. Sharma, “Neutrophils: Cinderella of innate immune system,” *Int. Immunopharmacol.*, vol. 10, no. 11, pp. 1325–1334, Nov. 2010.

[131] S. E. Headland and L. V. Norling, “The resolution of inflammation: Principles and challenges,” *Semin. Immunol.*, vol. 27, no. 3, pp. 149–160, 2015.

[132] T. Németh and A. Mócsai, “Feedback Amplification of Neutrophil Function.,” *Trends Immunol.*, vol. 37, no. 6, pp. 412–424, 2016.

[133] T. B. Issekutz, A. C. Issekutz, and H. Z. Movat, “The in vivo quantitation and kinetics of monocyte migration into acute inflammatory tissue.,” *Am. J. Pathol.*, vol. 103, no. 1, pp. 47–55, Apr. 1981.

[134] E. Kolaczkowska and P. Kubes, “Neutrophil recruitment and function in health and inflammation.,” *Nat. Rev. Immunol.*, vol. 13, no. 3, pp. 159–75, Mar. 2013.

[135] T. A. Wilgus, S. Roy, and J. C. McDaniel, “Neutrophils and Wound Repair: Positive Actions and Negative Reactions.,” *Adv. wound care*, vol. 2, no. 7, pp. 379–388, Sep. 2013.

[136] C. C. Winterbourn, A. J. Kettle, and M. B. Hampton, “Reactive Oxygen Species and Neutrophil Function.,” *Annu. Rev. Biochem.*, vol. 85, pp. 765–92, Jun. 2016.

[137] L. Kruidenier, I. Kuiper, C. B. H. W. Lamers, and H. W. Verspaget, “Intestinal oxidative damage in inflammatory bowel disease: semi-quantification, localization, and association with mucosal antioxidants.,” *J. Pathol.*, vol. 201, no. 1, pp. 28–36, Sep. 2003.

[138] A. M. Gardner *et al.*, “Apoptotic vs. nonapoptotic cytotoxicity induced by hydrogen peroxide.,” *Free Radic. Biol. Med.*, vol. 22, no. 1–2, pp. 73–83, 1997.

[139] W. C. Parks, C. L. Wilson, and Y. S. López-Boado, “Matrix metalloproteinases as modulators of inflammation and innate immunity.,” *Nat. Rev. Immunol.*, vol. 4, no. 8, pp. 617–29, Aug. 2004.

[140] O. Wéra, P. Lancellotti, and C. Oury, “The Dual Role of Neutrophils in Inflammatory Bowel Diseases.,” *J. Clin. Med.*, vol. 5, no. 12, Dec. 2016.

[141] V. Brinkmann *et al.*, “Neutrophil extracellular traps kill bacteria.,” *Science*, vol. 303, no. 5663, pp. 1532–5, Mar. 2004.

[142] T.-S. Teng, A.-L. Ji, X.-Y. Ji, and Y.-Z. Li, “Neutrophils and Immunity: From Bactericidal Action to Being Conquered.,” *J. Immunol. Res.*, vol. 2017, p. 9671604, 2017.

[143] V. Papayannopoulos and A. Zychlinsky, “NETs: a new strategy for using old weapons.,” *Trends Immunol.*, vol. 30, no. 11, pp. 513–21, Nov. 2009.

[144] M. J. Kaplan and M. Radic, “Neutrophil Extracellular Traps: Double-Edged Swords of Innate Immunity,” *J. Immunol.*, vol. 189, no. 6, pp. 2689–2695, Sep. 2012.

[145] A. Ortega-Gómez, M. Perretti, and O. Soehnlein, “Resolution of inflammation: an integrated view.,” *EMBO Mol. Med.*, vol. 5, no. 5, pp. 661–74, May 2013.

[146] A. Ayala, C.-S. Chung, P. S. Grutkoski, and G. Y. Song, “Mechanisms of immune resolution.,” *Crit. Care Med.*, vol. 31, no. 8 Suppl, pp. S558-71, Aug. 2003.

[147] A. J. Meszaros, J. S. Reichner, and J. E. Albina, “Macrophage-induced neutrophil apoptosis.,” *J. Immunol.*, vol. 165, no. 1, pp. 435–41, Jul. 2000.

[148] D. D. Chaplin, “Overview of the immune response.,” *J. Allergy Clin. Immunol.*, vol. 125, no. 2 Suppl 2, pp. S3-23, Feb. 2010.

[149] A. Spinelli, C. Correale, H. Szabo, and M. Montorsi, “Intestinal fibrosis in Crohn’s disease: medical treatment or surgery?,” *Curr. Drug Targets*, vol. 11, no. 2, pp. 242–8, Feb. 2010.

[150] D. C. Baumgart and W. J. Sandborn, “Crohn’s disease.,” *Lancet (London, England)*, vol. 380, no. 9853, pp. 1590–605, Nov. 2012.

[151] “Fistula,” *MedlinePlus*, 2018. [Online]. Available: https://medlineplus.gov/ency/article/002365.htm. [Accessed: 01-Oct-2018].

[152] K. Geboes, “Histopathology of Crohn’s disease and ulcerative colitis,” *Inflamm. bowel Dis. Edinburgh, London, Melb. Churchill Livingstone Elsevier*, vol. 18, pp. 255–276, 2003.

[153] D. C. Baumgart and W. J. Sandborn, “Inflammatory bowel disease: clinical aspects and established and evolving therapies.,” *Lancet (London, England)*, vol. 369, no. 9573, pp. 1641–57, May 2007.

[154] M. Rendi, P. E. Swanson, and M. P. Upton, “Crohn Disease Pathology,” *Medscape*, 2017. [Online]. Available: https://emedicine.medscape.com/article/1986158-overview#a1. [Accessed: 10-Jan-2018].

[155] R. B. Sartor, “Mechanisms of Disease: pathogenesis of Crohn’s disease and ulcerative colitis,” *Nat.Clin.Pract.Gastroenterol.Hepatol.*, vol. 3, no. 1743–4378; 7, pp. 390–407, 2006.

[156] A. Magarotto, S. Orlando, M. Coletta, D. Conte, M. Fraquelli, and F. Caprioli, “Evolving roles of cross-sectional imaging in Crohn’s disease,” *Dig. Liver Dis.*, vol. 48, no. 9, pp. 975–983, Sep. 2016.

[157] E. Rubin and J. L. Farber, *Essential Pathology*. Philadelphia: Lippincott Williams & Wilkins, 2000.

[158] “H&E 9860,” *Virtual Pathology at the University of Leeds*. [Online]. Available: http://www.virtualpathology.leeds.ac.uk/slides/library/. [Accessed: 18-Oct-2018].

[159] E. F. Stange *et al.*, “European evidence based consensus on the diagnosis and management of Crohn’s disease: definitions and diagnosis.,” *Gut*, vol. 55 Suppl 1, no. suppl_1, pp. i1-15, Mar. 2006.

[160] D. Jenkins *et al.*, “Guidelines for the initial biopsy diagnosis of suspected chronic idiopathic inflammatory bowel disease. The British Society of Gastroenterology Initiative.,” *J. Clin. Pathol.*, vol. 50, no. 2, pp. 93–105, Feb. 1997.

[161] Y.-H. Chen, D. Zhou, and D. I. Weltman, “Imaging in Crohn Disease,” *Medscape*, 2015. [Online]. Available: https://emedicine.medscape.com/article/367666-overview#a1. [Accessed: 05-Oct-2018].

[162] S. Taylor *et al.*, “METRIC (MREnterography or ulTRasound in Crohn’s disease): a study protocol for a multicentre, non-randomised, single-arm, prospective comparison study of magnetic resonance enterography and small bowel ultrasound compared to a reference standard in those ,” *BMC Gastroenterol.*, vol. 14, no. 1, p. 142, 2014.

[163] K. Horsthuis, P. C. F. Stokkers, and J. Stoker, “Detection of inflammatory bowel disease: diagnostic performance of cross-sectional imaging modalities,” *Abdom. Imaging*, vol. 33, no. 4, pp. 407–416, 2008.

[164] A. Furukawa *et al.*, “Cross-sectional imaging in Crohn disease.,” *Radiographics*, vol. 24, no. 3, pp. 689–702, 2004.

[165] J. Panes *et al.*, “Imaging techniques for assessment of inflammatory bowel disease: Joint ECCO and ESGAR evidence-based consensus guidelines,” *J. Crohn’s Colitis*, vol. 7, no. 7, pp. 556–585, 2013.

[166] G. Masselli, “Small Bowel Imaging: Clinical Applications of the Different Imaging Modalities—A Comprehensive Review,” *ISRN Pathol.*, vol. 2013, pp. 1–13, 2013.

[167] J. Panés *et al.*, “Systematic review: The use of ultrasonography, computed tomography and magnetic resonance imaging for the diagnosis, assessment of activity and abdominal complications of Crohn’s disease,” *Aliment. Pharmacol. Ther.*, vol. 34, no. 2, pp. 125–145, 2011.

[168] D. Choi *et al.*, “Bowel wall thickening in patients with Crohn’s disease: CT patterns and correlation with inflammatory activity.,” *Clin. Radiol.*, vol. 58, no. 1, pp. 68–74, Jan. 2003.

[169] M. Macari and E. J. Balthazar, “CT of Bowel Wall Thickening,” *Am. J. Roentgenol.*, vol. 176, no. 5, pp. 1105–1116, May 2001.

[170] Y. Weerakkody and F. Gaillard, “Fat halo sign (inflammatory bowel disease),” *Radiopaedia*. [Online]. Available: https://radiopaedia.org/articles/fat-halo-sign-inflammatory-bowel-disease?lang=us. [Accessed: 10-Sep-2020].

[171] M. G. Harisinghani, J. Wittenberg, W. Lee, S. Chen, A. L. Gutierrez, and P. R. Mueller, “Bowel Wall Fat Halo Sign in Patients Without Intestinal Disease,” *Am. J. Roentgenol.*, vol. 181, no. 3, pp. 781–784, Sep. 2003.

[172] H. Dave-Verma, S. Moore, A. Singh, N. Martins, and J. Zawacki, “Computed tomographic enterography and enteroclysis: pearls and pitfalls.,” *Curr. Probl. Diagn. Radiol.*, vol. 37, no. 6, pp. 279–87.

[173] N. Zakeri and R. C. G. Pollok, “Diagnostic imaging and radiation exposure in inflammatory bowel disease.,” *World J. Gastroenterol.*, vol. 22, no. 7, pp. 2165–78, Feb. 2016.

[174] G. Van Assche *et al.*, “The second European evidence-based Consensus on the diagnosis and management of Crohn’s disease: Definitions and diagnosis.,” *J. Crohns. Colitis*, vol. 4, no. 1, pp. 7–27, Feb. 2010.

[175] F. Maccioni *et al.*, “MR Imaging in Patients with Crohn Disease: Value of T2- versus T1-weighted Gadolinium-enhanced MR Sequences with Use of an Oral Superparamagnetic Contrast Agent,” *Radiology*, vol. 238, no. 2, pp. 517–530, Feb. 2006.

[176] J. Florie, M. N. J. M. Wasser, K. Arts-Cieslik, E. M. Akkerman, P. D. Siersema, and J. Stoker, “Dynamic Contrast-Enhanced MRI of the Bowel Wall for Assessment of Disease Activity in Crohn’s Disease,” *Am. J. Roentgenol.*, vol. 186, no. 5, pp. 1384–1392, May 2006.

[177] M. Fraquelli *et al.*, “Role of US in detection of Crohn disease: meta-analysis.,” *Radiology*, vol. 236, no. 1, pp. 95–101, Jul. 2005.

[178] F. Parente *et al.*, “Role of early ultrasound in detecting inflammatory intestinal disorders and identifying their anatomical location within the bowel.,” *Aliment. Pharmacol. Ther.*, vol. 18, no. 10, pp. 1009–16, Nov. 2003.

[179] D. J. Bell and B. DiMuzio, “Limberg score,” *Radiopaedia*. .

[180] T. Kucharzik, K. Kannengiesser, and F. Petersen, “The use of ultrasound in inflammatory bowel disease,” pp. 135–144, 2017.

[181] D. Strobel, R. S. Goertz, and T. Bernatik, “Diagnostics in inflammatory bowel disease: ultrasound.,” *World J. Gastroenterol.*, vol. 17, no. 27, pp. 3192–7, Jul. 2011.

[182] R. W. Stidham and R. K. Cross, “Endoscopy and cross-sectional imaging for assessing Crohn′s disease activity.,” *Tech. Gastrointest. Endosc.*, vol. 18, no. 3, pp. 123–130, Jul. 2016.

[183] S. Bharadwaj, N. Narula, P. Tandon, and M. Yaghoobi, “Role of endoscopy in inflammatory bowel disease,” *Gastroenterol. Rep.*, vol. 6, no. 2, pp. 75–82, May 2018.

[184] G. R. Lichtenstein, S. B. Hanauer, and W. J. Sandborn, “Management of Crohn’s disease in adults.,” *Am. J. Gastroenterol.*, vol. 104, no. 2, pp. 465–483; quiz 464, 484, 2009.

[185] D. W. Hommes and S. J. H. van Deventer, “Endoscopy in inflammatory bowel diseases.,” *Gastroenterology*, vol. 126, no. 6, pp. 1561–73, May 2004.

[186] M. J. Hamilton, “The valuable role of endoscopy in inflammatory bowel disease.,” *Diagn. Ther. Endosc.*, vol. 2012, p. 467979, 2012.

[187] W. A. Voderholzer *et al.*, “Small bowel involvement in Crohn’s disease: a prospective comparison of wireless capsule endoscopy and computed tomography enteroclysis.,” *Gut*, vol. 54, no. 3, pp. 369–73, Mar. 2005.

[188] M. Pennazio *et al.*, “Small-bowel capsule endoscopy and device-assisted enteroscopy for diagnosis and treatment of small- bowel disorders: European Society of Gastrointestinal Endoscopy (ESGE) Clinical Guideline,” *Endoscopy*, vol. 47, no. 4, pp. 352–376, 2015.

[189] C. W. Teshima and G. May, “Small bowel enteroscopy.,” *Can. J. Gastroenterol.*, vol. 26, no. 5, pp. 269–75, May 2012.

[190] B. Chassaing, J. D. Aitken, M. Malleshappa, and M. Vijay-Kumar, “Dextran Sulfate Sodium (DSS)-Induced Colitis in Mice,” in *Current Protocols in Immunology*, vol. 18, Hoboken, NJ, USA: John Wiley & Sons, Inc., 2014, pp. 15.25.1-15.25.14.

[191] T. Anbarasan *et al.*, “High Resolution Microultrasound (μUS) Investigation of the Gastrointestinal (GI) Tract,” 2017, pp. 541–561.

[192] H. S. Lay *et al.*, “In-Vivo Evaluation of Microultrasound and Thermometric Capsule Endoscopes,” *IEEE Trans. Biomed. Eng.*, vol. 66, no. 3, pp. 632–639, 2019.

[193] M. Perše and A. Cerar, “Dextran sodium sulphate colitis mouse model: traps and tricks.,” *J. Biomed. Biotechnol.*, vol. 2012, p. 718617, 2012.

[194] W. Elsheikh, K. L. Flannigan, W. McKnight, J. G. P. Ferraz, and J. L. Wallace, “Dextran sulfate sodium induces pan-gastroenteritis in rodents: Implications for studies of colitis,” *J. Physiol. Pharmacol.*, vol. 63, no. 5, pp. 463–469, 2012.

[195] T. Ohkusa, “[Production of experimental ulcerative colitis in hamsters by dextran sulfate sodium and changes in intestinal microflora].,” *Nihon Shokakibyo Gakkai Zasshi*, vol. 82, no. 5, pp. 1327–36, May 1985.

[196] D. D. Eichele and K. K. Kharbanda, “Dextran sodium sulfate colitis murine model: An indispensable tool for advancing our understanding of inflammatory bowel diseases pathogenesis,” *World J. Gastroenterol.*, vol. 23, no. 33, pp. 6016–6029, 2017.

[197] S. Wirtz *et al.*, “Chemically induced mouse models of acute and chronic intestinal inflammation,” *Nat. Protoc.*, vol. 12, no. 7, pp. 1295–1309, 2017.

[198] H. Laroui *et al.*, “Dextran sodium sulfate (dss) induces colitis in mice by forming nano-lipocomplexes with medium-chain-length fatty acids in the colon,” *PLoS One*, vol. 7, no. 3, 2012.

[199] M. Perše and A. Cerar, “Dextran Sodium Sulphate Colitis Mouse Model: Traps and Tricks,” *J. Biomed. Biotechnol.*, vol. 2012, pp. 1–13, 2012.

[200] Y. Yan *et al.*, “Temporal and spatial analysis of clinical and molecular parameters in dextran sodium sulfate induced colitis.,” *PLoS One*, vol. 4, no. 6, p. e6073, Jun. 2009.

[201] U. Erben *et al.*, “A guide to histomorphological evaluation of intestinal inflammation in mouse models.,” *Int. J. Clin. Exp. Pathol.*, vol. 7, no. 8, pp. 4557–76, 2014.

[202] A. Hedges, “Random Number Generator / Picker.” [Online]. Available: https://andrew.hedges.name/experiments/random/. [Accessed: 29-Nov-2018].

[203] P. Bankhead *et al.*, “QuPath: Open source software for digital pathology image analysis,” *Sci. Rep.*, vol. 7, no. 1, pp. 1–7, 2017.

[204] M. Haahr and S. Haahr, “List Randomizer,” *RANDOM.ORG*. [Online]. Available: https://www.random.org/lists/. [Accessed: 29-Nov-2018].

[205] A. G. Bradbury and R. E. Clutton, “Review of Practices Reported for Preoperative Food and Water Restriction of Laboratory Pigs (Sus scrofa).,” *J. Am. Assoc. Lab. Anim. Sci.*, vol. 55, no. 1, pp. 35–40, Jan. 2016.

[206] H. S. Lay, “In-Vivo Evaluation of Microultrasound and Thermometric Capsule Endoscopes.”

[207] G. Cummins, “Safety Evaluation of Additively Manufactured Ingestible Capsule Endoscope Packaging Prototypes for Translational Trials.”

[208] H. S. Lay *et al.*, “Microultrasound characterisation of ex vivo porcine tissue for ultrasound capsule endoscopy,” *J. Phys. Conf. Ser.*, vol. 797, p. 012003, Jan. 2017.

[209] R. Mosses, “ULTRACAP – Final Report: Microultrasound Surveillance of Barrett’s Oesophagus,” Glasgow, 2018.

[210] K. M. Sanders, S. D. Koh, S. Ro, and S. M. Ward, “Regulation of gastrointestinal motility—insights from smooth muscle biology,” *Nat. Rev. Gastroenterol. Hepatol.*, vol. 9, no. 11, pp. 633–645, Nov. 2012.

[211] M. S. Piper and R. J. Saad, “Diabetes Mellitus and the Colon.,” *Curr. Treat. Options Gastroenterol.*, vol. 15, no. 4, pp. 460–474, Dec. 2017.

[212] M. Zhao, D. Liao, and J. Zhao, “Diabetes-induced mechanophysiological changes in the small intestine and colon.,” *World J. Diabetes*, vol. 8, no. 6, pp. 249–269, Jun. 2017.

[213] X. Wang *et al.*, “Development of a Mechanical Scanning Device With High-Frequency Ultrasound Transducer for Ultrasonic Capsule Endoscopy,” *IEEE Trans. Med. Imaging*, vol. 36, no. 9, pp. 1922–1929, Sep. 2017.

[214] Y. Qiu *et al.*, “Ultrasound capsule endoscopy with a mechanically scanning micro-ultrasound: a porcine study,” *Manuscr. Prog.*

[215] Luke Newman, “Klebsiella contamination in WBRU-TG,” 2018.

[216] Charles River Research Models and Services, “Klebsiella species,” *Tech. Sheet*, 2009.

[217] T. Tanaka *et al.*, “Dextran sodium sulfate strongly promotes colorectal carcinogenesis in ApcMin/+ mice: Inflammatory stimuli by dextran sodium sulfate results in development of multiple colonic neoplasms,” *Int. J. Cancer*, vol. 118, no. 1, pp. 25–34, 2006.

[218] A. Fatehullah *et al.*, “Increased variability in ApcMin/+ intestinal tissue can be measured with microultrasound,” *Sci. Rep.*, vol. 6, no. October 2015, p. 29570, Jul. 2016.

[219] M. Brückner *et al.*, “Detection and characterization of murine colitis and carcinogenesis by molecularly targeted contrast-enhanced ultrasound,” *World J. Gastroenterol.*, vol. 23, no. 16, p. 2899, 2017.

[220] S. C. Ng *et al.*, “Worldwide incidence and prevalence of inflammatory bowel disease in the 21st century: a systematic review of population-based studies,” *Lancet*, vol. 390, no. 10114, pp. 2769–2778, 2017.

[221] NICE, “Inflammatory bowel disease,” 2014.

[222] K. Bodger, “Cost of Illness of Crohn’s Disease,” *Pharmacoeconomics*, vol. 20, no. 10, pp. 639–652, 2002.

[223] Ø. Hovde *et al.*, “Mortality and causes of death in Crohn’s disease: results from 20 years of follow-up in the IBSEN study,” *Gut*, vol. 63, no. 5, pp. 771–775, May 2014.

[224] P. B. Carvalho, B. Rosa, F. D. de Castro, M. J. Moreira, and J. Cotter, “PillCam COLON 2 © in Crohn’s disease: A new concept of pan-enteric mucosal healing assessment,” *World J. Gastroenterol.*, vol. 21, no. 23, pp. 7233–7241, Jun. 2015.

[225] R. V. Bryant, S. Winer, T. SPL, and R. H. Riddell, “Systematic review: Histological remission in inflammatory bowel disease. Is ‘complete’ remission the new treatment paradigm? An IOIBD initiative,” *J. Crohn’s Colitis*, vol. 8, no. 12, pp. 1582–1597, Dec. 2014.

[226] J. U. Kang, “Virtual Biopsy [Point of View],” *Proc. IEEE*, vol. 98, no. 4, pp. 503–505, Apr. 2010.

[227] S. Ødegaard, L. B. Nesje, O. D. Lærum, and M. B. Kimmey, “High-frequency ultrasonographic imaging of the gastrointestinal wall,” *Expert Rev. Med. Devices*, vol. 9, no. 3, pp. 263–273, May 2012.

[228] K. Nylund *et al.*, “Crohn’s disease: Comparison of in vitro ultrasonographic images and histology,” *Scand. J. Gastroenterol.*, vol. 43, no. 6, pp. 719–726, Jan. 2008.

[229] G. Bassotti, F. Chistolini, and A. Morelli, “Pathophysiological aspects of diverticular disease of colon and role of large bowel motility.,” *World J. Gastroenterol.*, vol. 9, no. 10, pp. 2140–2, Oct. 2003.

[230] L. Wess, M. A. Eastwood, T. J. Wess, A. Busuttil, and A. Miller, “Cross linking of collagen is increased in colonic diverticulosis.,” *Gut*, vol. 37, no. 1, pp. 91–4, Jul. 1995.

[231] G. Cummins *et al.*, “Gastrointestinal diagnosis using non-white light imaging capsule endoscopy,” *Nat. Rev. Gastroenterol. Hepatol.*, pp. 1–19.

[232] H. S. Lay, B. F. Cox, V. Seetohul, C. E. M. Demore, and S. Cochran, “Design and Simulation of a Ring-Shaped Linear Array for Microultrasound Capsule Endoscopy,” *IEEE Trans. Ultrason. Ferroelectr. Freq. Control*, pp. 1–1, 2018.

[233] A. Ziegler, L. Gonzalez, and A. Blikslager, “Large Animal Models: The Key to Translational Discovery in Digestive Disease Research,” *Cell. Mol. Gastroenterol. Hepatol.*, vol. 2, no. 6, pp. 716–724, Nov. 2016.

[234] M. M. Swindle, A. Makin, A. J. Herron, F. J. Clubb, and K. S. Frazier, “Swine as Models in Biomedical Research and Toxicology Testing,” *Vet. Pathol.*, vol. 49, no. 2, pp. 344–356, 2012.

[235] T. T. Kararli, “Comparison of the gastrointestinal anatomy, physiology, and biochemistry of humans and commonly used laboratory animals,” *Biopharm. Drug Dispos.*, vol. 16, no. 5, pp. 351–380, 1995.

[236] A. M. Merritt, C. D. Buergelt, and L. C. Sanchez, “Porcine ileitis model induced by TNBS-ethanol instillation.,” *Dig. Dis. Sci.*, vol. 47, no. 4, pp. 879–85, Apr. 2002.

[237] T. Flisikowska *et al.*, “A porcine model of familial adenomatous polyposis,” *Gastroenterology*, vol. 143, no. 5, pp. 1173-1175.e7, 2012.

[238] J. G. Fujimoto *et al.*, “New technology for high-speed and high-resolution optical coherence tomography.,” *Ann. N. Y. Acad. Sci.*, vol. 838, pp. 95–107, Feb. 1998.

[239] M. J. Gora *et al.*, “Tethered capsule endomicroscopy enables less invasive imaging of gastrointestinal tract microstructure.,” *Nat. Med.*, vol. 19, no. 2, pp. 238–40, Feb. 2013.

[240] M. J. Gora *et al.*, “Imaging the upper gastrointestinal tract in unsedated patients using tethered capsule endomicroscopy.,” *Gastroenterology*, vol. 145, no. 4, pp. 723–5, Oct. 2013.

[241] J. G. Fujimoto, C. Pitris, S. A. Boppart, and M. E. Brezinski, “Optical coherence tomography: an emerging technology for biomedical imaging and optical biopsy.,” *Neoplasia*, vol. 2, no. 1–2, pp. 9–25, Jun. 2016.

[242] G. Cummins *et al.*, “Gastrointestinal diagnosis using non-white light imaging capsule endoscopy,” *Nat. Rev. Gastroenterol. Hepatol.*, Apr. 2019.

[243] A. F. Fercher, “Optical coherence tomography – development, principles, applications,” *Z. Med. Phys.*, vol. 20, no. 4, pp. 251–276, Nov. 2010.

[244] T.-H. Tsai, J. Fujimoto, and H. Mashimo, “Endoscopic Optical Coherence Tomography for Clinical Gastroenterology,” *Diagnostics*, vol. 4, no. 2, pp. 57–93, May 2014.

[245] B. F. Cox, V. Seetohul, H. Lay, and S. Cochran, “Microultraound and small bowel inflammation: Tissue phantom studies,” in *2015 IEEE International Ultrasonics Symposium (IUS)*, 2015, pp. 1–4.

[246] M. Laviron, C. Combadière, and A. Boissonnas, “Tracking monocytes and macrophages in tumors with live imaging,” *Front. Immunol.*, vol. 10, no. MAY, pp. 1–9, 2019.

[247] M. Monici *et al.*, “Natural fluorescence of white blood cells: spectroscopic and imaging study,” *J. Photochem. Photobiol. B Biol.*, vol. 30, no. 1, pp. 29–37, Sep. 1995.

[248] Z. Fireman, “Capsule endoscopy: Future horizons.,” *World J. Gastrointest. Endosc.*, vol. 2, no. 9, pp. 305–7, Sep. 2010.

[249] S. Yang, “Data analysis for diagnosis of pathology in microultrasound images of the gut,” University of Glasgow, 2018.

[250] S. Yang, B. F. Cox, C. Lemke, I. S. Näthke, and S. Cochran, “Deep Learning Enabled Micro-Ultrasound for Characterization of Mouse Bowel Inflammation,” no. Manuscript in Progress, 2020.

[251] J. C. Norton *et al.*, “Intelligent magnetic manipulation for gastrointestinal ultrasound,” *Sci. Robot.*, vol. 4, no. 31, p. eaav7725, Jun. 2019.

Appendix A

	µUS Step scanner	µUS Continuous Sweep Scanner
Scanning Method	Step-acquire-repeat scans	Mid mode: 0.1 mm/s
Average speed of scan	Average speed: 0.012 mm/s	Fast mode: 2.0 mm/s
Minimum programmable increment of stage motors	2.0 µm	0.5 µm
RF data acquisition	Sampling frequency for the step scanner is adjustable according to oscilloscope time base, with a maximum frequency of 2.5 GHz.	Obtained from a 12-Bit FlexRIO oscilloscope adapter module at a sampling frequency of 800 MS/s.
A-scan storage	Each A-scan stored was the temporal average of <128 echoes to decrease noise, and transfer of 9-bit data from the oscilloscope to computer is via a general purpose interface bus (GPIB).	Each A-scan stored was the temporal average of between 4 and 32 echoes to decrease noise, and transfer of 12-bit data from the digitizer was to computer via PCI Express.
Maximum scan length	Available precision step scanning stage length is 100 mm.	Available continuous scanning stage length is >50 mm.

Table A1. Technical differences between µUS step and continuous sweep scanning systems. Table adapted from T. Anbarasan, C.E.M. Démoré, H. Lay, M.R.S. Sunqrot, R. Poltarjonoks, S. Cochran, B.F. Cox., "High Resolution Microultrasound (µUS) Investigation of the Gastrointestinal (GI) Tract," 2017, pp. 541–561

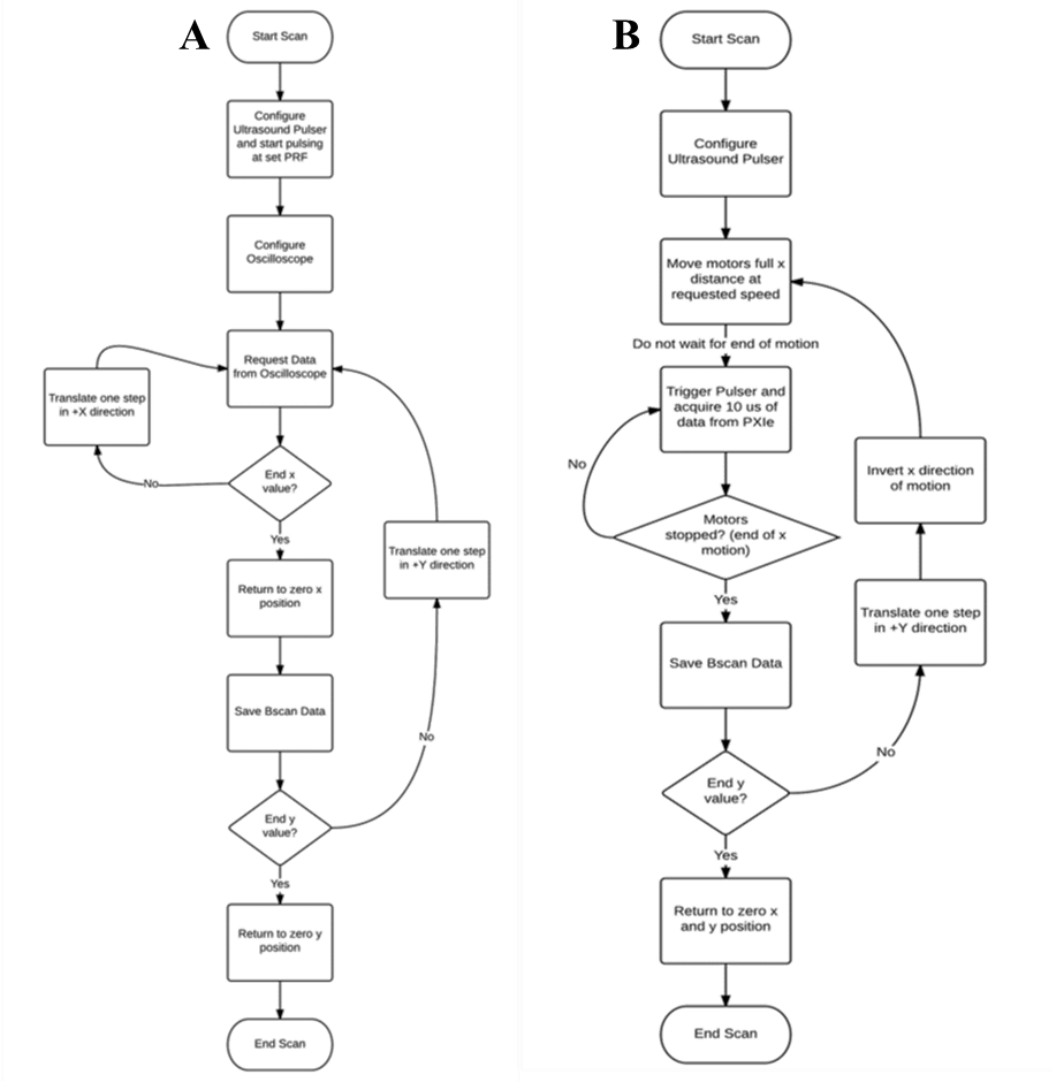

Figure. 1A. Scanning automation algorithm for (A**)** µUS step scanner (B**)** µUS continuous sweep scanner. Figure adapted from T. Anbarasan, C.E.M. Démoré, H. Lay, M.R.S. Sunqrot, R. Poltarjonoks, S. Cochran, B.F. Cox., "High Resolution Microultrasound (µUS) Investigation of the Gastrointestinal (GI) Tract," 2017, pp. 541–561.

Appendix B

1. Histoclear 1…5 min
2. Histoclear 2…5 min
3. 100% Ethanol 1…3 min
4. 100% Ethanol 2…3 min
5. 70% Ethanol…3 min
6. Wash in tap water…5 mins
7. Mayer's Haematoxylin…5 min
8. Wash in tap water…5 mins
9. Blue in Scott's[1] tap water…2 min
10. Wash in tap water…3 mins
11. Eosin…5 mins
12. Wash in tap water…3-5 sec (Very quick wash or all your eosin will disappear)
13. 95% Ethanol…10 sec
14. 100% Ethanol 3…2 min
15. 100% Ethanol 4…3 min
16. Histoclear 3…5 min
17. Histoclear 4…5 min
18. Mount in DPX

1. Scott's Tap water is just distilled water with a sprinkle of Sodium Bicarbonate dissolved in it. It doesn't have to an exact measurment, just as long as the solution is slightly alkaline

Table 1B. Haematoxylin and Eosin (H&E) staining from Calum Thomson